Modeling of Electronic Properties in Organic Semiconductor Device Structures

A DISSERTATION
SUBMITTED TO THE FACULTY OF THE GRADUATE SCHOOL
OF THE UNIVERSITY OF MINNESOTA
BY

Hsiu-Chuang Chang

IN PARTIAL FULFILLMENT OF THE REQUIREMENTS
FOR THE DEGREE OF
DOCTOR OF PHILOSOPHY

Dr. P. Paul Ruden, Advisor

May 2012

© Hsiu-Chuang Chang 2012

Acknowledgements

My time here at the University of Minnesota (UMN) in the Electrical and Computer Engineering Department has been an extraordinarily educating experience. Numerous individuals have helped over the course of my graduate studies. First and foremost, I would like to express my deepest gratitude to my advisor, Dr. P. Paul Ruden, for all his research guidance, endless patience, and continuous encouragement in every aspect of my life. I feel very privileged to be one of his graduate students.

I would like to thank my collaborators, Dr. Yan Liang and Prof. C. Daniel Frisbie, for all the experimental work presented in this thesis. It has been a wonderful time to work with Yan who has proposed creative and interesting ideas and inspired me to figure out problems from different perspectives. I would like to thank the former and current Ruden group members: Dr. Dominic Schroepfer, Dr. Mohammad Yunus, Dr. Isaiah P. Steinke, Feilong Liu, and Aditi Goswami for providing support and making the office an enjoyable place of work. Nick Erickson from the Holmes group also deserves acknowledgement for helpful discussions. I would also like to express my appreciation for the computational resources provided by the Minnesota Supercomputing Institute, and the financial support from the National Science Foundation through the UMN Materials Research Science and Engineering Center (MRSEC).

Finally, I would like to sincerely thank my family, in particular my parents, for their constant support and love.

Dedication

To my parents

Fang-Yuan Chang and Mei-Yueh Hsieh

Abstract

Organic semiconductors (OSCs) have recently become viable for a wide range of electronic devices, some of which have already been commercialized. With the mechanical flexibility of organic materials and promising performance of organic field effect transistors (OFETs) and organic bulk heterojunction devices, OSCs have been demonstrated in applications such as radio frequency identification tags, flexible displays, and photovoltaic cells.

Transient phenomena play decisive roles in the performance of electronic devices and OFETs in particular. The dynamics of the establishment and depletion of the conducting channel in OFETs are investigated theoretically. The device structures explored resemble typical organic thin-film transistors with one of the channel contacts removed. By calculating the displacement current associated with charging and discharging of the channel in these capacitors, transient effects on the carrier transport in OSCs may be studied. In terms of the relevant models it is shown that the non-linearity of the process plays a key role. The non-linearity arises in the simplest case from the fact that channel resistance varies during the charging and discharging phases. Traps can be introduced into the models and their effects examined in some detail. When carriers are injected into the device, a conducting channel is established with traps that are initially empty. Gradual filling of the traps then modifies the transport characteristics of the injected charge carriers. In contrast, dc measurements as they are typically performed to characterize the transport properties of organic semiconductor channels investigate a steady state with traps partially filled. Numerical and approximate analytical models of the formation of the conducting channel and the resulting displacement currents are presented.

For the process of transient carrier extraction, it is shown that if the channel capacitance is partially or completely discharged through the channel resistance, qualitatively different time dependences of the displacement current may be obtained.

Depending on the final state of the capacitor, either fully discharged or remaining partially charged, the displacement current in the long time limit shows power law or exponential dependence on time. The salient effect of including fast traps in this model is to change the apparent exponent in the resulting approximate power law for the case of full depletion. The exponent of the power law decreases in magnitude as the ratio of the emission to capture rates decreases. In contrast, the effects of slow traps are quite different. If significant, slow traps can give rise to a slowly decaying displacement current.

In organic bulk heterojunction photovoltaic cells, large interfacial areas that impact the efficiency of photo-generation of charge carriers are of critical importance. Carrier recombination at the interface is studied on the basis of two bilayer structures with interfaces perpendicular and parallel to the current direction, which idealize the island-like morphology of mixed materials. Overall recombination currents at the interface are found to depend strongly on the interface orientation and on parameters that control the time scales of interfacial recombination and carrier transport.

Table of Contents

Acknowledgements .... **i**

Dedication .... **ii**

Abstract .... **iii**

Table of Contents .... **v**

List of Tables .... **viii**

List of Figures .... **ix**

1 Introduction **1**

1.1 Literature review 1

1.1.1 Organic field effect transistors (OFETs) 2

1.1.2 Organic photovoltaic cells (OPVs) 5

1.2 Objective of the work 8

1.3 Organization of the thesis 9

2 Transient charge carrier transport effects in OFET channels **12**

2.1 Introduction and motivation 12

2.2 Device structure and experimental method 14

2.2.1 Carrier injection and extraction 18

2.3 Conducting channel formation and depletion 20

2.3.1 Geometric model 20

2.3.2 Spatially averaged carrier density model 24

2.3.3 Resistor-capacitor model 28

2.3.4 Numerical device model 31

2.4 Effects of traps 35

2.4.1 Slow traps 37

2.4.2 Fast traps 41
2.4.3 Intermediate traps 43
2.4.4 Non-uniform distribution of trap states: metal/semiconductor interface 45
2.5 Conclusion 48

3 Charge carrier extraction transient in OFET channels 49

3.1 Introduction 49
3.2 Device structure and experiments 49
3.3 Time dependent discharge current 51
3.3.1 Resistor-capacitor circuit model 51
3.3.2 Discharge current without traps 53
3.3.3 Effects of traps 55
3.4 Conclusion 57

4 Geometric effects on interfacial recombination 59

4.1 Motivation 59
4.2 Bilayer structure with interface perpendicular to the current direction 61
4.3 Bilayer structure with interface parallel to the current direction 65
4.3.1 Profiles of normalized carrier densities and interfacial recombination 67
4.3.2 Time scales of interfacial recombination and carrier transport 72
4.3.3 Geometric effects of multiple interfaces on interfacial recombination 79
4.3.4 Carrier balance 85
4.4 Conclusion 88

5 Summary and suggestions for future work 90

5.1 Transient charge carrier transport 90
5.1.1 Summary 90
5.1.2 Suggestions for future work 91
5.2 Geometric effects on interfacial recombination 94
5.2.1 Summary 94
5.2.2 Suggestions for future work 94

References...96

Appendix...104

A. Hopping transport in disordered semiconductors 104

B. Numerical method for the displacement current device model 109

C. Analytical solutions for the non-linear resistor-capacitor circuit model 111

C.1 Linear voltage profile..112

C.2 Step function voltage profile...114

D. Numerical method for the bilayer structure with interface parallel to the current direction 117

List of Tables

Table 2.1 Average injected, extracted, trapped carrier densities, and percentage of trapped carriers over total injected carriers. 19

Table 2.2 Time scales of different carrier transport effects 23

Table 4.1 Time scales for interfacial recombination rate and carrier transport 73

List of Figures

Figure 1.1	Organic light-emitting diodes flexible display developed by Industrial Technology Research Institute	1
Figure 1.2	Chemical structures for pentacene and P3HT	3
Figure 1.3	Organic-transistor geometries	4
Figure 1.4	Flowchart of major physical processes in organic photovoltaics	8
Figure 2.1	Schematic diagrams for the device structure and gate voltage profile	15
Figure 2.2	Measured displacement current versus time	16
Figure 2.3	Measured displacement current versus voltage	16
Figure 2.4	Displacement current measured in consecutive sweeps	19
Figure 2.5	Calculated carrier density profile in the geometric model	22
Figure 2.6	Calculated *I-V* characteristics in the geometric model	23
Figure 2.7	Calculated carrier densities in the spatially averaged charge carrier model	27
Figure 2.8	Calculated *I-V* characteristics in the spatially averaged carrier density model	27
Figure 2.9	The resistor-capacitor equivalent circuit model	29
Figure 2.10	Calculated *I-V* characteristics in the resistor-capacitor model	31
Figure 2.11	Calculated *I-V* characteristics in the full numerical model for the trap free case	34
Figure 2.12	Calculated *I-V* characteristics for trap time constants much larger than the time scale of the transient process	38
Figure 2.13	Calculated *I-V* characteristics of different capture time constants with a fixed emission time constant	39
Figure 2.14	Calculated *I-V* characteristics of different emission time constants with a fixed capture time constant	40

Figure 2.15	Calculated *I-V* characteristics in consecutive sweeps	40
Figure 2.16	Calculated *I-V* characteristics for trap time constants much smaller than the time scale of the transient process	42
Figure 2.17	Calculated *I-t* characteristics for trap time constants much smaller than the time scale of the transient process	42
Figure 2.18	Calculated *I-V* characteristics for trap time constants comparable with the time scale of the transient process	44
Figure 2.19	Calculated *I-t* characteristics for trap time constants comparable with the time scale of the transient process	44
Figure 2.20	Measured *I-t* characteristics from devices fabricated with Au contact with different thickness of pentacene films	46
Figure 2.21	Average trapped carrier density with Au contact with different thickness of pentacene films and schematic diagrams for the penetration of Au atoms	46
Figure 2.22	Calculated *I-t* characteristics with deep traps limited to a narrow region near the contact edge (non-uniform trap distribution)	47
Figure 3.1	Schematic device structure, the resistor-capacitor equivalent circuit model, and gate voltage profile	50
Figure 3.2	Measured discharge current versus time	51
Figure 3.3	Measured discharge current compared with analytical results	54
Figure 3.4	Mobile carrier densities versus total carrier densities	56
Figure 3.5	Numerically calculated results compared with experimental data	57
Figure 4.1	Morphology of bulk heterojunction structure simplified by combinations of interfaces perpendicular or parallel to the current direction	61
Figure 4.2	Schematic diagram for the bilayer structure with interface perpendicular to the current direction	62
Figure 4.3	Normalized carrier density profile	64
Figure 4.4	Schematic diagrams for the bilayer structure with interface parallel to the current direction	65
Figure 4.5	Normalized carrier density profiles of a bilayer structure	68

Figure 4.6 Normalized carrier density profiles of multiple-layer structures 69

Figure 4.7 Normalized carrier density profile of a five-layer structure 70

Figure 4.8 J_s versus x/L with and without the electric field 71

Figure 4.9 J_s versus x/L shown for three interfaces labeled in Fig. 4.5(c), in the absence of the electric field 71

Figure 4.10 J_s versus x/L shown for three interfaces labeled in Fig. 4.5(c), in the presence of the electric field 72

Figure 4.11 Recombination ratio (I_{rec}/I_{in}) versus W/L 74

Figure 4.12 Recombination ratio (I_{rec}/I_{in}) versus W/L under the influence of the electric field 75

Figure 4.13 I_{rec} versus W_T/L 76

Figure 4.14 I_{rec}/W_T versus t_{rec}/t_L 78

Figure 4.15 I_{rec}/W_T versus $t_{rec}/t_{diff.L}$ with and without the influence of the electric field 78

Figure 4.16 Current ratios ($I_{8\text{-}lays}/I_{2\text{-}lays}$ and $I_{4\text{-}lays}/I_{2\text{-}lays}$) versus W_T/L, in the case of slow recombination rate 80

Figure 4.17 Current ($I_{8\text{-}lays}/I_{2\text{-}lays}$ and $I_{4\text{-}lays}/I_{2\text{-}lays}$) versus W_T/L, in the case of fast recombination rate in the absence of the electric field 82

Figure 4.18 Normalized carrier density profiles with respect to the y-direction 83

Figure 4.19 Current ratios ($I_{8\text{-}lays}/I_{2\text{-}lays}$ and $I_{4\text{-}lays}/I_{2\text{-}lays}$) versus W_T/L, in the case of fast recombination rate in the presence of the electric field 84

Figure 4.20 Normalized carrier density profiles calculated at the interface as a function of x/L without the electric field ($\mu_n > \mu_p$) 86

Figure 4.21 Normalized carrier density profiles calculated at the interface as a function of x/L with the electric field ($\mu_n > \mu_p$) 86

Figure 4.22 I_{rec}/W_T versus $t_{rec}/t_{L-\mu_0}$ for three different sets of electron and hole mobilities 87

Figure 4.23 Current ratios ($I_{8\text{-}lays}/I_{2\text{-}lays}$ and $I_{4\text{-}lays}/I_{2\text{-}lays}$) versus W_T/L in the absence of the electric field where $\mu_n > \mu_p$ 88

Figure 5.1 Modified gate voltage profile 92

Figure 5.2	Calculated results (with traps) for various modified gate voltage profiles	93
Figure 5.3	Experimental data for various modified gate voltage profiles	93
Figure A.1	Hopping process between two localized states	105
Figure A.2	Schematic diagrams for nearest-neighbor and variable-range hopping	106
Figure B.1	A computational molecule for the explicit form	110
Figure C.1	The resistor-capacitor equivalent circuit model	111
Figure D.1	Schematic diagram for the bilayer structure with interface parallel to the current direction	117
Figure D.2	Carrier densities with indices at the interface	119
Figure D.3	Flowchart of the algorithm for the numerical calculation	121

1 Introduction

1.1 Literature review

For the last half a century, inorganic semiconductors have dominated the microelectronics industry, allowing for the development for the memory devices, integrated circuits, and microprocessors in all commercialized electronics.[1] However, processing methods for fabricating inorganic devices are becoming ever more complex and expensive.

Beginning in the mid 1980s, organic electronics has burgeoned with the discovery and development of the organic photovoltaics (OPVs),[2-7] organic light emitting diode (OLEDs), [8-15] and organic field effect transistors (OFETs). [16-19] Since then, interest in these devices has steadily increased in both academia and industry. Organic semiconductors, primarily small molecules and conjugated polymers, have potential for low-cost and large-area applications, such as electronic papers, flexible displays, and radio frequency identification tags (RFIDs).[20] Although the relatively weak intermolecular bonding which contributes to the mechanical flexibility of the organic materials limits the charge carrier mobilities, a wide range of organic electronic devices have already been commercialized.[21-23] Figure 1.1 shows one of the organic electronic products, an OLED flexible display.

Figure 1.1: OLED flexible display developed by ITRI (Industrial Technology Research Institute).[24]

1.1.1 Organic field effect transistors (OFETs)

The field effect transistor (FET) is one of the most fundamental devices in the semiconductor industry. In a FET, the flow of charge carriers between source and drain terminals constitutes a current that is controlled by the transverse electric field induced by the gate voltage across the dielectric layer. Among the advantages that organic semiconductors possess over conventional inorganic semiconductors is a relatively low production cost and mechanical flexibility. This motivates the development of OFETs.[25-28] Although OFETs may not be able to replace inorganic FETs due to the limited speed of operation of the former, there is still significant potential for OFETs for a range of low-cost applications. For instance, the compatibility of organic materials with plastic substrates makes OFETs one of the major candidates for the next generation of technology in large-area flexible displays.[29]

In a conventional inorganic device, lightly doped silicon or combinations of group III-V elements comprise the active semiconductor layer. The active layer of organic devices is comprised of small hydrocarbon molecules[30,31] or conjugated polymers.[32,33] The ability of organic molecules to transport charge carriers is primarily due to overlapping π-bonds of neighboring molecules. Conjugation creates a sp^2 hybridized network of delocalized orbitals that extend over much of the molecule. Planar conjugated molecules such as pentacene[34-39] composed of five fused benzene rings serve as candidates for high performance OFETs. However, the deposition of small molecule thin films through vacuum sublimation increases cost, hindering from scaling up to commercialized applications. Solution-processable conjugated polymers, on the other hand, offer the possibility to manufacture OFETs by low-cost printing techniques with which polymeric integrated circuits with the operating frequency above 50 kHz have already been fabricated.[40-51] Additionally, conjugated polymers may be chemically tailored to achieve desirable electronic and optical properties. Poly(3-hexylthiophene) (P3HT), for example, is notable for its high mobility. The regioregular structure of P3HT allows neighboring chains to overlap in ordered stacks, exhibiting high degrees of crystallinity.[52-56] Figure 1.2 shows chemical structures for pentacene and P3HT.

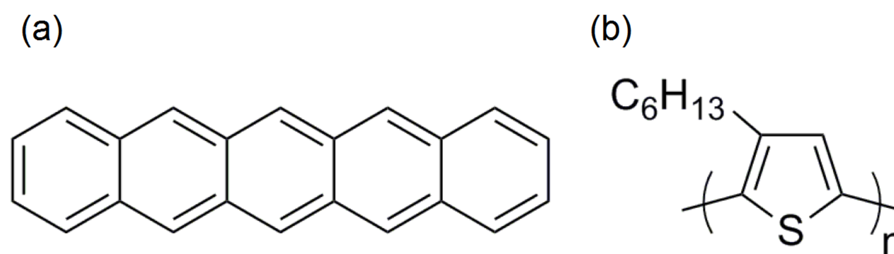

Figure 1.2: Chemical structures of: (a) pentacene and (b) P3HT.

Charge carrier mobility is of critical importance in the performance of OFETs. One of the earliest OFETs was reported by Tsumura *et al.* in 1986 with a carrier mobility ~10^{-5} $cm^2V^{-1}s^{-1}$.[16] After more than two decades of research and device optimization, mobility values in high performance OFETs are well above 1 $cm^2V^{-1}s^{-1}$.[28,57] As for organic thin film transistors (OTFTs) based on solution-processed polymers[58] or small molecules,[59,60] mobility values as high as 1 $cm^2V^{-1}s^{-1}$ have also been achieved, which is comparable to the mobility of amorphous silicon-based transistors.[61] Therefore, OFETs and OTFTs are appropriate for applications such as sensors and RFIDs.[62] Even though numerous experiments have been performed to study the electronic properties and carrier transport,[63-66] the exact nature of charge transport in organic semiconductors is still the subject of intensive research. The concept of valence and conduction bands is seldom used in the organic semiconductor literature and almost all the organic semiconductors are disordered materials. In lieu of the valence and conduction bands, the designated states for hole and electron transport are referred to as the highest occupied molecular orbital (HOMO) and lowest unoccupied molecular orbital (LUMO), respectively.[67,68] At present theories of charge transport in organic semiconductors include hopping, polaron, and band-like models.[28,69] In Appendix A, we briefly discuss hopping transport in disordered semiconductors.

Two geometries for OFETs are depicted in Fig. 1.3. The main components are: (i) an organic semiconductor layer composed of small molecules or polymers, (ii) a gate dielectric layer, and (iii) three conducting electrodes referred to as source, drain, and gate. The device can be viewed as a parallel plate capacitor with one plate constituted by the

gate electrode, while the organic active layer is the second plate with the two remaining electrodes, source and drain, directly in contact with the semiconductor. Two different classes of geometries in Fig. 1.3 are based on the order in which the various components are deposited.

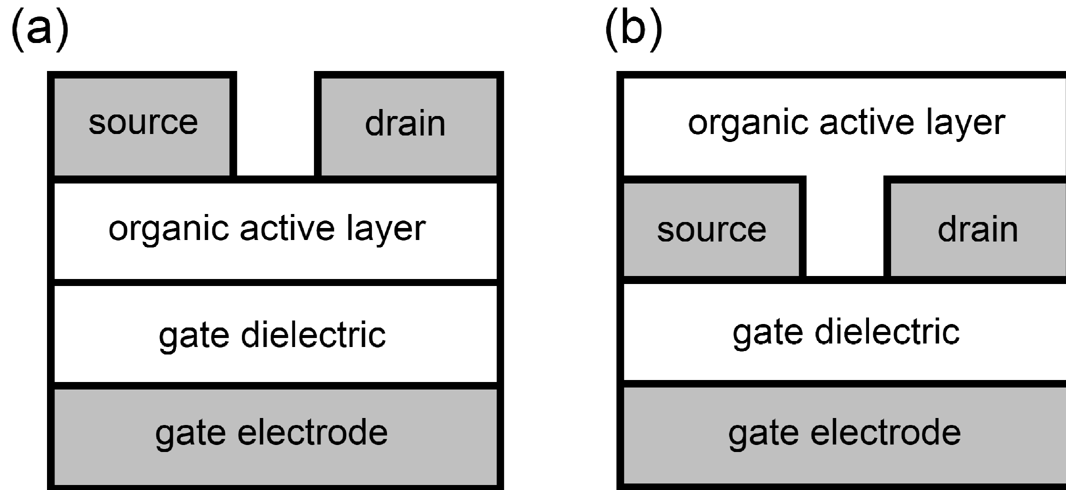

Figure 1.3: Two organic-transistor geometries, bottom gate with: (a) top contacts. (b) bottom contacts.

Usually, organic semiconductors are not doped. Mobile charge carriers are injected and extracted into and from the semiconductor through source and drain electrodes. A conduction channel is established when the gate voltage, V_G, exceeds a given threshold voltage, V_T. The threshold voltage may result from the presence of (charged) trapped carriers at the dielectric surface, leading to a necessarily additional gate voltage to induce the channel formation, or the presence of trap states in the semiconductor that need to be filled before mobile carriers can be induced in the channel. Considering the case of a p-type organic semiconductor field effect transistor in dc measurement, the transistor functions in the linear regime when $|V_{GS} - V_T| >> |V_{DS}|$, and the current, I_D, is expressed as

$$I_D = \frac{W}{L}\mu C'\left[(V_{GS} - V_T) - \frac{V_{DS}}{2}\right]V_{DS}, \qquad (1.1)$$

where W is the channel width, L is the channel length, μ is the charge carrier mobility, C' is the capacitance per unit area of the gate dielectric, V_{GS} is the potential difference between gate and source, and V_{DS} is the potential difference between drain and source. When $|V_{GS} - V_T| < |V_{DS}|$, the transistor functions in the saturation regime, and the current is given by

$$I_D = \frac{W}{2L}\mu C'(V_{GS} - V_T)^2. \qquad (1.2)$$

1.1.2 Organic photovoltaic cells (OPVs)

Over the past two decades, the science and engineering of organic semiconducting materials have advanced rapidly, leading to the demonstration and optimization of a range of organics-based devices, including organic photovoltaics.[21,22] In 1986, Kodak Corporation introduced the first bilayer OPV[2] with the power conversion efficiency about 1%, which provides the promise of mechanically flexible solar cells using low-cost and large-area manufacturing techniques in the future.[70-72] Since then, many modifications and improvements to OPVs have been proposed, including new photovoltaic materials, deposition techniques, device architectures, and electrode materials.[73-75] Recently, the certified power conversion efficiency of 9.8 % for a 1.1 cm^2 tandem cell manufactured with a low temperature evaporation process has been achieved,[76] and 10.1 % for solution-processed small molecules has been reached.[77] Efficiency exceeding the 10 % benchmark of the amorphous silicon devices is a significant milestone for organic solar cells.

While the physics of conventional p-n junctions and properties of inorganic solar cells are well understood, the understanding of the underlying science in organic solar

cells remains an intense subject of research. One of the significant advantages for OPVs over conventional inorganic solar cells is the relative ease with which the optoelectronic properties can be tuned through well-developed methods of synthesis. Additionally, organic semiconductors have such a higher absorption coefficient that much more light can be absorbed in thinner and lighter organic solar cells. However, the photo-excitation of the organic semiconductors does not automatically lead to the generation of mobile charge carriers, due to strongly bound electron-hole pairs called excitons with a binding energy of hundreds of meV.[78,79] Excitons need to be split up before the mobile carriers can be transported through the film and collected at the electrodes. Moreover, the relatively small diffusion range of excitons compared with the film thickness necessary to absorb the major portion of the incident light has made it difficult to reach high conversion efficiency.

Figure 1.4 shows the dominant physical processes converting light to photocurrent in OPVs. The black arrows indicate major routes giving rise to photocurrents, while the gray arrows are related to other possible mechanisms which may account for losses in conversion efficiency, for example, carrier recombination. It should be noted that the exact mechanism of exciton dissociation into mobile charge carriers is still under debate,[80-83] and the square with dashed lines in Fig. 1.4 illustrates one of the possible processes.[84] The individual steps are discussed in detail in the following:

1. Photon absorption. Light is absorbed in hole (donor) or electron (acceptor) transport materials, generating strongly bound electron-hole (e-h) pairs (excitons). The donor material is designed to have LUMO and HOMO levels closer to the vacuum level than those of the acceptor material.
2. Exciton diffusion. To generate mobile carriers, the photogenerated excitons have to be separated at dissociation sites. Therefore, it is crucial for excitons to diffuse to and reach the donor/acceptor interface prior to exciton recombination. Depending on the material, exciton diffusion lengths are about 10–40 nm.[85-87]
3. Dissociation into geminate e-h pairs. It is energetically favorable for charge transfer to occur at the donor/acceptor interface, provided that the energy gain

after the dissociation is larger than the exciton binding energy. Thus, excitons may efficiently[88] dissociate into geminate e-h pairs, resulting in the spatially separated charge carriers.[89] However, electron and hole which reside on two separate molecules are still under the influence of their mutual Coulomb interaction.

4. Dissociation into mobile carriers. It is evident that the dissociation of geminate e-h pairs requires the electric field composed of built-in and applied voltages to overcome the Coulomb attraction. This step is one of the main factors limiting the efficiency of organic solar cells.[90-92]
5. Charge transport and collection. Mobile electrons and holes are transported to the respective electrodes by diffusion and drift.

Also indicated are exciton, exciplex, geminate, and non-geminate recombination, which serve to reduce the conversion efficiency. Specifically, the relaxation of geminate e-h pairs into exciplexes which may be thermally activated to excitons or recombine impedes the geminate e-h pair dissociation.[84]

The predominant strategy to efficiently separate excitons is to have heterojunction structure composed of donor and acceptor materials. The most commonly used geometry is the bulk heterojunction structures which show the best performance. The efficiency of organic bulk heterojunction photovoltaic cells is empirically known to depend significantly on the morphology of the active layer, such as the degree and length scale of phase separation between the donor and acceptor phases.[93-95] One of the major challenges hindering the fabrication of higher efficiency organic photovoltaics, which is beginning to be addressed in this thesis, is the lack of understanding of the morphological effects of donor/acceptor interfaces on device performance.[96,97]

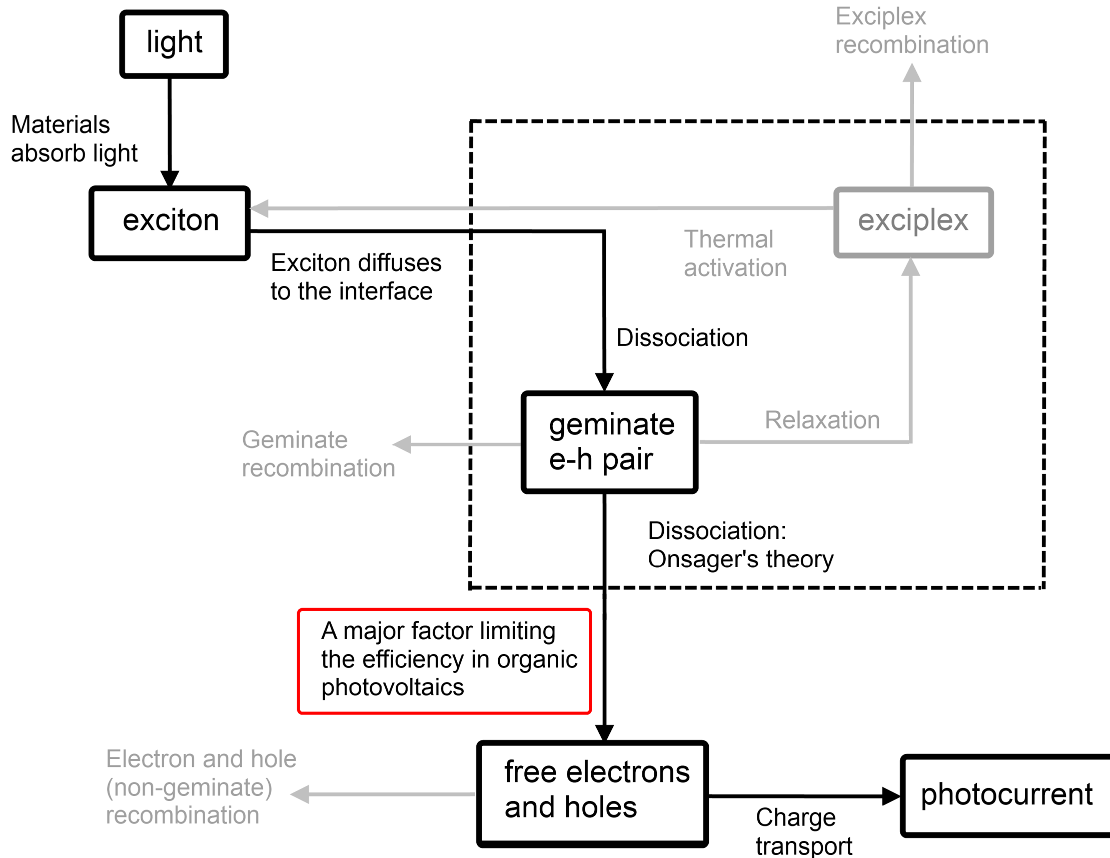

Figure 1.4: Flowchart of major physical processes in organic photovoltaic cells. Black arrows indicate major routes giving rise to photocurrents, while gray arrows are related to competing loss mechanisms. The square with dashed lines illustrates the proposed processes of the exciton dissociation by Morteani *et al*..[84]

1.2 Objective of the work

The objective for the research presented in this thesis is to study electronic properties in organic semiconductor device structures through analytical and numerical device models and to develop a deeper understanding of the physics underlying OFET and OPV operations. Transient phenomena play decisive roles in the performance of

electronic devices and OFETs in particular. First, we investigate theoretically the displacement current and the effects of traps on the establishment and depletion of the conducting channel in OFETs. The device structures explored resemble typical organic thin-film transistors with one of the channel contacts removed. Non-linear numerical and approximate analytical models explain the asymmetry between the current characteristics during carrier injection and extraction observed experimentally. The effects of traps on the charge carrier mobility are studied for several cases with a wide range of trapping time constants. Second, a portion of this thesis is devoted to developing an improved understanding of morphological effects on interfacial recombination in organic bulk heterojunction devices. In bulk heterojunctions, large interfacial areas are of critical importance for device operation. Carrier recombination at the interface is studied with device models for bilayer structures which idealize the island-like morphology of bulk heterojunctions.

1.3 Organization of the thesis

The thesis is organized in the following manner:

Chapter 2 begins with an introduction to the research of transient measurements for characterization of OFETs, and summarizes the results of three published papers: "Conducting channel formation and annihilation in organic field-effect transistor structures," by Y. Liang, C. D. Frisbie, H.-C. Chang, and P. P. Ruden, *J. Appl. Phys.* **105**, 024514 (2009); "Transient effects controlling the charge carrier population of organic field effect transistor channels," by H.-C. Chang, P. P. Ruden, Y. Liang, and C. D. Frisbie, *J. Appl. Phys.* **107**, 104502 (2010); "Examination of Au, Cu, and Al contacts in organic field-effect transistors via displacement current measurements," by Y. Liang, H.-C. Chang, P. P. Ruden, and C. D. Frisbie, *J. Appl. Phys.* **110**, 064514 (2011). We present measurements of displacement current and device models exploring the dynamics of the formation and depletion of the conducting channels. By measuring the displacement current through an OFET-like device with only one channel contact, transient carrier

transport in organic semiconductors may be studied. Analytical and numerical results are compared to the experimental data. The observed asymmetric characteristics of current versus time in the experiments are explained by three analytical models and verified by the complete numerical model. The complete numerical model is also used to explore the effects of traps in a wide range of trapping parameters. When carriers are injected into the device, a conducting channel is established while traps, which are initially empty, are being populated. The filling of the traps then modifies the transport characteristics of the injected charge carriers. In contrast, dc experiments as they are typically performed to characterize the transport properties of organic semiconductor channels investigate a steady state with traps partially filled. My collaborators, Dr. Yan Liang and Prof. C. Daniel Frisbie, contributed the experimental data presented in this chapter.

Major parts of Chapter 3 have been published as "Charge carrier extraction dynamics for organic field effect transistor structures," by H.-C. Chang, P. P. Ruden, Y. Liang, and C. D. Frisbie, *Appl. Phys. Lett.* **99**, 073306 (2011). We present experimental data and a model for charge carrier extraction from the channel of the same device structure as in Chapter 2. The initially accumulated channel is depleted by a sudden change of the gate voltage. The measured discharge current transient decreases either as a power law or exponentially if the final state of the channel is completely or partially depleted, respectively. The extraction process is modeled with a capacitor/resistor circuit with a time-dependent resistance that increases with decreasing channel carrier density. Analytical and numerical results are discussed and compared with the experimental data. The experimental results presented in the chapter were contributed by my collaborators, Dr. Yan Liang and Prof. C. Daniel Frisbie.

Chapter 4 begins an exploration of geometric effects on interfacial recombination. In organic bulk heterojunction photovoltaic cells, large interfacial areas that impact the efficiency of the electron-hole pair dissociation are of critical importance for device performance. Instead of the electron-hole pair dissociation, the related process of the carrier recombination at the interface is studied for two simple bilayer structures with interfaces perpendicular and parallel to the current direction. Recombination currents are

found to depend rather sensitively on the geometry. Time scales of interfacial recombination process and carrier transport are useful concepts in this context.

The last chapter, Chapter 5, gives brief summaries and provides avenues for the future work. In transient measurements of OFETs, modifying the gate voltage profiles promises to yield more detailed information about traps and calculated preliminary results are presented. In the work relevant to the effect of morphology on carrier recombination, it is necessary to learn more about the issue of carrier balance for both bilayer structures. Furthermore, an analytical expression for the average interfacial recombination coefficient as a function of morphological parameters is desirable for the eventual formulation of a simple one-dimensional model.

In Appendix A, we explore the hopping transport in disordered semiconductors. In Appendix B, the detailed description of the numerical method applied in the device model for the displacement current experiments is provided. The carrier density is discretized with correlated position and time intervals. In Appendix C, the derivation of analytical solutions for the non-linear resistor-capacitor model is presented. Depending on the gate voltage profiles and initial conditions, different characteristics of the displacement current as a function of time are obtained. In Appendix D, we present the numerical method for calculating interfacial recombination currents in the bilayer structure with interface parallel to the current direction. Analytical solutions of interfacial carrier densities reduce the calculation time significantly.

2 Transient charge carrier transport effects in OFET channels

2.1 Introduction and motivation

Organic semiconductors (OSCs) are among the most promising materials for novel electronics. Many electronic devices have been fabricated from conjugated organic hydrocarbons, and some are already commercialized.[18,98] Organic semiconductors are primarily small molecules and conjugated polymers. Pentacene, for example, is one of the most widely used p-type organic semiconductor materials among the small molecules.[99-102]

For carrier transport in organic materials, the trapping/detrapping of mobile charge carriers is an important issue that can even play the dominant role in device performance. Frequently, organic field effect transistors (OFETs) are used to characterize the electrical properties of OSCs.[27,33] One usually measures the dc current through the conducting channel as a function of the applied gate-to-source and drain-to-source voltages and obtains a steady state charge carrier field effect mobility. However, the transient processes, including the formation and depletion of the conducting channel, are not explored in these experiments. Moreover, the steady state mobility is measured with traps partially filled and the dynamic effects of traps do not manifest themselves directly. On the other hand, transient measurements can provide information about the dynamics of carrier trapping phenomena. An effective mobility that characterizes transient experiments is measured when trapping effects are in process and the fractional frap filling changes.

Several techniques have been introduced to investigate transient carrier transport in OFETs. Time-resolved microscopic optical second-harmonic generation (TRM-SHG)[103-106] is one of them, which is used by the Iwamoto group to study transient carrier

transport before the conducting channel is established. In TRM-SHG experiments, drain and gate contacts are grounded, with a voltage pulse generating charge carriers which move from source to drain. Detectors in TRM-SHG can directly visualize the movement of carriers since the SHG signal is sensitive to the large lateral electric field in the channel. It is found that inefficient injection led to a high lateral electric field at the contact edge. Transient carrier transport and effects of traps are discussed in a recent publication.[106]

Another method to study the transient charge carrier transport is the modified time-of-flight (MTOF) experiment proposed by the Dodabalapur group.[107-110] Similar to TRM-SHG, a voltage pulse at the source generates and moves carriers toward the drain at which transient currents are measured. It is found that the transient mobility is typically larger than the field effect mobility obtained from the dc measurements.[111]

Displacement current measurement (DCM) is also a useful technique to study transient effects in OFETs. DCM was first introduced by Egusa et al. to explore carrier injection in organic light emitting diodes (OLEDs).[112,113] Thereafter, several research groups further developed and used this technique to investigate charge carrier transport in OFETs,[114-123], OLEDs,[124-126] and organic photovoltaic cells.[127] The first report regarding the carrier injection characteristics of OFETs by DCM was published by the Niwano group.[114-116] The Majima group also uses DCM technique in OFETs extensively.[117,120] The channel length of their fabricated devices is much smaller than the overlapping distance between channel contacts and organic semiconductor layer. Thus, they focus on issues of carrier injection and extraction but neglect the transient carrier transport in the channel. However, in displacement current experiments the basic physics of transient charge carrier transport in OFET channels was not well understood at the beginning of this project.

The goal of this project was to develop appropriate physical models for the DCM technique, and to use these models to explain experimental data[128] for the transient carrier transport in OFET channels. When one linearly sweeps the gate voltage and measures the displacement current running through the gate electrode with source and drain grounded, a puzzling current peak in the carrier injection process is always observed.

Compared with TRM-SHG and MTOF, DCM has several advantages. First, the experimental setup of DCM is relatively simple, and electrical signal is easy to detect with optimized device structures. Second, transient carrier injection and extraction can be studied, as well as the effects of traps, providing much information about the dynamics of carrier trapping/detrapping events. Third, the number of injected, extracted, and trapped carriers can be calculated by integrating the displacement (charging and discharging) current with respect to time.

2.2 Device structure and experimental method

In the displacement current measurements, a two-terminal device structure resembling a simplified field effect transistor with one of the channel contacts removed, as shown in Fig. 2.1(a), is used. Under suitable bias a conducting channel is established in the device. Since the channel length is on the order of millimeters, charge carriers take a relatively long time to reach the far end of the device after having been injected by the channel contact. Transient effects that occur on a time scale comparable to the transit time may readily be explored.

The schematics of the device geometry are shown in Figs. 2.1(a) and 2.1(b).[129] A heavily doped p-type silicon wafer with 300 nm thick thermal oxide layer serves as the substrate. On top of the silicon oxide, a 30 nm thick pentacene film is thermally evaporated. The width (W) of the pentacene strip is 0.5 mm. The pentacene channel length (L) is defined as shown in Fig. 2.1(b). A typical value is 6 mm. A 40 nm gold layer with an area of 0.5×0.7 mm^2 is deposited on the pentacene by thermal evaporation while the substrate is water-cooled. The overlapping area between the gold contact and the pentacene strip is kept as small as possible but large enough to make good contact.

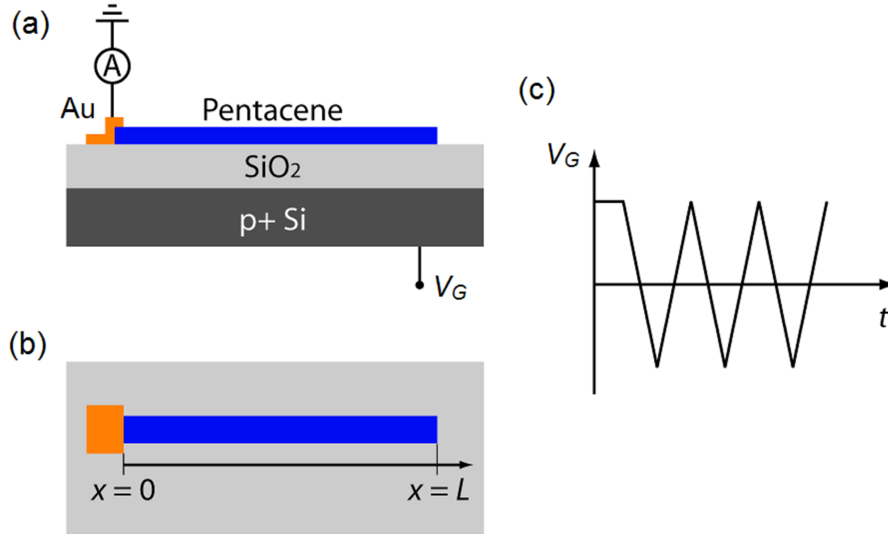

Figure 2.1 (Courtesy of Yan Liang): (a) Schematic cross section of the device structure. (b) Schematic top view of the device. (c) Consecutive voltage sweeps applied to the bottom (gate) electrode voltage.

Electrical characterization is carried out by measuring the displacement current (I) running through the grounded top electrode while linearly sweeping the bottom electrode voltage (V_G). $V_G(t)$ is taken to follow a simple zigzag time profile with sweep rates of µ5.7 Vs^{-1}. In addition, we may sweep the gate voltage consecutively in the measurement, as shown in Fig. 2.1(c). The measured displacement current of the first sweep is plotted as a function of time and voltage in Figs 2.2 and 2.3, respectively. The capital letters in both plots refer to the same time ranges. At the beginning of the forward sweep we start with a positive voltage which decreases as a function of time. As long as it remains positive, only a small displacement current associated with the capacitance of the contact is measured (region A). This current is given by

$$I = dQ/dt = d(C_0 V_G)/dt = C_0 \cdot dV_G/dt = C_0 \cdot r_V \,, \tag{2.1}$$

where Q is the amount of charge accumulated under the contact, C_0 is the effective capacitance associated with the contact, and r_V is the sweep rate.

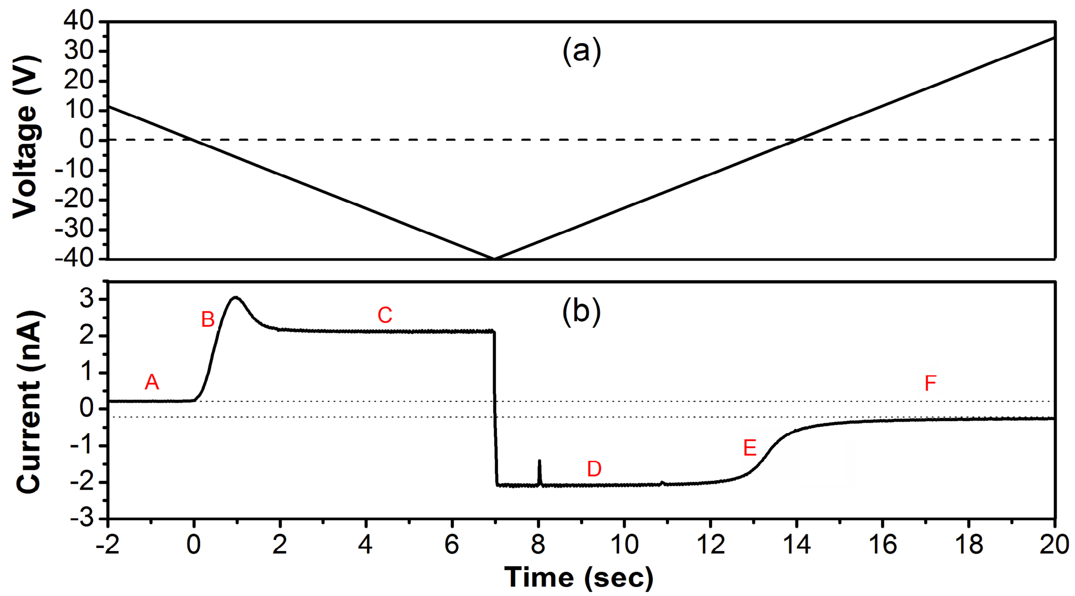

Figure 2.2: (a) Applied gate voltage versus time. (d) Measured *I* versus *t* characteristics (solid curve) and displacement current associated with the contact (dotted line).

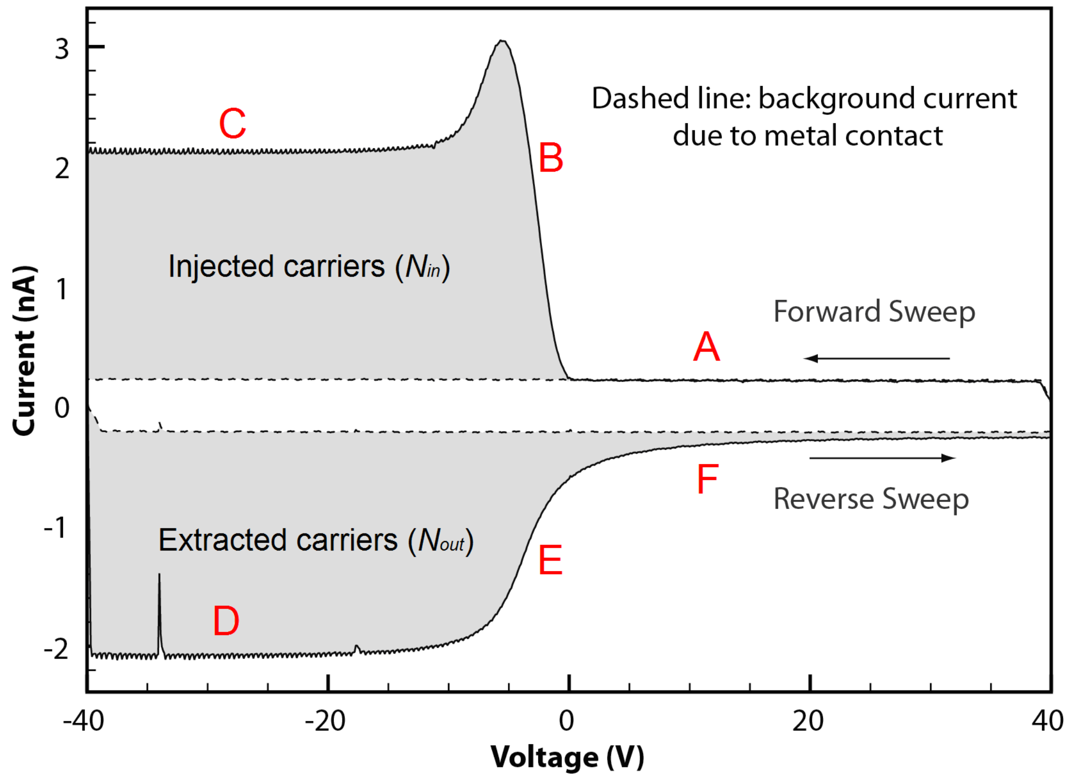

Figure 2.3 (Courtesy of Yan Liang): Measured *I* versus V_G characteristics (solid curve) and displacement current associated with the contact (dotted line).

Since the overlapping area between the contact and pentacene is small, and the thickness of pentacene is much smaller than that of silicon oxide, C_0 approximately equals $\varepsilon_0 \varepsilon'_{SiO_2} A_{Au} / d_{SiO_2}$, where ε_0 is the vacuum permittivity, ε'_{SiO_2} is the relative permittivity of SiO_2, A_{Au} is the area of the contact, and d_{SiO_2} is the thickness of the SiO_2 layer.

Beginning at $t = 0$ (region B), holes are injected into the device as the gate voltage becomes negative. In other words, the pentacene strip (capacitor) is being charged with holes. In this region, a peak is observed due to the transient process of conducting channel formation. Essentially, holes injected from the contact are driven toward the other end of the pentacene strip (in the *x*-direction) and populate the channel. Once holes are distributed uniformly at the pentacene/SiO_2 interface, a conducting channel is established and the displacement current becomes constant (region C). The constant current here is given by $I = C_1 \cdot r_V$, where C_1 is the new effective capacitance determined by the area of contact and pentacene (A_{pen}) combined, i.e. $C_1 = \varepsilon_0 \varepsilon'_{SiO_2} \left(A_{Au} + A_{pen} \right) / d_{SiO_2}$. We refer to the time period after which holes begin to be injected but before the current becomes constant, as the transient region. The time scale of this transient region is on the order of 1 s.

At the beginning of the reverse sweep, the sweep rate changes to a positive value (at $t = 7$ s in Fig. 2.2), the sign of the displacement current changes but the absolute value of the current is equal to that at the end of the forward sweep (region D). As the gate voltage continues to increase, holes are extracted out of the channel. During this time period, the current gradually decreases in magnitude, and the conducting channel is disappearing (region E). After the gate voltage becomes positive again and the pentacene channel no longer conducts, there is still a small amount of current in addition to the displacement current associated with the contact. This additional current is due to the emission of trapped holes (region F).

For the following discussion, we choose to plot I versus $V(t)$ in most cases.

2.2.1 Carrier injection and extraction

One may calculate the number of carriers injected into and extracted out of the channel in a complete sweep by integrating the displacement current with respect to time. The difference between the former and latter is the number of carriers trapped in the channel after one cyclic sweep. As shown in Fig. 2.3, the number of carriers injected into the pentacene channel during the forward sweep is given by

$$N_{in} = \left| \frac{1}{er_V} \int_{V_1}^{V_2} (I_f - I_f^{Au}) dV \right| = \left| \frac{1}{e} \int_{t_1}^{t_2} (I_f - I_f^{Au}) dt \right|, \qquad (2.2)$$

where e is the elementary charge, $t_1 = V_1/r_V$ and $t_2 = -V_2/r_V$ are the starting and ending time for the forward sweep, I_f is the displacement current in the forward sweep, and I_f^{Au} is the displacement current associated with the contact in the forward sweep. The number of carriers extracted from the pentacene channel in the reverse sweep is given by

$$N_{out} = \left| \frac{1}{er_V} \int_{V_1}^{V_2} (I_r - I_r^{Au}) dV \right| = \left| \frac{1}{e} \int_{t_2}^{t_1+t_2} (I_r - I_r^{Au}) dt \right|, \qquad (2.3)$$

where I_r is the displacement current during the reverse sweep, and $I_r^{Au} = -I_f^{Au}$ is the displacement current associated with the contact in the reverse sweep. Thus, the average trapped carrier concentration at the end of one cyclic sweep is given by

$$\overline{p}_{trap} = (N_{in} - N_{out}) / A_{pen} \,. \qquad (2.4)$$

Figure 2.4 shows the I versus V characteristics obtained from three consecutive cyclic sweeps, and Table 2.1 lists the average injected, extracted, and trapped carrier concentrations for each cyclic sweep. The average trapped carrier concentration of the

first sweep is about five times larger than that of the second sweep, indicating that most traps are filled in the first sweep. The negative threshold shift of carrier injection in the second sweep is attributed to the carriers trapped after the first sweep. The threshold shift for the second and the third sweeps is much smaller because fewer carriers are trapped in the second sweep than in the first sweep, as shown in Table 2.1. No obvious relationship is observed between the average trapped carrier concentration and the channel length, implying that the former is mainly controlled by the trap states distributed throughout the length of the channel, and not concentrated at the contact or the end of the strip.

	Injected ($\times 10^{12}$ cm^{-2})	Extracted ($\times 10^{12}$ cm^{-2})	Trapped (cm^{-2})	Trapped (%)
First sweep	2.80	2.64	1.61×10^{11}	5.76
Second sweep	2.65	2.62	3.02×10^{10}	1.14
Third sweep	2.62	2.60	2.63×10^{10}	1.00

Table 2.1 (Courtesy of Yan Liang): Average injected, extracted, trapped carrier concentration, and percentage of trapped carriers over total injected carriers in each sweeps.

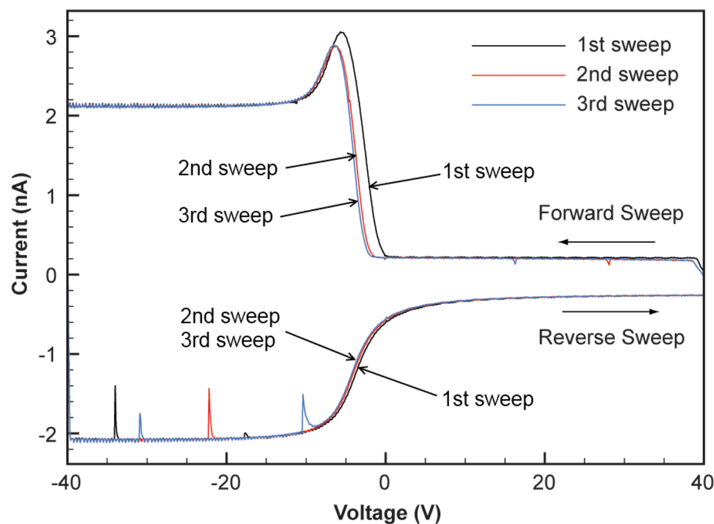

Figure 2.4 (Courtesy of Yan Liang): Displacement current measured in three consecutive sweeps.

2.3 Conducting channel formation and depletion

In the following discussion, we present device models[130] exploring the asymmetric current characteristics between injection and extraction process, and the effects of traps during transient processes in the conducting channel of OFETs. Numerical and approximate analytical models for the formation and depletion of the conducting channel and the resulting displacement current are discussed. We show that displacement current measurements on OFET structures provide unique opportunities for the study of trap dynamics involving a wide range of time scales. In agreement with the structures explored experimentally all the calculated results assume a specific channel capacitance (C') of 11.5 $nF \cdot cm^{-2}$, a channel length (L) of 6 mm, a width of the pentacene strip (W) of 0.5 mm, and sweep rates r_V of $\mu 5.7\ Vs^{-1}$.

2.3.1 Geometric model

One may understand qualitatively the transient displacement current versus gate voltage characteristics on the basis of an analytical geometric model, assuming the effects associated with traps are negligible. The model considers only drift current. Hence, it works when the diffusion current is negligible compared with the drift current, i.e., when the voltage drop along the channel is much larger than kT/e, where k is the Boltzmann constant and T is the temperature. At the start of carrier injection, at time t the hole concentration at $x = 0$, i.e. at the contact, is given by

$$p(0,t) = (C'/e)|r_V|t\ . \qquad (2.5)$$

As shown in Fig. 2.5(a), the hole concentration is assumed to decrease linearly to zero over a distance

$$l = \mu E t \,. \tag{2.6}$$

The hole density profile is thus a triangle. Using the relationship between the electric field and the hole density gradient, $E = |r_V| t / l$, one finds:

$$l = (\mu |r_V|)^{(1/2)} t \,. \tag{2.7}$$

After combining Eqs. (2.5)–(2.7), the total injected hole concentration and displacement current at time *t* are given by:

$$P(t) = (1/2) l p(0,t) = (1/2)(C'/e)|r_v|^{3/2} \mu^{1/2} t^2 \,, \tag{2.8}$$

$$I(t) = eW \frac{d}{dt} P(t) = WC' |r_V|^{3/2} \mu^{1/2} t \,. \tag{2.9}$$

The current rises linearly with time. In this model the linear rise is expected to continue until $l(t = \Delta t) = 2L$, and the current at $t = \Delta t$ is equal to $C' |r_V| 2LW$, where $\Delta t = 2L / \sqrt{\mu |r_V|}$. When $t > \Delta t$, the hole concentration becomes uniform over the full length of the strip shown in Fig. 2.5(b), and the current drops discontinuously to half the value of that at $t = \Delta t$:

$$P(t > \Delta t) = L \cdot p(t > \Delta t) = (LC'/e)|r_V| t \,, \tag{2.10}$$

$$I(t > \Delta t) = C' |r_V| LW \,. \tag{2.11}$$

Obviously, this simplified model has considerable deficiencies. However, it illustrates well the origin of the current peak observed when holes begin to enter the pentacene strip. For the full range of the charge injecting voltage sweep, the displacement current is given by:

$$I(t)=\begin{cases} WC'|r_V|^{3/2}\mu^{1/2}t, & t<\Delta t \\ WLC'|r_V|, & t>\Delta t \end{cases}. \tag{2.12}$$

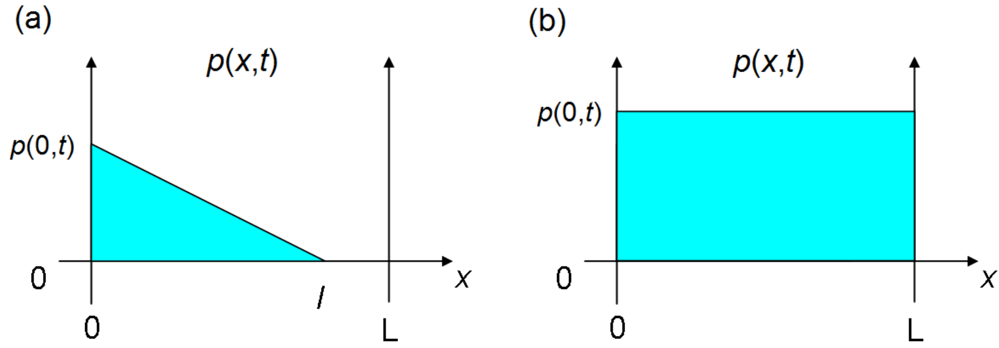

Figure 2.5: (a) Carrier density profile in the channel at the beginning of carrier injection. (b) When $t > \Delta t$, carrier concentration is constant over the channel.

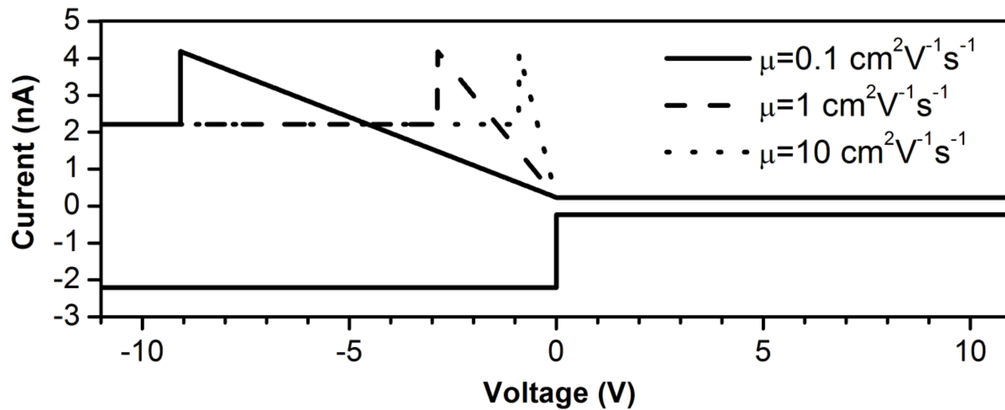

Figure 2.6: *I-V* curves calculated with the geometric model for structures with different mobilities and no traps.

Figure 2.6 shows the *I-V* characteristics of the geometric model for different mobility values. During the reverse sweep, the channel remains conducting and the channel field is small until almost all charge carriers have been extracted. The current during the charge extracting sweep is essentially independent of the mobility. This simple model explains qualitatively the lack of symmetry between currents measured

during channel formation and channel depletion. In addition, there are no threshold voltage shifts without traps, and therefore the reverse sweep currents of the three cases shown are the same.

The slope of *I-t* or *I-V* curve in transient region ($0 < t < \Delta t$),

$$dI/dt = WC'|r_V|^{3/2}\mu^{1/2}, \tag{2.13}$$

$$dI/dV = WC'|r_V|^{1/2}\mu^{1/2}, \tag{2.14}$$

is proportional to the square root of the mobility in this model. As a result, we may define an effective mobility as given by the slope of the transient region through

$$\mu_{eff} = (dI/dt)^2/(W^2C'^2|r_V|^3) = (dI/dV)^2/(W^2C'^2|r_V|). \tag{2.15}$$

To further justify the focus on the drift current contribution, we display in Table 2.2 the relevant time scales for three different mobility values. Evidently, diffusion is too slow a process to be relevant with the voltage ramp rates and other device parameters adopted here.

	Δt	$L^2/(\mu \cdot r_V \Delta t)$	$L^2/(kT\mu/e)$
$\mu = 0.1$ cm^{2}V^{-1}s^{-1}	1.585 s	1.1256 s	144 s
$\mu = 1$ cm^{2}V^{-1}s^{-1}	0.5 s	0.126 s	14.4 s
$\mu = 10$ cm^{2}V^{-1}s^{-1}	0.158 s	0.0126 s	1.44 s

Table 2.2: Time scales for different carrier transport effects in transient process.

2.3.2 Spatially averaged carrier density model

In the spatially averaged carrier density model, we consider the situation in which the transient spatial redistribution of the carriers in the channel plays a negligible role. This is obviously the case when the channel transit time is very short compared with the time scale of the measurement, i.e., the carrier mobility is high and/or the channel length is short. Thus, we may average the mobile hole concentration over the channel length,

$$\overline{p}(t) = \frac{1}{L}\int_0^L p(x,t)dx\,. \tag{2.16}$$

In this model, we also allow for the possible trapping of injected holes. The spatially averaged trapped hole concentration is given by,

$$\overline{p}_T(t) = \frac{1}{L}\int_0^L p_T(x,t)dx\,. \tag{2.17}$$

Consequently, the divergence of the current density is constant,

$$J(x,t) = e\frac{\partial}{\partial t}\int_x^L \;[p(x',t) + p_T(x',t)]dx' \approx e(L-x)\frac{\partial}{\partial t}[\overline{p}(t) + \overline{p}_T(t)]\,, \tag{2.18}$$

$$\frac{\partial}{\partial x}J(x,t) \approx -e\frac{\partial}{\partial t}[\overline{p}(t) + \overline{p}_T(t)] = -\frac{\partial}{\partial t}[C'V(t)] = -C'|r_V|\,. \tag{2.19}$$

According to the continuity equation,

$$\frac{d}{dt}\overline{p} = -\frac{1}{e}\frac{\partial J}{\partial x} - \frac{d}{dt}\overline{p}_T = \frac{C'|r_V|}{e} - \tilde{c}N_T\overline{p} + \tilde{e}\;\overline{p}_T\,, \tag{2.20}$$

$$\frac{d}{dt}\overline{p}_T = \tilde{c}\;N_T\overline{p} - \tilde{e}\;\overline{p}_T\,, \tag{2.21}$$

where the averaged density of trapped holes is controlled by the total (sheet) density of traps (N_T), the capture coefficient ($\tilde{c}$), and the emission coefficient ($\tilde{e}$).[131] We define the capture and emission time constants as follows:

$$\tau_{cap} = \frac{1}{\tilde{c} N_T}, \qquad \tau_{emi} = \frac{1}{\tilde{e}}. \tag{2.22}$$

Equations (2.20) and (2.21) are coupled ordinary linear differential equations. The remaining problem is straightforward to solve by Laplace transform. With the assumed initial values for $\overline{p}(t)$ and $\overline{p}_T(t)$ are both zero, $\overline{p}(t)$ and $\overline{p}_T(t)$ in the forward region of the first sweep are found to be

$$\overline{p}(t) = \frac{C'|r_V|}{e(\tilde{e} + \tilde{c}N_T)} \left[\tilde{e}t - \frac{\tilde{c}N_T}{\tilde{e} + \tilde{c}N_T} (e^{-(\tilde{e}+\tilde{c}N_T)t} - 1) \right], \tag{2.23}$$

$$\overline{p}_T(t) = \frac{C'|r_V|t}{e} - \overline{p}(t) = \frac{C'|r_V|}{e} \frac{\tilde{c}N_T}{\tilde{e} + \tilde{c}N_T} \left[t + \frac{1}{\tilde{e} + \tilde{c}N_T} (e^{-(\tilde{e}+\tilde{c}N_T)t} - 1) \right], \tag{2.24}$$

$$\overline{p}(t) + \overline{p}_T(t) = \frac{C'|r_V|}{e} t. \tag{2.25}$$

We define the reverse sweep as starting at $t = t_p$. The corresponding initial conditions are

$$\overline{p}(t'=0) = \overline{p}(t = t_p) = \overline{p}(t_p), \tag{2.26}$$

$$\overline{p}_T(t'=0) = \overline{p}_T(t = t_p) = \overline{p}_T(t_p), \tag{2.27}$$

$$t = t' + t_p. \tag{2.28}$$

$\overline{p}(t')$ and $\overline{p}_T(t')$ in the reverse sweep then are

$$\bar{p}(t') = \frac{C'|r_V|}{e}\frac{\tilde{c}N_T}{\tilde{e}+\tilde{c}N_T}\left[-\frac{\tilde{e}}{\tilde{c}N_T}t' + \frac{1}{\tilde{e}+\tilde{c}N_T}(e^{-(\tilde{e}+\tilde{c}N_T)t'}-1)\right] + \frac{1}{\tilde{e}+\tilde{c}N_T}\{\tilde{e}[\bar{p}(t_p)+\bar{p}_T(t_p)] + [\tilde{c}N_T\bar{p}(t_p) - \tilde{e}\bar{p}_T(t_p)]e^{-(\tilde{e}+\tilde{c}N_T)t'}\}, \quad (2.29)$$

$$\bar{p}_T(t') = -\frac{C'|r_V|}{e}\frac{\tilde{c}N_T}{\tilde{e}+\tilde{c}N_T}\left[t + \frac{1}{\tilde{e}+\tilde{c}N_T}(e^{-(\tilde{e}+\tilde{c}N_T)t}-1)\right] + \frac{\tilde{c}N_T}{\tilde{e}+\tilde{c}N_T}[\bar{p}(t_p)+\bar{p}_T(t_p)] + \frac{\tilde{e}\bar{p}_T(t_p) - \tilde{c}N_T\bar{p}(t_p)}{\tilde{e}+\tilde{c}N_T}e^{-(\tilde{e}+\tilde{c}N_T)t'}, \quad (2.30)$$

$$\bar{p}(t') + \bar{p}_T(t') = \bar{p}(t_p) + \bar{p}_T(t_p) - \frac{C'|r_V|}{e}t'. \quad (2.31)$$

Figure 2.7 shows how the average mobile and trapped hole concentrations change with trapping parameters. To limit the parameter space we discuss only cases for which $\tilde{e} = \tilde{c}N_T$. When the time *t* is much greater than $1/(\tilde{e}+\tilde{c}N_T)$, the mobile and trapped hole concentration increase linearly and they are equal because the capture and emission time constants have been chosen to be the same. When the time is comparable to $1/(\tilde{e}+\tilde{c}N_T)$ the exponential terms in Eqs. (2.23) and (2.24) play a role and the fraction of the mobile hole concentration $\bar{p}(t)/[\bar{p}(t)+\bar{p}_T(t)]$ changes with time at the beginning of the voltage sweep. The ratio is near unity initially but decreases to a constant less than unity when trapping/detrapping events balance.

Figure 2.8 shows the resulting *I-V* characteristics for the same trapping parameters as in Fig. 2.7. There are threshold voltage shifts in the reverse sweep because of partial trap filling. Threshold shift corresponds to the time t'_{th} at which $\bar{p}(t'_{th}) = 0$. In other words, the threshold voltage shifts in the extracting sweep are due to different densities of trapped holes. The smaller the trapping time, the larger the concentration of trapped holes, and the greater the resulting threshold voltage shift. Beyond the threshold, only the emission of trapped holes remaining in the channel contributes to the displacement current, and the trapped hole concentration decreases exponentially with emission time constant (τ_{emi}).

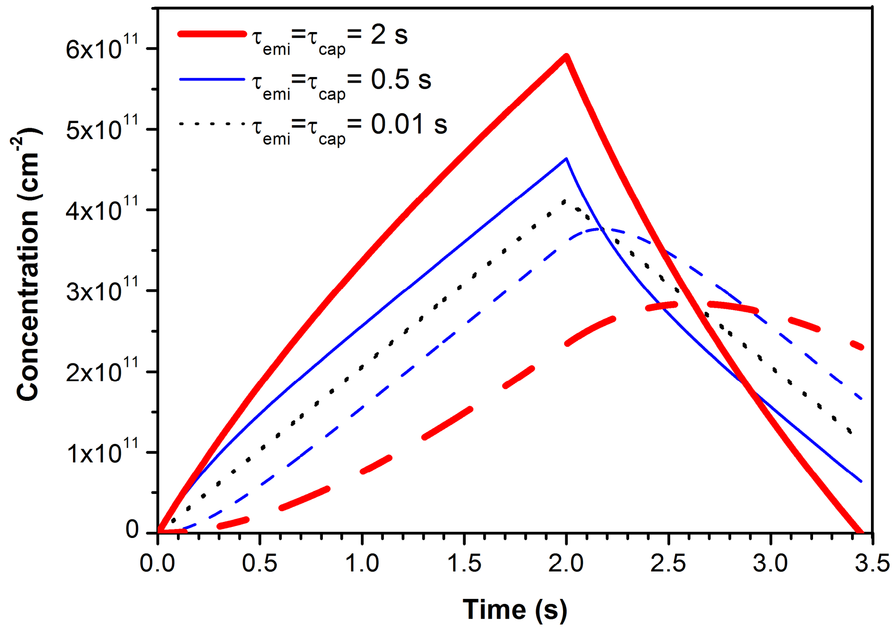

Figure 2.7: Hole concentrations calculated with the spatially averaged charge carrier model. The injecting sweep starts at $t = 0$ and the extracting sweep begins after $t = 2$ s. The thicker solid and dashed lines represent mobile and trapped hole concentrations for $\tau_{cap} = \tau_{emi} = 2$ s. The thinner solid and dashed lines represent mobile and trapped hole concentrations for $\tau_{cap} = \tau_{emi} = 0.5$ s. The dotted line represents both mobile and trapped hole concentrations for $\tau_{cap} = \tau_{emi} = 0.01$ s.

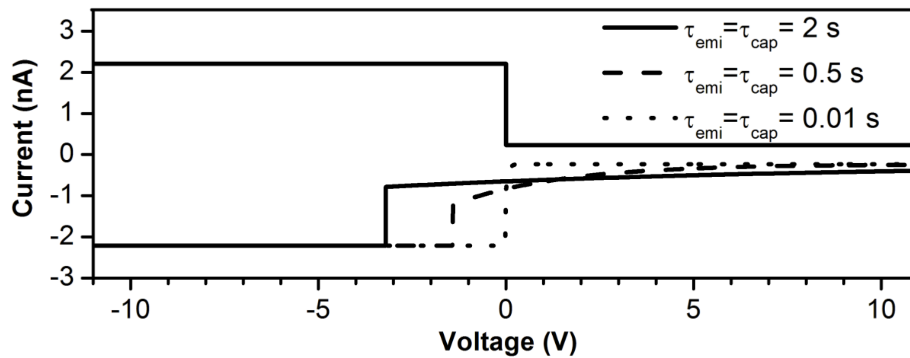

Figure 2.8: *I-V* curves calculated with the spatially averaged carrier density model.

In contrast with the geometric model, the spatially averaged carrier density model does not explain the current peak observed when carriers are injected. This current peak, therefore, is attributed to the non-linearity associated with spatial redistribution of the charge carriers. However, the model considered here does shed light on the effects of traps.

2.3.3 Resistor-capacitor model

To describe the transient carrier transport in the charging and discharging experiments, it proved to be useful also to develop a non-linear resistor-capacitor equivalent circuit model in which the resistance changes with the carrier density, as shown in Fig. 2.9. Thus, the resistance decreases with increasing potential difference across the capacitor during carrier injection. The displacement current (for $t > 0$) is given by

$$I(t) = WLC'\frac{dV_C(t)}{dt} = \frac{V_G(t) - V_C(t)}{R_{ch}(t)} = \frac{V_G(t) - V_C(t)}{L/[We\mu \cdot p(t)]}, \tag{2.32}$$

where the channel resistance, $R_{ch}(t)$, is assumed to be inversely proportional to the density of mobile holes, $p(t)$. Assuming that effects of traps are negligible, $p(t)$ is linearly proportional to the potential across the capacitance,

$$ep(t)WL = \begin{cases} -CV_C(t), & V_C(t) < 0 \\ 0, & V_C(t) \geq 0 \end{cases}, \tag{2.33}$$

where the threshold voltage is set to zero.

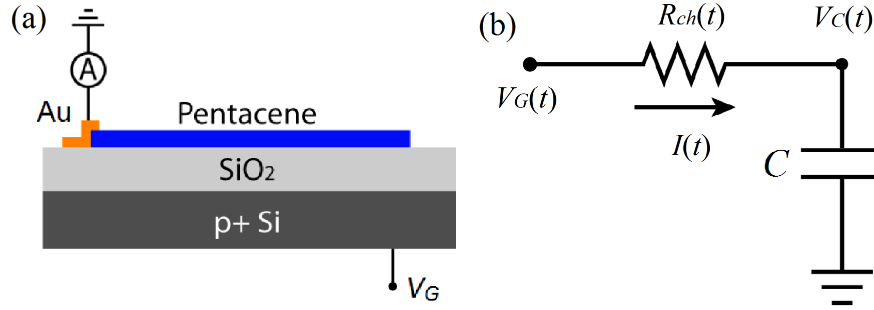

Figure 2.9: (a) Schematic cross section of the device structure. (b) The resistor-capacitor equivalent circuit model with time-dependent channel resistance, $R_{ch}(t)$, and constant capacitance (C).

After combining Eqs. (2.32) and (2.33),

$$\frac{dV_C}{dt} = \frac{\mu}{L^2}[(V_C)^2 - V_G V_C]\,. \tag{2.34}$$

Under conditions which represent carrier injection (charging),

$$\begin{aligned} V_G(t=0) &= V_C(t=0) = 0 \\ V_G(t>0) &= -|r_V|t \end{aligned}\,. \tag{2.35}$$

The analytical solution of $V_C(t)$ may be obtained,

$$V_C(t) = -|r_V| \cdot \left[t - \exp\left(-\frac{\mu|r_V|}{L^2}\frac{t^2}{2}\right)\int_0^t \exp\left(\frac{\mu|r_V|}{L^2}\frac{t'^2}{2}\right)dt' \right], \tag{2.36}$$

The current consequently is given by:

$$I(t) = WLC'\frac{dV_C(t)}{dt} = -\frac{r_V{}^2 \mu W C'}{L} t \exp\left(-\frac{\mu|r_V|}{L^2}\frac{t^2}{2}\right)\int_0^t \exp\left(\frac{\mu|r_V|}{L^2}\frac{t'^2}{2}\right)dt'\,. \tag{2.37}$$

With carrier extraction beginning at $t = t_p$, the corresponding initial conditions are

$$\begin{aligned} &V_G(t=t_p) = V_C(t=t_p) = V_p \\ &V_G(t>t_p) = V_p + |r_V|\tilde{t} \qquad , \\ &t = \tilde{t} + t_p \end{aligned} \tag{2.38}$$

where V_p is a negative constant and $I(t = t_p)$ is assumed to be zero. The voltage of the capacitor and the current in the carrier extraction (discharging) process are

$$V_C(\tilde{t}) = -|V_p| + |r_V| \cdot \left[\tilde{t} - \exp\left(\frac{\mu|r_V|}{L^2}\frac{\tilde{t}^2}{2} - \frac{\mu|V_p|}{L^2}\tilde{t}\right)\int_0^{\tilde{t}} \exp\left(-\frac{\mu|r_V|}{L^2}\frac{t'^2}{2} + \frac{\mu|V_p|}{L^2}t'\right)dt' \right], \tag{2.39}$$

$$I(\tilde{t}) = WC'|r_V|\left(-\frac{\mu|r_V|}{L}\tilde{t} + \frac{\mu|V_p|}{L}\right)\exp\left(\frac{\mu|r_V|}{L^2}\frac{\tilde{t}^2}{2} - \frac{\mu|V_p|}{L^2}\tilde{t}\right)\int_0^{\tilde{t}} \exp\left(-\frac{\mu|r_V|}{L^2}\frac{t'^2}{2} + \frac{\mu|V_p|}{L^2}t'\right)dt'. \tag{2.40}$$

Detailed derivations of Eqs. (2.36)–(2.40) are presented in Appendix C.

Figure 2.10 shows the resulting *I-V* characteristics for three different values of charge carrier mobility. Consistent with the geometric model of Fig. 2.6, higher mobilities yield smaller transient regions. At the beginning of the charging process, the channel resistance is so large that the channel capacitor is charged with carriers at a relatively slow rate, i.e., V_C stays closed to zero, and V_C and R_{ch} are almost constant. However, the gate voltage increases linearly with time and therefore, the charging current also increases linearly with time, as shown in the transient region of carrier injection in Fig. 2.10. Subsequently, as the channel capacitance is charged, the channel resistance gradually decreases. At the end of the transient region, the channel capacitance is sufficiently charged that the channel resistance decreases to such a small value that the charging current becomes constant, i.e., V_C and V_G both increase linearly with time almost at the same rate. In other words, for $0 < t < t_p$, when $t << R_{ch}C$, the charging current increases linearly with time, but becomes constant when $t >> R_{ch}C$.

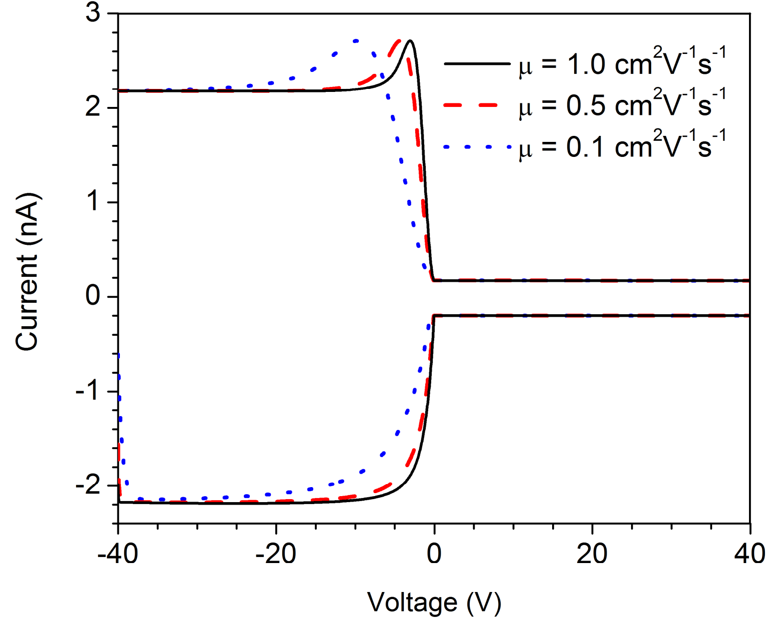

Figure 2.10: Calculated *I-V* characteristics using different hole mobilities in the resistor-capacitor model.

2.3.4 Numerical device model

In order to include the carrier dynamics, one has to formulate a complete model.[132] As shown in Fig. 2.1(b), the *x*-axis is parallel to the pentacene strip with its origin at the edge of gold contact. The gradual channel approximation is applicable because the device's lateral dimensions are very large compared with the oxide thickness. For the devices discussed here, the threshold voltage of the pristine devices (first sweep) is very near zero. (Subsequent sweeps, however, may be affected by trapped holes of previous sweeps as seen in Fig. 2.4). The local charge in the channel is proportional to the local voltage drop across the SiO_2,

$$V(x,t) = -[V_G - V_{channel}(x,t)], \tag{2.41}$$

$$e[p(x,t) + p_T(x,t)] = C'V(x,t) \qquad \text{for } V(x,t) \geq 0, \tag{2.42}$$

where $p(x,t)$ is the sheet concentration of mobile holes, $p_T(x,t)$ is the sheet concentration of trapped holes, C' is the SiO_2 capacitance per unit area, and $V(x,t)$ is the voltage difference between the channel and bottom electrode. The lateral electric field in the channel is

$$E(x,t) = -\frac{\partial V_{channel}(x,t)}{\partial x} = -\frac{\partial V(x,t)}{\partial x} = -\frac{e}{C'}\frac{\partial}{\partial x}[p(x,t) + p_T(x,t)]. \tag{2.43}$$

The linear current density due to drift and diffusion is

$$J(x,t) = e\mu p(x,t)E(x,t) - eD\frac{\partial p(x,t)}{\partial x}, \tag{2.44}$$

where μ is the mobile hole mobility and D is the mobile hole diffusivity, which is related to the mobility by the Einstein relationship. As holes are injected from the electrode into the pentacene, the sheet concentration of mobile holes varies with time according to the continuity equation,[133]

$$\frac{\partial p}{\partial t} = -\frac{1}{e}\frac{\partial}{\partial x}J + \left.\frac{\partial p}{\partial t}\right|_{traps}. \tag{2.45}$$

After combining Eqs. (2.41)–(2.45), the sheet concentration of mobile holes at position x and time t satisfies

$$\frac{\partial p}{\partial t} = \frac{e\mu}{C'}\left[\frac{\partial}{\partial x}\left(p\frac{\partial p}{\partial x}\right) + \frac{\partial}{\partial x}\left(p\frac{\partial p_T}{\partial x}\right)\right] + D\frac{\partial^2 p}{\partial x^2} + \left.\frac{\partial p}{\partial t}\right|_{traps}. \tag{2.46}$$

With the same definitions in Eqs. (2.21) and (2.22), the sheet concentration of trapped holes is determined by

$$\frac{\partial p_T}{\partial t} = \tilde{c}p(N_T - p_T) - \tilde{e}p_T = -\left.\frac{\partial p}{\partial t}\right|_{traps} . \tag{2.47}$$

To solve the coupled non-linear partial differential Eqs. (2.46) and (2.47), appropriate initial and boundary conditions are needed. For an initial voltage sweep that crosses the threshold voltage for carrier injection V_T at $t = 0$ ($V_T = 0$ for a pristine device), no holes exist in the pentacene channel,

$$p(x, t = 0) = p_T(x, t = 0) = 0 . \tag{2.48}$$

Since the current vanishes at the far end of the device, the boundary condition at $x = L$ is

$$(\partial p / \partial t)\big|_L = (\partial p_T / \partial t)\big|_L = 0 . \tag{2.49}$$

When bias is applied and holes are injected into the channel and the gate voltage varies linearly with time, the following conditions at the contact hold:

$$e[p(x = 0, t) + p_T(x = 0, t)] = C'V(x = 0, t) , \tag{2.50}$$

$$V(x = 0, t) = -V_G(t) = -[V_G(t = 0) - |r_V| \cdot t] , \tag{2.51}$$

for $t > 0$. The current, $I(t)$, going into the contact at $x = 0$ may be calculated either by monitoring the rate of increase in the integrated mobile and trapped holes in the pentacene or by directly evaluating $J(x,t)$ from Eq. (2.44) at $x = 0$,

$$\begin{aligned} I(t) &= eW \frac{\partial}{\partial t} \int_0^L [p(x,t) + p_T(x,t)] dx \\ &= -\frac{We^2}{C'} \mu \cdot p(0,t) \left[\frac{\partial p(0,t)}{\partial x} + \frac{\partial p_T(0,t)}{\partial x} \right] - eWD \frac{\partial p(0,t)}{\partial x} . \end{aligned} \tag{2.52}$$

Figure 2.11 shows the calculated *I-V* characteristics using different hole mobilities of 0.1, 1, and 10 $cm^2V^{-1}s^{-1}$ in the case of vanishing trap concentration. Carrier mobility can greatly affect the transient regions in both carrier injection and extraction. In carrier injection, larger hole mobility leads to smaller and narrower peaks; in the carrier extraction, larger hole mobility results in a shorter transient region. It is notable that a good linear region exists in the forward sweep between the onset and the maximum of the displacement current peak. The slope of the linear region is related to the hole mobility, sweep rate, oxide capacitance, channel width, and is independent of channel length, as can be understood already on the basis of the geometric model discussed in section 2.3.1. However, one has to keep in mind that Eqs. (2.13)–(2.15) is meaningful only before holes are distributed uniformly over the channel. Hence, the gate voltage has to be smaller than $|r_V|(2L/\sqrt{\mu r_V})$, but it should be larger than *kT/e* so that diffusion is negligible. For the large and relatively low mobility devices considered in this thesis, that is always the case.

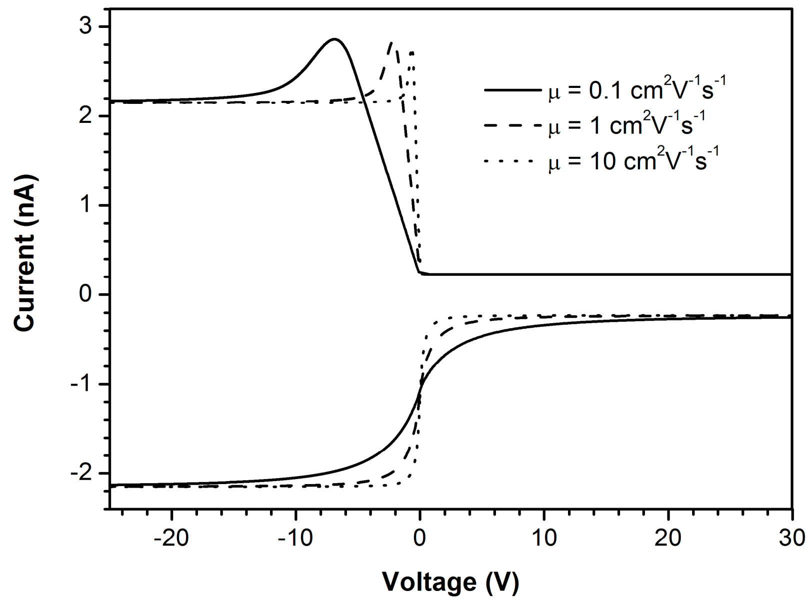

Figure 2.11: Calculated *I-V* characteristics using different hole mobilities in the full numerical model for the trap free case.

2.4 Effects of traps

The effective mobility that controls the transient displacement current is different from the steady state mobility measured by conventional dc OFET experiments. In that latter case, the mobility is measured when traps are partially filled and trapping/detrapping events balance. The effective mobility explored here is measured during the transient phase of carrier injection while traps are being filled. When traps are included in the model, the slope of the *I-V* curves in the transient region decreases and a meaningful effective mobility, which is smaller than the mobile carrier mobility, can be calculated from Eq. (2.14). The decreased effective mobility shows how traps influence the carrier transport. With the addition of traps to the numerical model, three parameters need to be considered: the total available trap density (N_T), the capture coefficient ($\tilde{c}$), and emission coefficient ($\tilde{e}$). The product of N_T and $\tilde{c}$ determines how fast mobile holes can be trapped and the emission coefficient determines how fast trapped holes are released. Depending on the average trapping time relative to $\Delta t \approx 1$ s, i.e. the time scale of the transient process ($\Delta t = 2L/\sqrt{\mu|r_V|}$), traps have different effects on μ_{eff}.

In order to explore how traps influence the effective mobility, we derive results for the effective mobility as a function of trapping parameters. It is useful to define $\tilde{e}' = \tilde{e}/N_0$, where N_0 is the effective density states for "mobile" holes. Detailed balance requires that in equilibrium the capture and emission rates are related by

$$\tilde{c}p_0(N_T - p_{T0}) = \tilde{e}'\, p_{T0}(N_o - p_0)\,, \qquad (2.53)$$

where the subscripts 0 indicate equilibrium concentrations. We assume that the mobile holes populate a narrow band at energy E_v, and that trapped holes populate states at energy levels E_T; ($E_T > E_v$),

$$p = \frac{N_o}{1 + g^{-1} \exp\left(\frac{E_F - E_V}{kT} \right)}, \tag{2.54}$$

$$p_T = \frac{N_T}{1 + g_T^{-1} \exp\left(\frac{E_F - E_T}{kT} \right)}, \tag{2.55}$$

where g and g_T are the degeneracy factors and E_F is the Fermi energy. Combining Eqs. (2.53)–(2.55) and using Eq. (2.22) yields

$$\frac{\tilde{c}}{\tilde{e}'} = \frac{\tilde{c} N_o}{\tilde{e}} = \frac{g_T}{g} \exp\left(\frac{E_T - E_V}{kT} \right), \tag{2.56}$$

$$\tau_{cap} = 1/(\tilde{c} N_T), \tag{2.57}$$

$$\tau_{emi} = \frac{1}{\tilde{e}} = \tau_{cap} \frac{N_T}{N_o} \frac{g_T}{g} \exp\left(\frac{E_T - E_V}{kT} \right). \tag{2.58}$$

Evidently, even if τ_{cap} is not temperature dependent, τ_{emi} increases exponentially as the temperature decreases. The average field effect mobility is smaller than the mobile carrier mobility because only a fraction of all carriers are mobile,

$$\mu_{ave} = \mu \frac{\tau_{cap}}{\tau_{cap} + \tau_{emi}} = \mu \frac{1}{1 + \frac{N_T}{N_o} \frac{g_T}{g} \exp\left(\frac{E_V - E_T}{kT} \right)}. \tag{2.59}$$

Equation (2.59) shows how the average mobility is affected by the trapping/detrapping mechanism in equilibrium. The relationship also clearly shows that the average mobility has a temperature dependence that is characterized by the activation energy associated with thermal emission of charge carriers from traps, in addition to the intrinsic temperature dependence of μ. Indeed, activated transport is generally observed in organic semiconductor devices such as the field effect transistor structures considered

here. Activation energies extracted from the experiments are in the range of 35 meV < E_A < 100 meV,[134] with typical values for pentacene OFETs fabricated by the same process as used for the structures of interest here being ~55 meV.[128]

The extent to which μ_{ave} may be equated with μ_{eff} depends of course on the relative time scales of the trapping/detrapping processes and the current transient. As the detrapping process is rather sensitive to temperature, it is expected that different regimes may be relevant for the same device and sweep rate at different temperatures. Three cases are described in the following.

2.4.1 Slow traps

For the case of slow traps: τ_{cap} or $\tau_{\text{emi}} >> \Delta t$, $\mu_{eff} \approx \mu$. When the average trapping time is much larger than Δt, almost no mobile holes are captured and the mobility is unaffected by the traps. Therefore, the mobility is time independent, and it is likely to be only weakly temperature dependent. Figure 2.12 shows calculated *I-V* curves for slow traps. The capture time is held fixed at $\tau_{\text{cap}} = 5$ s, while τ_{emi} assumes values of 5, 10, 20, and 40 s. The capture and emission times are much larger than Δt. Hence, the *I-V* characteristics during the carrier injection sweep are the same for all cases.

While the gate voltage decreases from 0 to −30V (in about 5 s) some mobile holes are captured by traps. Additional capture occurs during the charge extracting sweep. Therefore, trapped holes result in a threshold voltage shift that is detected in the charge extracting sweep. With decreasing emission rate more holes remain in traps, increasing the threshold shift and suppressing the current associated with the emission of charge carriers from traps, which is most clearly observed during the extracting sweep once the voltage is again positive.

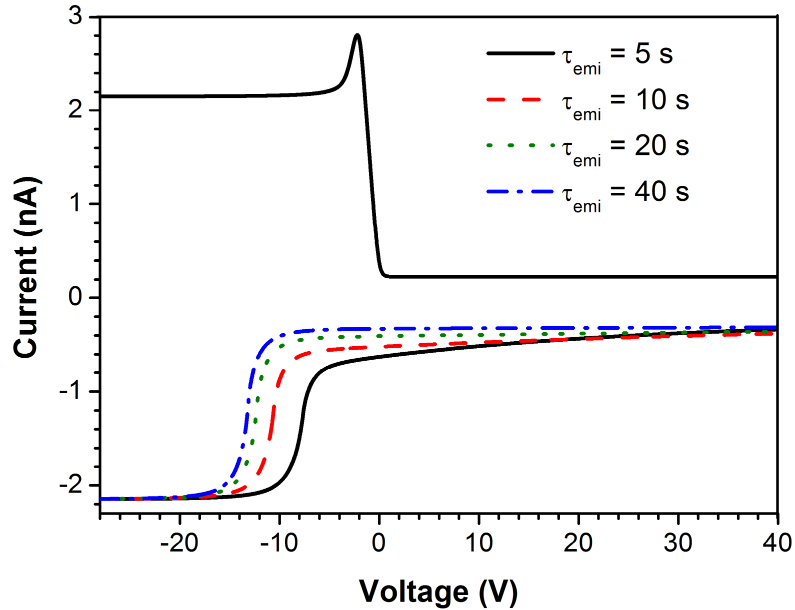

Figure 2.12: Calculated *I-V* characteristics for different trap time constants that are much larger than the time scale of the transient. τ_{cap} = 5 s, and τ_{emi} = 5, 10, 20, and 40 s.

In the simple scenario of slow traps, the trapped carrier concentration is much less than that of the mobile carriers and one may explain the effects of the trapping parameters concisely. This situation is also true for the experimental results shown in Table 2.1: the trapped carriers are usually less than 10% of the total charge carriers injected into the channel. Figure 2.13 shows the calculated results with different τ_{cap}. The emission time constant is fixed at 10^3 s in all calculations. Evidently, τ_{cap} has little effect on the forward sweep. However, a smaller τ_{cap} shifts the transient region in the reverse sweep to more negative voltages, indicating more trapping in the channel.

Figure 2.14 shows the calculated *I-V* characteristics with different emission time constants. τ_{cap} is fixed at 10 s. Similarly, the shape of the transient region in the forward sweep is not strongly affected by τ_{emi}. For a large emission time constant such as τ_{emi} = 10^3 s, most of the trapped carriers cannot be emitted during the reverse sweep, resulting in a large negative shift in the transient region of the reverse sweep. On the contrary, for

a small emission time constant such as $\tau_{emi} = 10^{-2}$ s, most of the trapped carriers can be emitted. Lastly, if the emission time constant is comparable to the time scale of reverse sweep as is the case for $\tau_{emi} = 2$ s, the detrapped carriers can contribute to the displacement current in the reverse sweep. Therefore, the displacement current near the end of the reverse sweep increases in magnitude over the displacement current associated with the gold contact.

Figure 2.15 shows the calculated *I-V* characteristics with three consecutive cyclic sweeps. The emission and capture time constants are of about the same order as the time scales of injection and extraction processes (~7 s). The threshold shift of carrier injection in the second sweep is attributed to the fact that there are trapped carriers remaining in the channel after the first sweep. However, the threshold shift of carrier injection in the third sweep is much smaller than that of the second sweep because fewer carriers are trapped in the second sweep than in the first sweep. Figure 2.15 shows good agreement with the experimental data of Fig. 2.4.

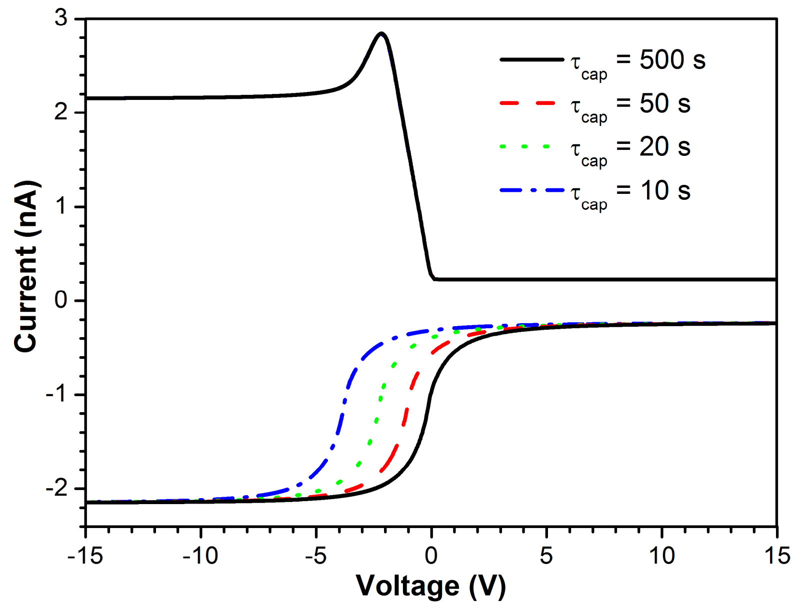

Figure 2.13: Calculated *I-V* characteristics with different τ_{cap}. The emission time constant is fixed at 10^3 s for all the calculations. More negative shift is observed in the reverse sweeps for smaller τ_{cap}.

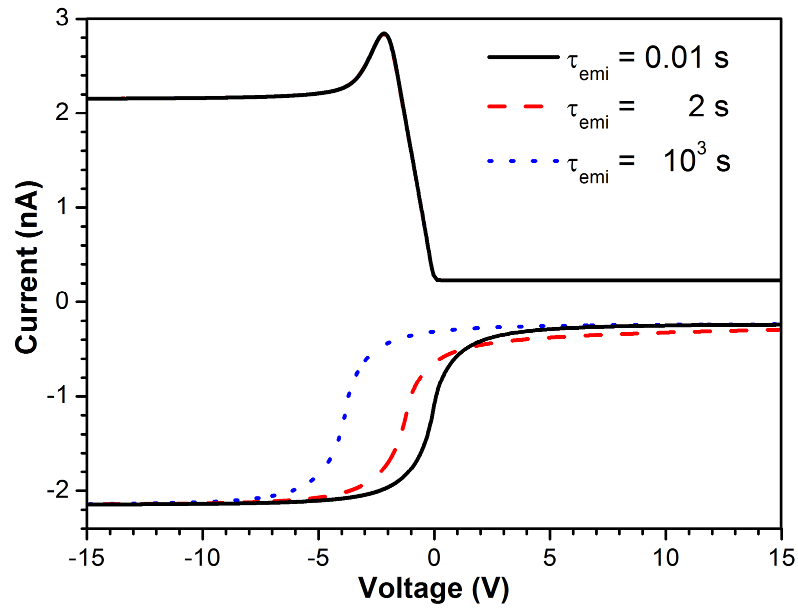

Figure 2.14: Calculated *I-V* characteristics with different τ_{emi} , with τ_{cap} = 10 s in all calculations.

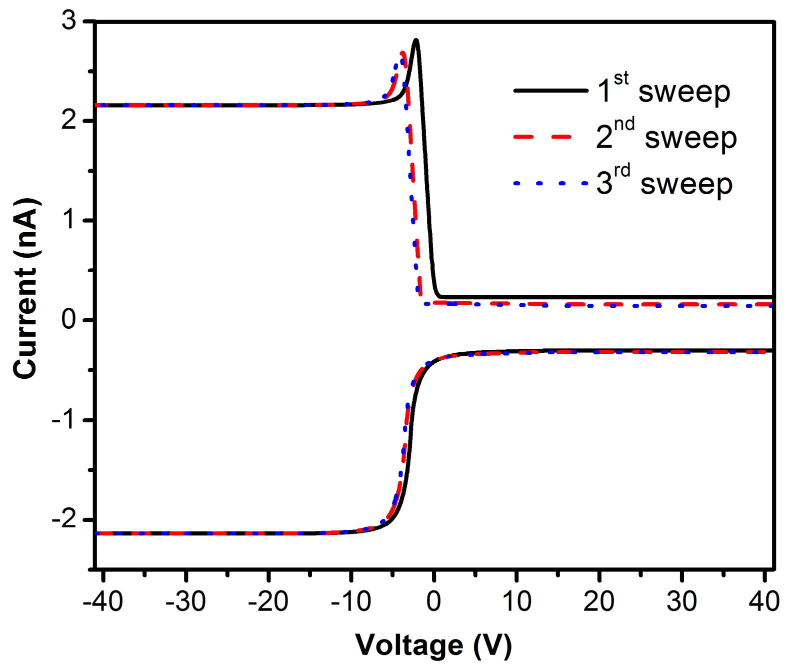

Figure 2.15: Calculated *I-V* characteristics for three consecutive cyclic sweeps. τ_{cap} = τ_{emi} = 10 s.

2.4.2 Fast traps

For the case of fast traps: τ_{cap} and $\tau_{emi} << \Delta t$, $\mu_{eff} = \mu_{ave}$. When the average trapping time is much smaller than Δt, the capture and emission rates are so fast that the fraction of the mobile carriers is approximately constant. Under this condition, the effective mobility is well approximated by the average mobility; it is temperature dependent but time independent. In Figs. 2.16 and 2.17, we plot *I-V* and *I-t* characteristics for several fast trap cases. Here we choose $\tau_{\mathrm{cap}} = 0.01$ s, and τ_{emi} takes the values of 0.01, 0.02, 0.04, and 0.08 s. τ_{emi} and τ_{cap} are small compared with $\Delta t \approx 1$ s, even for the longest emission time considered. As shown in the inset of Figs. 2.16 and 2.17, the effective mobility versus time for the different cases is essentially time independent. The small mobility increase at the beginning is attributed to the diffusion current, which is neglected in Eq. (2.15). This result also agrees with Fig. 2.7 because the ratio of mobile and trapped hole concentrations does not change with time.

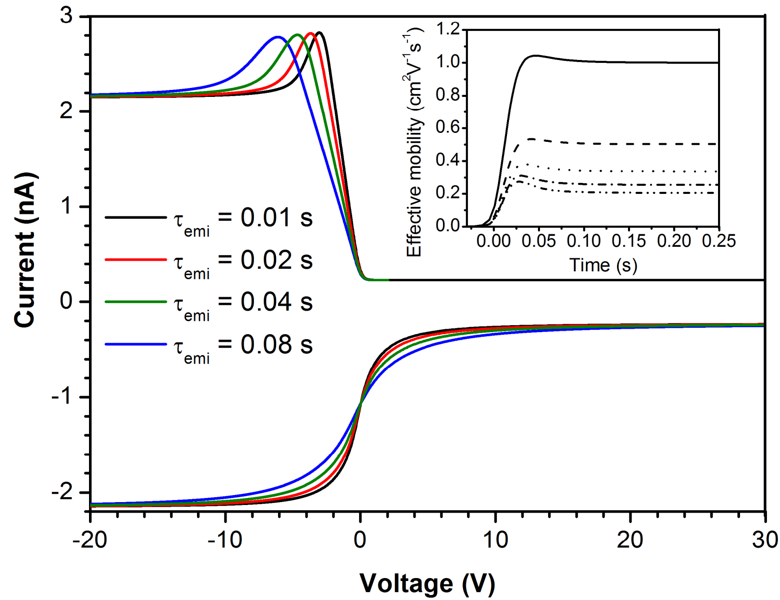

Figure 2.16: Calculated *I-V* characteristics for different trap time constants that are much smaller than the time scale of the transient. Inset: μ_{eff} vs time. The Dash-dot-dot curve is for the non-trapping case. Solid, dashed, dotted, and dash-dot lines are for fast trapping cases, τ_{emi} = 0.01, 0.02, 0.04, and 0.08 s, respectively. τ_{cap} = 0.01 s is unchanged for all calculations.

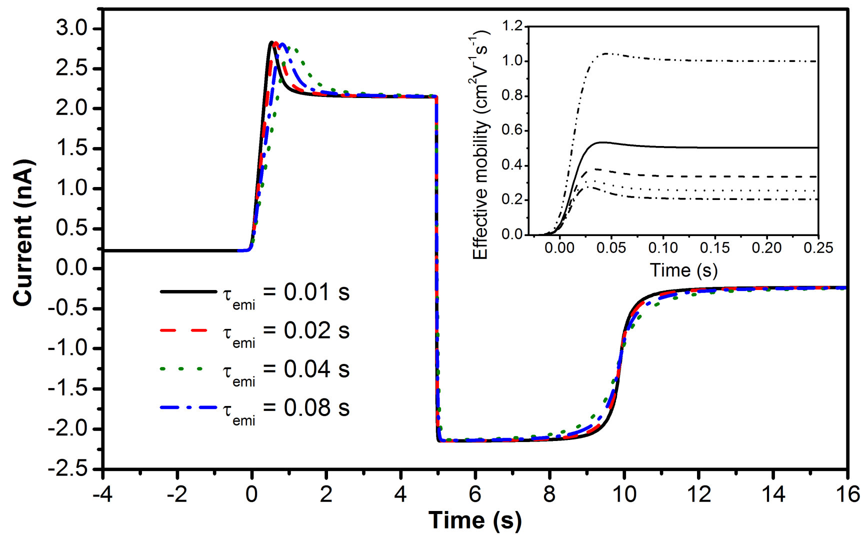

Figure 2.17: Calculated *I-t* characteristics for different trap time constants that are much smaller than the time scale of the transient. Inset: μ_{eff} vs time. Trapping parameters and notations are the same as in Fig. 2.16.

2.4.3 Intermediate traps

For the case of intermediate traps, $(\tau_{cap} + \tau_{emi}) \approx \Delta t$, $\mu_{eff} = \mu_{eff}(t)$. When the average trapping time is comparable to the time scale of the current transient, the effective mobility is time dependent as the fraction of trapped charge carriers changes. In Figs. 2.18 and 2.19, calculated *I-V* and *I-t* characteristics for different emission time are plotted, respectively. The capture time is chosen to be the same as in the case of fast traps ($\tau_{cap} = 0.01$ s), but the emission time constant is taken to be longer, $\tau_{\mathrm{emi}} = 0.1$, 0.2, 0.4, and 0.8 s. This makes the emission time comparable to Δt. The effective mobility versus time is plotted in the inset of Figs. 2.18 and 2.19. The effective mobility is larger at the beginning of charge injection and decreases subsequently. Near steady state conditions are approached toward the end of the time range plotted in the inset. Once the trapping/detrapping events balance, $\mu_{eff} \approx \mu_{ave}$. When the effective mobility changes with time, we may use Eqs. (2.23) and (2.24) to approximate μ_{eff}:

$$\mu_{eff} \approx \mu \frac{\overline{p}(t)}{\overline{p}(t) + \overline{p}_T(t)} = \mu \frac{1}{(\tilde{e} + \tilde{c}N_T)\cdot t}\left[\tilde{e}\,t - \frac{\tilde{c}N_T}{\tilde{e} + \tilde{c}N_T}(e^{-(\tilde{e}+\tilde{c}N_T)t} - 1)\right]. \tag{2.60}$$

Equation (2.60) shows good agreement with the inset of Figs. 2.18 and 2.19.

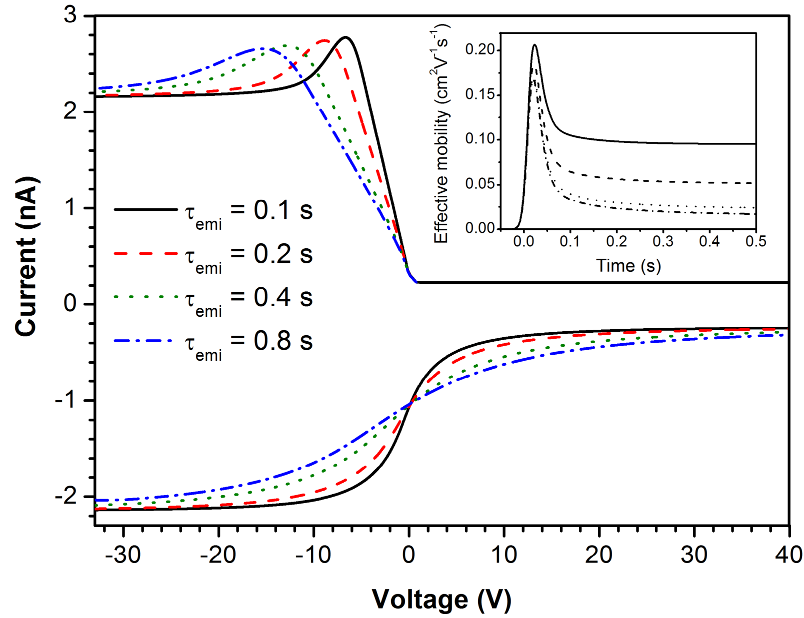

Figure 2.18: Calculated *I-V* characteristics for trap time constants with τ_{emi} comparable to the time scale of the transient. Inset: μ_{eff} vs time for the cases discussed. Solid, dashed, dotted, and dash-dot lines are for τ_{emi} = 0.1, 0.2, 0.4, and 0.8 s, respectively. τ_{cap} = 0.01 s is fixed for all the calculations.

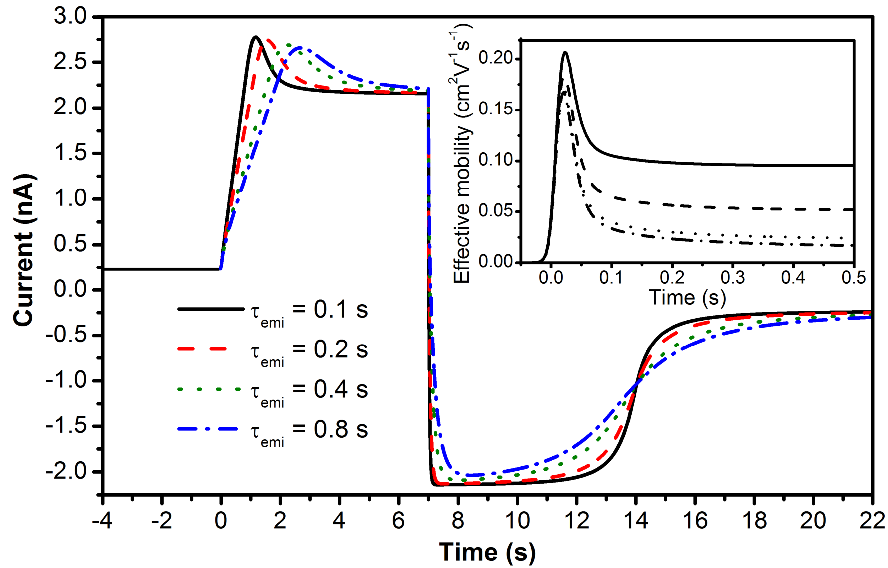

Figure 2.19: Calculated *I-t* characteristics for trap time constants with τ_{emi} comparable to the time scale of the transient. Inset: μ_{eff} vs time for the cases discussed. Trapping parameters and notations are the same as in Fig. 2.18.

2.4.4 Non-uniform distribution of trap states: metal/semiconductor interface

In this section, we study effects of non-uniform distribution of traps (in the channel) on displacement current characteristics, which trap states near metal/organic-semiconductor interfaces may in some cases impact carrier injection and extraction significantly.[135] Gold is the most widely used contact material with pentacene in OFETs. However, Au often penetrates into the semiconductor layer in top-contact devices and results in detrimental effects on device performance.[136,137] In the experiments different thicknesses (30 and 100 nm) of pentacene films are deposited individually and the Au contacts of all the devices are deposited in one single process. Figures 2.20 shows the measured displacement current of devices fabricated with Au contacts deposited on 30 nm (Au/30Pen) and 100 nm (Au/100Pen) thickness pentacene. Evidently, the displacement current depends on the thickness of the pentacene films. The threshold shift of Au/30Pen indicates that almost all injected holes are trapped at the very beginning of carrier injection. Equations (2.2)–(2.4) are used and the numbers of carriers injected into the pentacene channel are similar for both Au/30Pen and Au/100Pen, while fewer carriers are extracted from Au/30Pen, as indicated from the current shift in carrier extraction process. Figure 2.21(a) shows the average trapped carrier density, and there are about three times more trapped carriers in Au/30Pen than that in Au/100Pen.

Previous reports have shown that metal/OSC interfaces are complicated due to the variations of metal-OSC energy band diagrams,[138] interfacial dipoles,[139,140] and microstructures of the organic semiconductor films.[141-143] Studies have also demonstrated that Au atoms can penetrate organic semiconductor films when deposited from the vapor phase,[136,137] and generate deep trap states near the metal/pentacene interface.[144,145] In addition, deep trap states may extend into the channel due to the lateral diffusion of the penetrating Au atoms.[146,147] As shown in Figs. 2.21(b) and 2.21(c), the dependence of the current characteristics on the thickness of the pentacene films may be attributed to the non-uniform distribution of traps in the case of Au/30Pen. In other words, deep trap states concentrated near the metal/OSC interface lead to the dissimilarities between the current characteristics of Au/30Pen and Au/100Pen.

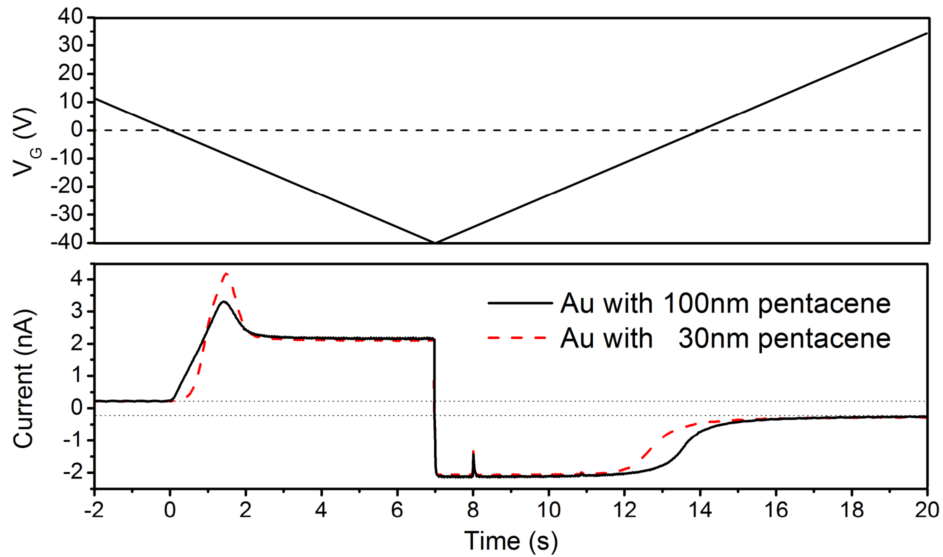

Figure 2.20 : (a) Applied gate voltage versus time. (b) Measure *I* versus *t* from devices fabricated with Au contacts with different thickness of pentacene films.

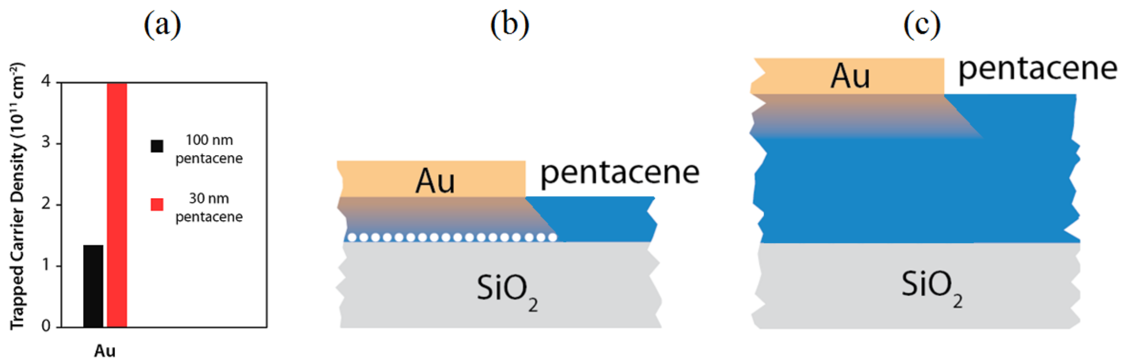

Figure 2.21 (Courtesy of Yan Liang): (a) Average trapped carrier density for Au/30Pen and Au/100Pen. (b) and (c) Schematic diagrams for the penetration of Au atoms into 30 nm and 100 nm thick pentacene, respectively. The white dots represent deep traps.

Numerical device model is used to support the premise that deep trap states near the contact edge may cause mobile carriers to be trapped along the length of the channel, and affect carrier injection and extraction. In the model, traps are limited to a very narrow region near the contact edge and no traps exist elsewhere in the long channel. The assumed trap distribution, $N_T(x)$, is a half Gaussian function centered at the contact

edge. The integrated density of traps per unit width, *W*, of the channel ($\int_0^L N_T(x)dx$) is 9.7×10^8 cm^{-1}. Populating the traps by injecting holes when the gate voltage swings to negative values causes them to be charged positively, giving rise to a potential barrier near the contact. This barrier limits the extraction of mobile holes during the subsequent sweep of the gate voltage toward positive values.

The dashed line in Fig. 2.22 shows the calculated result for the device with deep traps near the contact edge, while the solid line is for an ideal device with no traps. Similar to the experimental data shown in Fig. 2.20, a higher displacement current peak is observed in the forward sweep for the device with deep traps near the contact edge. In the reverse sweep, fewer carriers are extracted from this device as indicated by the shift of the threshold to a more negative value visible in the dashed curve. The integrated density of trapped carriers calculated for the dashed displacement current curve is 3.5×10^{11} cm^{-1}, which is much larger than the integrated density of traps (9.7×10^8 cm^{-1}). This result confirms that mobile carriers can be trapped along the length of the channel by the presence of a potential barrier near the contact.

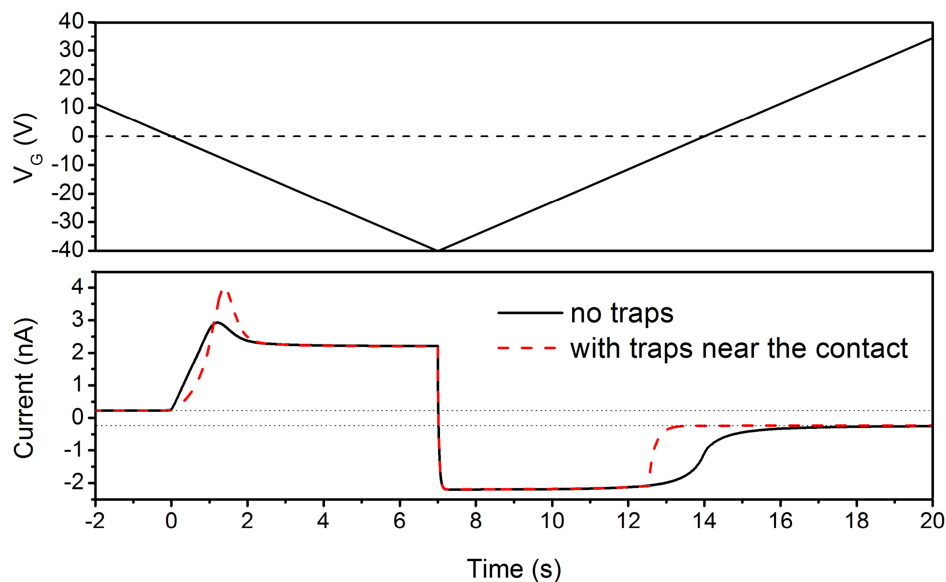

Figure 2.22: (a) Applied gate voltage versus time. (b) Calculated results for the *I-t* characteristic. The dashed curve represents the case in which deep trap states are limited to a narrow region near the contact edge. The solid curve represents the case of an ideal device with no traps.

2.5 Conclusion

We have modeled transient charge carrier transport in OFET structures with one of the channel contacts removed. Numerical and approximate analytical models are used to study the formation and depletion of the conducting channels. The asymmetric current characteristics between injection and extraction processes observed in the experiments are explained qualitatively on the basis of three analytical models. In the geometric model, the initial parabolic dependence of the injected carrier density on time associated with the distribution of injected carriers over the channel results in a current peak of the injection process. The spatially averaged carrier density model, however, neglects the transient spatial redistribution of the charge carriers by averaging the carrier density over the channel length. It explains the threshold shift in the extraction process, but no current peak is observed in the injecting sweep, which verifies that non-linearity is linked to the carrier spatial redistribution. This non-linear phenomenon may also be modeled with a resistor-capacitor equivalent circuit in which the resistance changes with the carrier density. The dependence of the resistance on the injected carriers (charging the capacitor) leads to a current peak during the injection (charging) process.

With the numerical device model, the wide range of time constants associated with carrier capture into traps and emission from traps allows for several distinct cases to be examined. The geometric model of the injection process is used as a basis for the definition of an effective mobility that is quite different from the free carrier mobility because of charge carrier trapping. Trapping processes that are slow on the relevant transient time scale have negligible impact on the effective mobility, but they may manifest themselves in threshold shifts that are observed during charge carrier extraction. Very fast traps (on the time scale of the transient region) give rise to an average mobility that may be obtained from steady state measurements. Most interesting is the case of traps with time constants that are comparable to the transient time scale. Under these conditions the effective mobility characterizing the injection transient is itself time dependent.

3 Charge carrier extraction transient in OFET channels

3.1 Introduction

Here the equivalent circuit model described briefly in section 2.3.3 is applied to charge carrier extraction from the channel. The initially accumulated channel is depleted by a sudden change of the gate voltage. During the depletion of the conducting channel, carrier extraction is increasingly impeded by the increasing resistance of the channel. The measured discharge current transient decreases either as a power law or exponentially if the final state of the channel is completely or partially depleted, respectively. Analytical and numerical results are discussed and compared with the experimental data

3.2 Device structure and experiments

The schematic device structure is shown in Fig. 3.1(a). A heavily doped p-type Si wafer with a 300 nm thick thermal oxide layer was used as the substrate, and a 30 nm thick square-shaped pentacene film was thermally evaporated on the top of the SiO_2. The length (L) and width (W) of the pentacene film were 3 mm. Electrical characterization was carried out by measuring the displacement current running through the grounded top electrode while biasing the bottom gate. Copper was employed as the channel contact because of its relatively low contact resistance to pentacene.[135-150] (The threshold voltage (V_T) determined from the displacement current measurements was about 5.5 V).

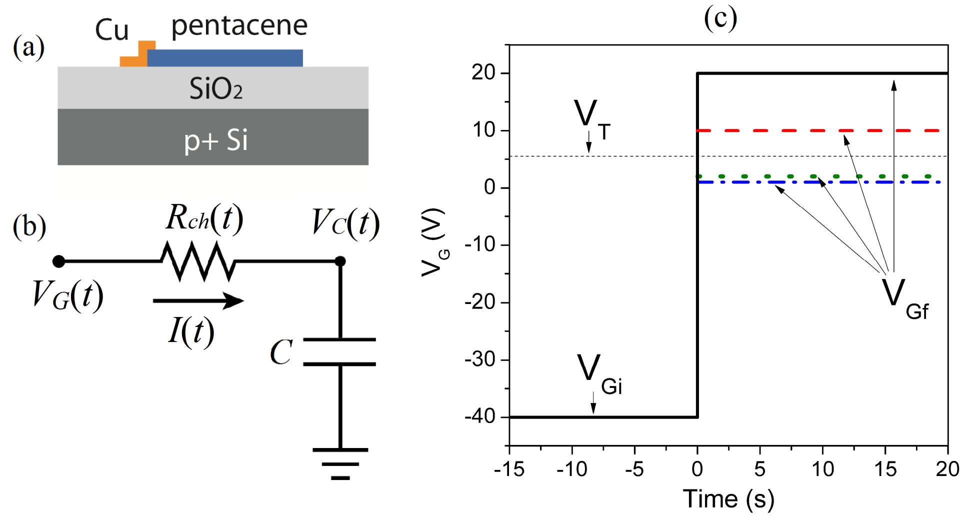

Figure 3.1: (a) Schematic device structure (300 nm thick thermal oxide layer). The length and width of the 30 nm thick pentacene film were 3 mm. (b) The model RC circuit with time-dependent channel resistance, $R_{ch}(t)$, and constant capacitance (C). (c) Gate voltage profile. The solid and dashed lines refer to a completely depleted channel in the final state, while dotted and dash-dotted lines correspond to partially depleted channels in the final states.

A constant initial voltage bias (V_{Gi}) of –40 V was applied for 15 s to inject holes and form a (steady state) conducting channel. Then the gate voltage abruptly increased to a new constant value (V_{Gf}), as shown in Fig. 3.1(c). The discharge current was measured and it was found that the current characteristics depend on V_{Gf} in a rather striking way. Using V_T as the reference voltage in the following discussion it is helpful to introduce $V_{GT,f} = V_{Gf} - V_T$ and $V_{GT,i} = V_{Gi} - V_T$. Figure 3.2 shows the discharge current measured for different $V_{GT,f}$ in semi-log and log-log (inset) scales. For $V_{GT,f} = -4.5$ or –3.5 V, i.e., $V_{Gf} = 1$ or 2 V, the transient current strongly depends on $V_{GT,f}$ and decreases approximately linearly on a semi-log scale from 0.1 to 0.01 nA. For $V_{GT,f} = 4.5$ or 14.5 V, i.e., $V_{GT,f} = 10$ or 20 V, the current is independent of $V_{GT,f}$ and decreases approximately linearly on a log-log scale. Evidently, for the case of $V_{GT,f} < 0$, the pentacene channel is depleted only partially in the final state and the transient current in the long time limit follows an approximately exponential decrease with time. When $V_{GT,f} \geq 0$, the channel is completely depleted in the final state and the discharge current in the long time limit decreases with time as a power law.

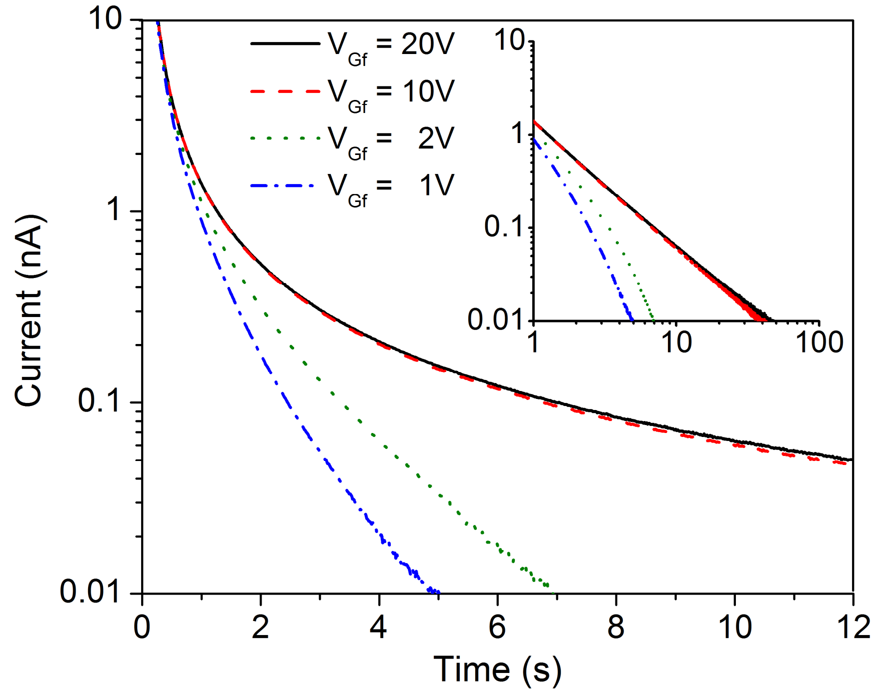

Figure 3.2 (Courtesy of Yan Liang): Measured discharge current versus time on semi-log and log-log (inset) scales.

3.3 Time dependent discharge current

3.3.1 Resistor-capacitor circuit model

To understand time-dependent discharge current, we develop the model describing transient carrier extraction with a non-linear resistor-capacitor circuit (Fig. 3.1(b)) in which the resistance changes with the carrier density. Thus, the resistance increases with decreasing potential difference across the capacitor. The channel resistance and the discharge current (for $t > 0$) are given by:

$$I(t) = \frac{V_G(t) - V_C(t)}{R_{ch}(t)} = C\frac{dV_C(t)}{dt}, \tag{3.1}$$

$$R_{ch}(t) = \frac{L}{W\sigma(t)} = \frac{L}{We\mu \cdot p(t)}, \tag{3.2}$$

where e is the elemental charge, μ is the hole mobility, C is the channel capacitance, and the channel resistance, $R_{ch}(t)$, is assumed to be inversely proportional to the density of mobile holes, $p(t)$. In order to solve Eqs. (3.1) and (3.2), one has to consider the effects of traps and relate $p(t)$ to the total hole density, $P(t) = p(t) + p_t(t)$, where $p_t(t)$ is the density of trapped holes. $P(t)$ is linearly proportional to the potential across the capacitance,

$$eP(t)WL = \begin{cases} -CV_C(t), & V_C(t) < 0 \\ 0, & V_C(t) \geq 0 \end{cases}, \tag{3.3}$$

where the threshold voltage is set to zero. Assuming the time scale of the traps is short compared to that of the transient experiments and capture and emission rates balance,

$$\tilde{c}p(P_T - p_t) = \tilde{e}p_t, \tag{3.4}$$

$$\frac{\tilde{e}}{\tilde{c}P_T} = \frac{\tau_{cap}}{\tau_{emi}}. \tag{3.5}$$

where P_T is the density of traps, and τ_{cap} and τ_{emi} are capture and emission time constants. Combining Eqs. (3.4) and (3.5), a parabolic relationship between $p(t)$ and $P(t)$ is obtained

$$p = -[(1+\frac{\tau_{cap}}{\tau_{emi}})P_T - P]/2 + \sqrt{[(1+\frac{\tau_{cap}}{\tau_{emi}})P_T - P]^2/4 + P_T P\frac{\tau_{cap}}{\tau_{emi}}}. \tag{3.6}$$

3.3.2 Discharge current without traps

First, we explore the transient hole extraction without traps, i.e. $P_T = 0$, $p(t) = P(t)$ and combining Eqs. (3.1), (3.2), and (3.3) we obtain the following non-linear ordinary differential equation for $V_C(t)$:

$$\frac{dV_C}{dt} = \frac{\mu}{L^2}[(V_C)^2 - V_G V_C]\,. \tag{3.7}$$

Under conditions,

$$V_G(t \le 0) = V_{GT.i}\,, \tag{3.8}$$

$$V_G(t > 0) = V_{GT.f}\,, \tag{3.9}$$

analytical solutions of $V_C(t)$ for two scenarios are formed,

$$V_C(t) = \begin{cases} 1/[(1/V_{GT,f} - 1/V_{GT,i})\exp(\mu V_{GT,f}t/L^2) - 1/V_{GT,f}] & V_{GT,f} < 0 \\ -1/(\mu t/L^2 + 1/V_{GT,i}) & V_{GT,f} \ge 0 \end{cases}. \tag{3.10}$$

The current consequently becomes:

$$I(t) = \begin{cases} \dfrac{\mu C V_{GT,f}}{L^2}\dfrac{(1/V_{GT,f} - 1/V_{GT,i})\exp(\mu V_{GT,f}t/L^2)}{[(1/V_{GT,f} - 1/V_{GT,i})\exp(\mu V_{GT,f}t/L^2) - 1/V_{GT,f}]^2} & V_{GT,f} < 0 \\ (CL^2/\mu)/[t + (L^2/\mu V_{GT,i})]^2 & V_{GT,f} \ge 0 \end{cases} \tag{3.11}$$

Detailed derivations of Eqs. (3.10) and (3.11) are presented in Appendix C.

In the long time limit, the current decreases exponentially for the partially-depleted channel ($V_{GT,f} < 0$), while a power law dependence for the completely-depleted channel ($V_{GT,f} \ge 0$) implies a slower hole extraction rate due to the larger channel

resistance of the latter. Figure 3.3 shows the analytical results for partially- and completely-depleted channels. Exponential behavior for the non-trapping partially-depleted channel is shown as the dotted and dash-dotted lines, with the extraction rate (exponential term) depending on $V_{GT,f}$. On the other hand, the solid curve shows the discharge current in the completely-depleted channel case, and $V_{GT,f}$ has no effect on the current, which decreases with time as a power law.

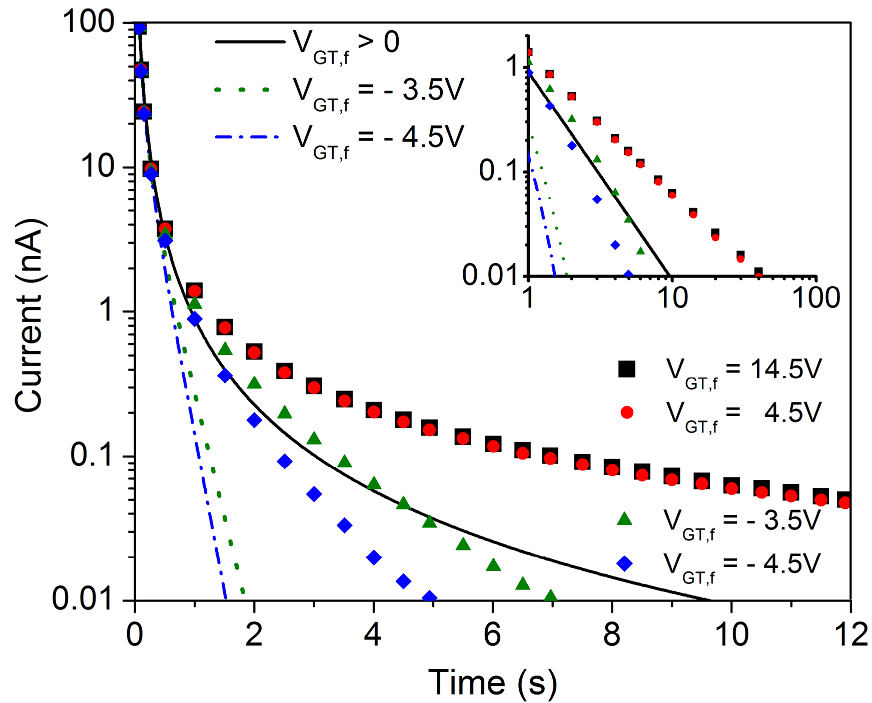

Figure 3.3: Discharge current versus time on semi-log and log-log (inset) scales. Experimental data are shown in symbols, and lines are analytical results from Eq. (3.11) with $V_{GT.i}$ = –45.5 V and μ = 0.1 $cm^2V^{-1}s^{-1}$.

The two distinct characteristics can be explained qualitatively by considering the simple discharge of a capacitor. If the resistance is constant the current decreases exponentially. This is relevant for the partially-depleted channel where $R_{ch}(t)$ increases only at the very beginning and becomes a finite constant thereafter. However, for the

completely-depleted channel $R_{ch}(t)$ approaches infinity when the hole concentration in the channel approaches zero. The extraction rate becomes ever slower, and a power law decrease of the current is obtained. Furthermore, the long-time limit transient current measured for $V_{GT,f} \geq 0$ in the temperature range 300 K > T > 120 K increases with decreasing temperature.[128] This result also agrees with the model, as the decreasing charge carrier mobility leads to an increasing current in the long time limit, as shown in Eq. (3.11).

3.3.3 Effects of traps

While the analytical results of the preceding section 3.3.2 are qualitatively consistent with the experimental data, as Fig. 3.3 shows, the calculated currents decrease more rapidly with time than those measured. Moreover, in the case of the completely depleted channel, the inset shows that the magnitude of the exponent derived from the data is about 1.3, not 2 as predicted by Eq. (3.11).

We next consider the effect of traps on transient carrier extraction as in Eqs. (3.4)–(3.6). The parabolic relationship between the density of mobile carriers and the density of total carriers is plotted in Fig. 3.4. Without traps, $p(t)$ is linearly proportional to $P(t)$. With traps, as the trapping ratio τ_{emi}/τ_{cap} increases, the density of trapped carriers increases, and the density of mobile carriers decreases. At the beginning of the discharging process, $p(t)$ decreases linearly with $P(t)$ and the extraction rate stays the same as that of the non-trapping case. When $P(t)$ is of the same order as P_T, the parabolic relation starts to play an important role, i.e., trapped carriers increase channel resistance dramatically and thus, the extraction rate decreases. In other words, traps in this model have no effect on the carrier extraction rate when $p(t) >> P_T$, but the rate is significantly reduced when $P(t)$ is comparable to P_T.

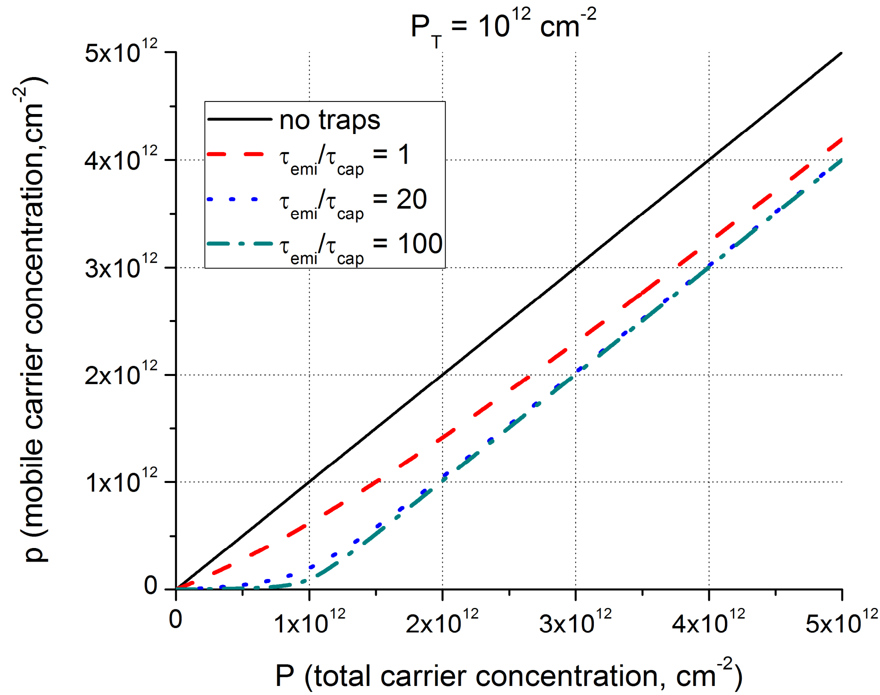

Figure 3.4: The density of mobile carriers versus the density of total carriers with different trapping ratios τ_{emi}/τ_{cap}.

We solve Eqs. (3.1)–(3.3) and (3.6) numerically. In Fig. 3.5, the calculated results obtained for $P_T = 3\text{x}10^{11}\text{cm}^{-2}$ and $\tau_{emi}/\tau_{cap} = 20$ are plotted. Evidently, these model results are in good agreement with the experimental data for both the partially and completely depleted cases. It is perhaps surprising that a model based on a single fast trap level yields such satisfactory results. Clearly, the physical structure is expected to contain a range of different traps, with some that may have characteristic times that are comparable to, or longer than, the time scale explored. The experimental data are acquired starting ~0.06s after the applied voltage step, and for currents below 0.01nA they become rather noisy, so that the experimentally accessible time range extends at most over 2.5 orders of magnitude.

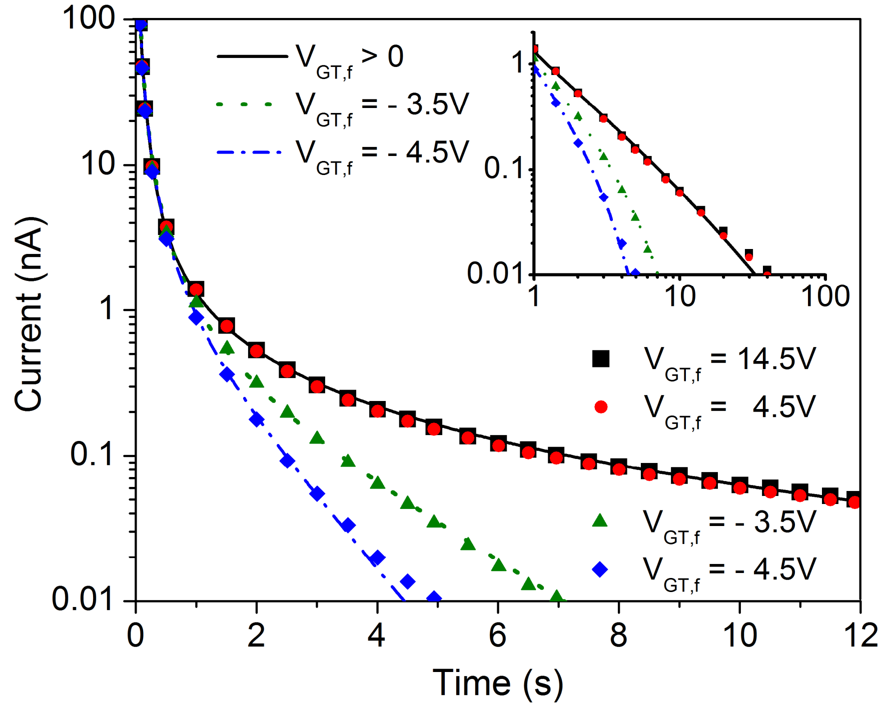

Figure 3.5: Semi-log and log-log (inset) plots comparing numerically-calculated currents (lines) with experimental data (symbols). $V_{GT,i} = -45.5$ V, $\mu = 0.1$ cm^{2}V^{-1}s^{-1}, with trap parameters $\tau_{emi}/\tau_{cap} = 20$, and $P_T = 3\times10^{11}$ cm^{-2}.

3.4 Conclusion

We model the transient carrier extraction characteristics in OFET structures and compare the results to experimental data. The conducting channel is depleted by an abrupt change of the gate voltage that leads to partially or completely depleted channels. Depending on the final state of the capacitor, either fully discharged or remaining partially charged, the displacement current in the long time limit shows power law or exponential dependence on time. We investigate the carrier extraction dynamics by using a resistor-capacitor equivalent circuit with a time-dependent resistance that describes the

increasing resistance during channel depletion. Without traps, analytical results show two distinct current characteristics depending on the final gate voltages below or above the threshold voltage. With traps, numerical results show that trapped carriers increase the channel resistance, giving rise to slower carrier extraction rates in both scenarios in good agreement with the experimental data. The effect of including fast traps is to change the apparent exponent in the resulting approximate power law for the case of full depletion. The exponent of the power law decreases in magnitude as the ratio of the emission to capture rates decreases. With a relatively large $|r_V|$, the different time dependence of the discharging currents is also verified by the complete device model which is less appropriate in this problem due to the discretization issue.

4 Geometric effects on interfacial recombination

4.1 Motivation

Photovoltaic technology is currently dominated by crystalline silicon for wafer-size solar cells. However, organic materials have been the subject of active research over the past twenty years and have received substantial interest in recent years from industry. Organic semiconductors, primarily conjugated polymers and crystals of relatively small hydrocarbon molecules, have become viable materials for optoelectronic and photovoltaic devices, in particular for low-cost and large-area applications. The molecular structure of organic semiconductors typically contains a backbone of sp^2-hybridized carbon atoms. The remaining p-orbitals of the carbon atoms form π-orbitals which are the highest occupied molecular orbital (HOMO) and lowest unoccupied molecular orbital (LUMO). These HOMO and LUMO states determine the optical and electrical properties of the materials. Organic photovoltaic devices[2] consist of a transparent electrode, typically a conducting oxide such as indium-tin oxide, two organic light-absorbing layers, and a second electrode. The two organic layers are made of different organic semiconductors, one with an electron-donor character and the other with an electron-acceptor character. Electron-donor molecules exhibit a low ionization potential, while electron-acceptor molecules possess a high electron affinity. Thus, donor materials have high-lying HOMO levels, and acceptor materials have low-lying LUMO levels. As shown in Fig. 4.1(e), the donor and acceptor layers provide efficient hole and electron transport, and are referred to as the hole transport layer (HTL) and electron transport layer (ETL), respectively. In this bilayer structure, the interface between the HTL and ETL, i.e. donor/acceptor heterojunction, is responsible for the efficient dissociation of electron-hole pairs (excitons). While the challenge in inorganic solar cells is to have minority carriers migrate to opposite sides of the junction efficiently in order to

prevent them from recombining, the critical step in organic solar cells is to dissociate excitons before they decay to the ground state. This requires excitons to rapidly diffuse to the donor/acceptor interface where the dissociation occurs. Organic bulk heterojunction structures are designed to increase the fraction of photogenerated carriers that reach the dissociating donor/acceptor interface and contribute to photocurrent. The approach is motivated by the prospect of using spatially distributed junctions between donor and acceptor materials which interpenetrate each other. This arrangement permits efficient exciton dissociation throughout the active layers.

The efficiency of organic bulk heterojunction photovoltaic cells depends significantly on the morphology of donor and acceptor materials.[151-153] Therefore, it is imperative to understand the dependence of electronic processes at the interface on the morphology.[154] As shown schematically in two dimensions in Figs. 4.1(a) and 4.1(b), the morphology of an imaginary bulk heterojunction structure composed of electron and hole transport layers can be approximated by combinations of interfaces that are perpendicular or parallel to the current direction. Two simple bilayer structures shown in Figs. 4.1(c) and 4.1(d) are considered first in order to lay the basis for studies of the more complicated morphology shown in Fig. 4.1(b). In both bilayer structures, electronic processes occur at the interface perpendicular or parallel to the current direction shown in Figs. 4.1(c) and 4.1(d), respectively. Instead of the exciton dissociation, the following discussion presents a first attempt to explore the geometric effects of morphology on the related process of recombination at the interface. As shown in Fig. 4.1(e), we study the transport of separated charges toward the interfaces, which is followed by electron-hole pair recombination. The relevant effects of morphology on the electron-hole pair recombination process are of interest. Exploring interfacial recombination currents with different parameters, for instance, electric field, layer thickness, charge carrier mobility, and interfacial recombination rate, is of critical importance to fully examine effects of the morphology on the efficiency of bulk heterojunction devices.

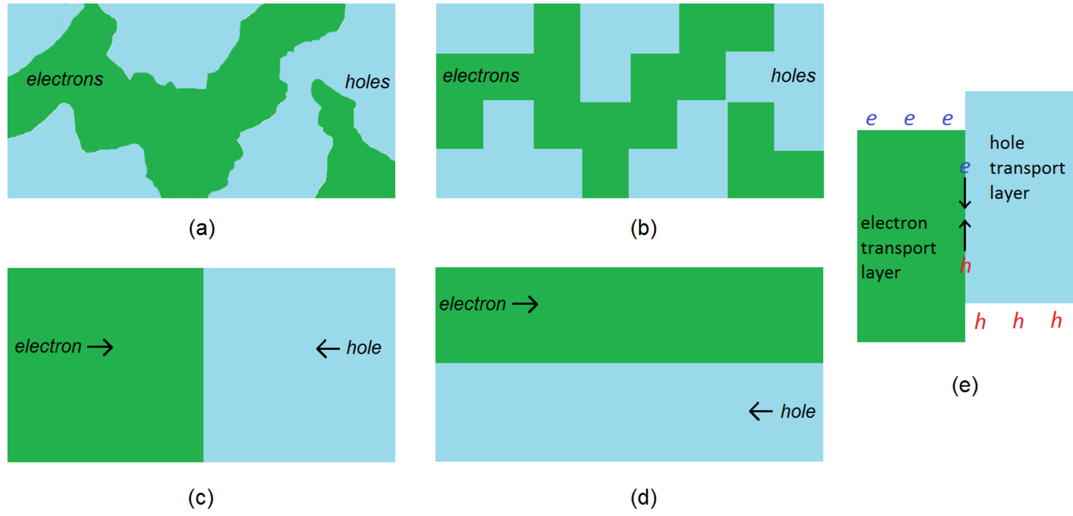

Figure 4.1: (a) Schematic bulk heterojunction structure. (b) Combination of interfaces perpendicular and parallel to the current direction is used to approximate the morphology of a bulk heterojunction structure. (c) Bilayer structure with interface perpendicular to the current direction. (d) Bilayer structure with interface parallel to the current direction. (e) Electrons injected from the electron transport layer and holes injected from the hole transport layer recombine at the interface.

4.2 Bilayer structure with interface perpendicular to the current direction

The bilayer structure with interface perpendicular to the current direction is discussed, assuming the electron (at $x = -L/2$) and hole (at $x = L/2$) injecting contacts are Ohmic contacts, as shown in Fig. 4.2. Recombination occurs only at the interface ($x = 0$) with a uniform electric field throughout the structure, F_x. Assuming equal mobilities for electrons and holes, analytical solutions of carrier concentrations may be obtained. Under steady state conditions, the continuity equations with currents including drift and diffusion are given by

$$\nabla \cdot J_p = \nabla \cdot J_n = 0, \tag{4.1}$$

$$J_p = +eD(dp/dx) + e\mu pF_x$$
$$J_n = -eD(dn/dx) + e\mu nF_x, \quad (4.2)$$

where k is the Boltzmann constant, T is the temperature, J_n and J_p are electron and hole currents, e is the elementary charge, μ is charge carrier mobility, D is the diffusivity, $n(x)$ and $p(x)$ are densities of electrons and holes as a function of x.

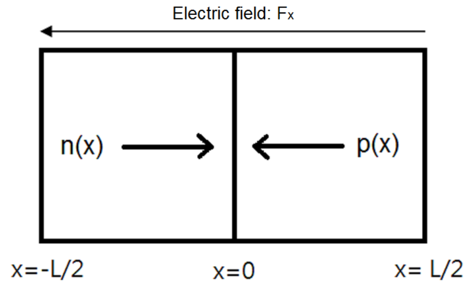

Figure 4.2: Schematic diagram for the bilayer structure with interface perpendicular to the current direction. Recombination occurs only at the interface.

The interfacial recombination current, J_{rec}, is modeled as a bimolecular process depending on the electron and hole densities near the interface. Clearly, the interfacial recombination current is equal to the electron and hole currents. Thus, the boundary conditions follow:

$$J_p = J_n = J_{rec} = e\gamma \cdot n(x = 0^-)p(x = 0^+), \quad (4.3)$$

$$n(x = -L/2) = n_0$$
$$p(x = +L/2) = p_0, \quad (4.4)$$

where γ is a constant interfacial recombination coefficient, n_0 and p_0 are carrier densities at the injecting contacts, and L is twice the length of each carrier transport layer.

One may solve Eqs. (4.1)–(4.4) analytically. In the absence of the electric field, i.e., $F_x = 0$, respective carrier densities decreasing linearly from the injecting contact toward the interface and the resulting currents are given by

$$\begin{aligned} n(x) &= \alpha_n (x + L/2) + n_0, \qquad -L/2 \le x \le 0 \\ p(x) &= \alpha_p (x - L/2) + p_0, \qquad 0 \le x \le L/2 \end{aligned}, \tag{4.5}$$

$$J_p = J_n = eD\alpha_p = -eD\alpha_n, \tag{4.6}$$

$$\begin{aligned} \alpha_p &= -\alpha_n = (-b + \sqrt{b^2 - 4c})/2 \\ b &= 4D/\gamma L^2 + 2p_0/L + 2n_0/L \\ c &= 4n_0 p_0 / L^2 \end{aligned}. \tag{4.7}$$

In the presence of the electric field, i.e., $F_x \neq 0$, electron and hole densities as a function of x and the resulting currents are:

$$\begin{aligned} n(x) &= n_0 + c_n (e^{\alpha x} - e^{-\alpha L/2}) \\ p(x) &= p_0 + c_p (e^{-\alpha x} - e^{-\alpha L/2}) \end{aligned}, \tag{4.8}$$

$$\begin{aligned} J_n &= \mu F_x (n_0 - c_n e^{-\alpha L/2}) \\ J_p &= \mu F_x (p_0 - c_p e^{-\alpha L/2}) \end{aligned}, \tag{4.9}$$

$$\begin{aligned} &c_n = (-b_n + \sqrt{\Delta_n})/2a_n, \qquad a_n = (1 - e^{-\alpha L/2})^2 \\ &b_n = e^{\alpha L/2}(p_0 - n_0)(1 - e^{-\alpha L/2})^2 + n_0 \cdot (1 - e^{-\alpha L/2}) + p_0 (1 - e^{-\alpha L/2}) + \mu F_x e^{-\alpha L/2}/\gamma \\ &\Delta_n = e^{\alpha L}(p_0 - n_0)(1 - e^{-\alpha L/2})^2 + (\mu F_x e^{-\alpha L/2}/\gamma)^2 \\ &\quad + 2(\mu F_x e^{-\alpha L/2}/\gamma)(p_0 + n_0)(1 - e^{-\alpha L/2}) \end{aligned}, \tag{4.10}$$

$$\begin{aligned} &c_p = (-b_p + \sqrt{\Delta_p})/2a_p, \qquad a_p = (1 - e^{-\alpha L/2})^2 \\ &b_p = e^{\alpha L/2}(n_0 - p_0)(1 - e^{-\alpha L/2})^2 + p_0 \cdot (1 - e^{-\alpha L/2}) + n_0 (1 - e^{-\alpha L/2}) + \mu F_x e^{-\alpha L/2}/\gamma \\ &\Delta_p = e^{\alpha L}(n_0 - p_0)(1 - e^{-\alpha L/2})^2 + (\mu F_x e^{-\alpha L/2}/\gamma)^2 \\ &\quad + 2(\mu F_x e^{-\alpha L/2}/\gamma)(n_0 + p_0)(1 - e^{-\alpha L/2}) \end{aligned}, \tag{4.11}$$

where Einstein's relation has been used. It is useful to define a dimensionless parameter, $V_{kT} = eF_x \cdot L/kT$. The drift plays a dominant role when V_{kT} is much larger than one, while the diffusion is the only mechanism if V_{kT} equals zero. In Fig. 4.3, normalized carrier density versus x/L is plotted assuming $n_0 = p_0$, and it is found that carrier density decreases linearly toward the interface without electric field. However, strong electric field ($V_{kT} >> 1$) results in the constant carrier density near the injecting contact and the decreasing carrier density when the interface is approached. In addition, the carrier density at the interface increases with increasing electric field, indicating that the interfacial recombination current increases.

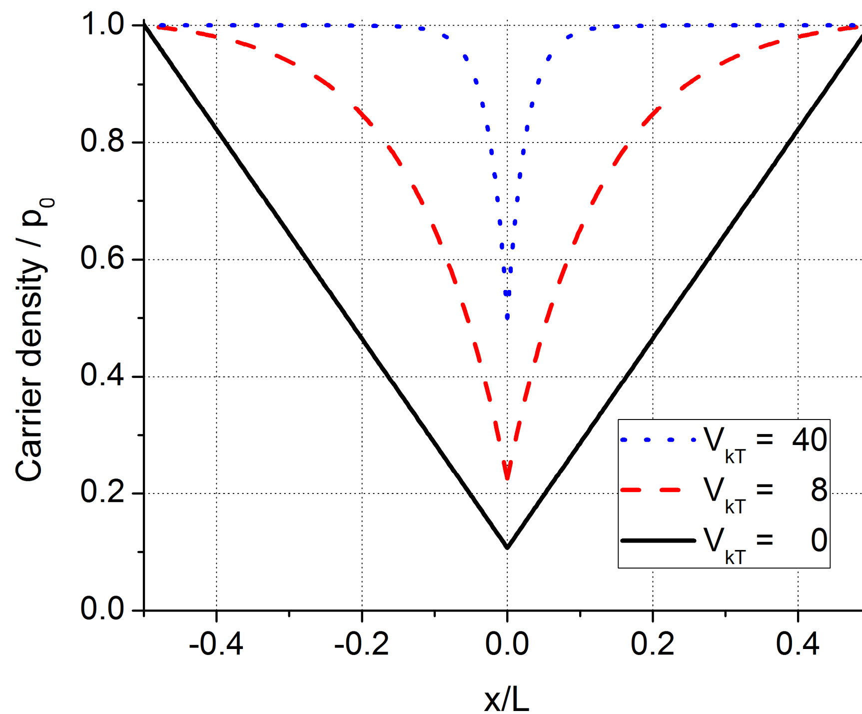

Figure 4.3: Normalized carrier density versus *x/L*, in the absence and presence of the electric field.

4.3 Bilayer structure with interface parallel to the current direction

Interfacial recombination current in bilayer structure with interface parallel to the current direction is explored next. As shown in Fig. 4.4(a), the structure modeled consists of electrons injected from the left (Ohmic) contact of the top layer and holes injected from the right (Ohmic) contact of the bottom layer. Similar to the previous example, recombination only occurs at the interface and the electric field is uniform, as shown in Fig. 4.4(b). However, because the interface is parallel to the field direction, this structure is considerably more interesting and challenging to model than the earlier example.

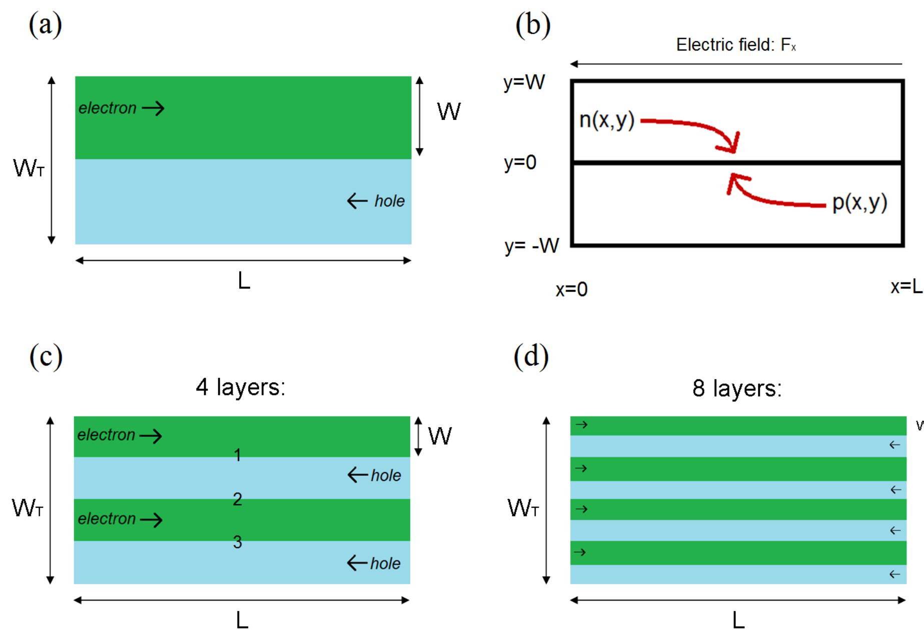

Figure 4.4: (a) and (b) Schematic diagrams for the bilayer structure with interface parallel to the current direction. Electrons injected from the top layer and holes injected from the bottom layer approach the interface and recombine. (c) Four-layer structure with three interfaces labeled. (d) Eight-layer structure with seven interfaces.

Steady-state carrier transport is govern by the continuity equations,

$$\nabla \cdot J_p = \nabla \cdot J_n = 0\,, \tag{4.12}$$

$$\begin{aligned} J_p &= +eD_p(\partial p/\partial x + \partial p/\partial y) + e\mu_p pF_x \\ J_n &= -eD_n(\partial n/\partial x + \partial n/\partial y) + e\mu_n nF_x \end{aligned}\,, \tag{4.13}$$

where μ_n and μ_p are electron and hole mobilities, D_n and D_p are electron and hole diffusivities, $n(x,y)$ and $p(x,y)$ are densities of electrons and holes. The boundary conditions are given by specifying the carrier flux at $y = \pm W$ and densities at $x = 0$ and $x = L$:

$$n(x=0) = n_0, \quad p(x=L) = p_0, \quad n(x=L) = p(x=0) = 0\,, \tag{4.14}$$

$$(\partial n/\partial y)\big|_{y=W} = (\partial p/\partial y)\big|_{y=-W} = 0\,, \tag{4.15}$$

where L is the length of the structure, W is the thickness of the electron or hole transport layers, and n_0 and p_0 are densities of electrons and holes at the injecting contacts. Interfacial recombination is formulated in terms of diffusion currents in y-direction at the interface as follows:

$$J_s(x) = eD_n(\partial n/\partial y)\big|_{y=0^+} = eD_p(\partial p/\partial y)\big|_{y=0^-} = e\gamma \cdot n(x, y=0^+)\,p(x, y=0^-)\,, \tag{4.16}$$

where γ is interfacial recombination coefficient. Equations (4.12)–(4.16) describes the interfacial recombination process in a 2-layer structure, and they may be modified to incorporate additional interfaces as shown in Figs. 4.4(c) and 4.4(d), in order to study geometric effects of multiple interfaces on interfacial recombination current on the basis of a constant W_T, where $W_T = \sum_{\text{the number of layers}} W$.

4.3.1 Profiles of normalized carrier densities and interfacial recombination

Equations (4.12)–(4.16) are solved with numerical methods discussed in Appendix D. To minimize parameters, we assume $\mu_n = \mu_p = \mu$, $D_n = D_p = D$, $n_0 = p_0$, and $W_T = L$. Normalized carrier density profiles are shown in Fig. 4.5. Without interfacial recombination, i.e., $\gamma = 0$, Fig. 4.5(a) shows normalized carrier densities that decrease linearly from the injecting contact toward the extracting contact in the case of $F_x = 0$, while for $F_x > 0$ (Fig. 4.5(c)) carrier densities decrease only near the far end from the relevant injecting contact. Figures 4.5(b) and 4.5(d) in which the interfacial recombination plays an important role are the cases of most interest. Evidently, carriers move toward the interface at which the recombination occurs. Similarly, normalized carrier density profiles of structures with multiple electron and hole transport layers are plotted in Fig. 4.6. In the cases of $F_x > 0$, the electric field results in more carriers injected into the structure.

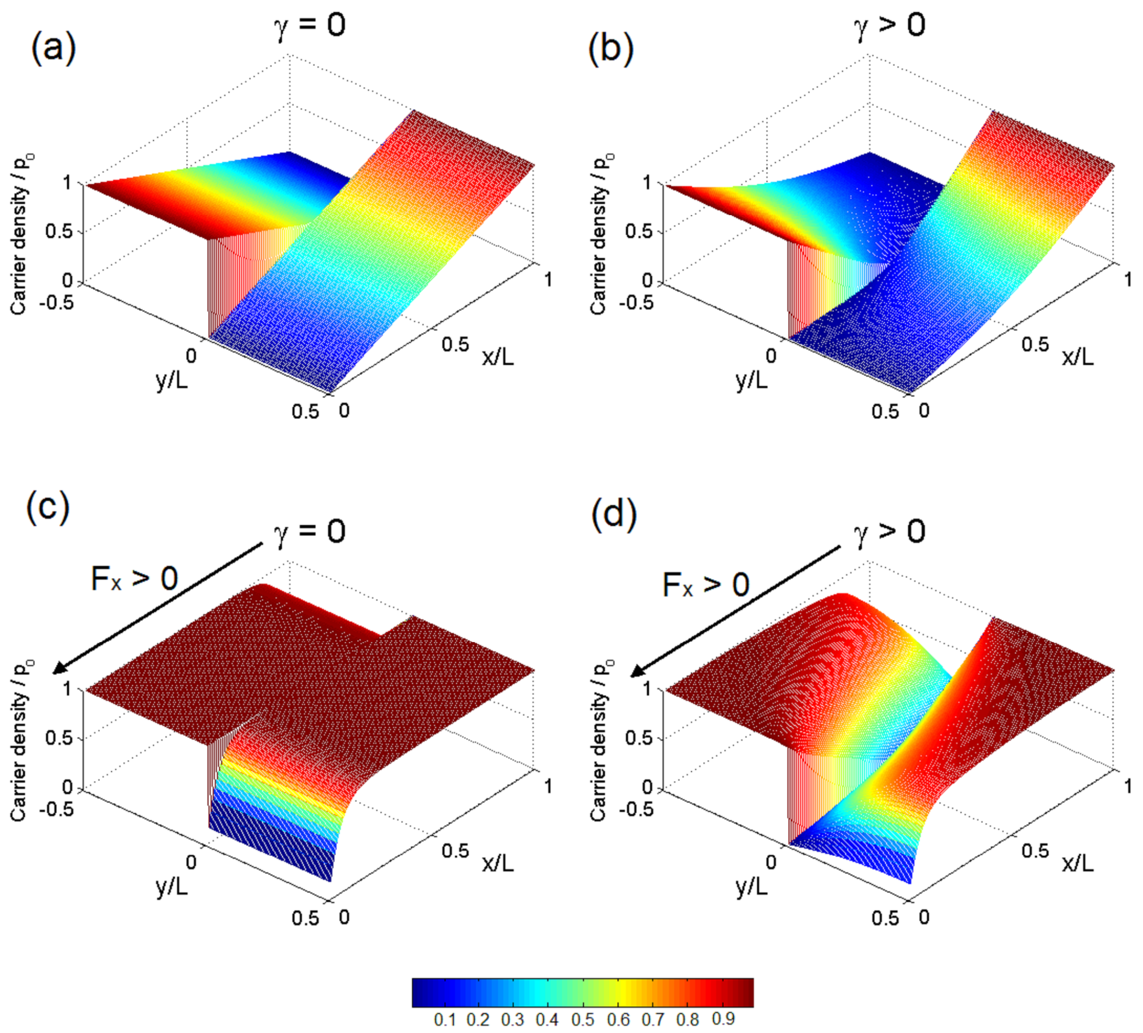

Figure 4.5: Normalized carrier density profiles are shown for four cases: (a) γ = 0 and F_x = 0, (b) γ > 0 and F_x = 0, (c) γ = 0 and F_x > 0, (d) γ > 0 and F_x > 0, which γ and F_x are taken to be the same as in (b) and (c), respectively.

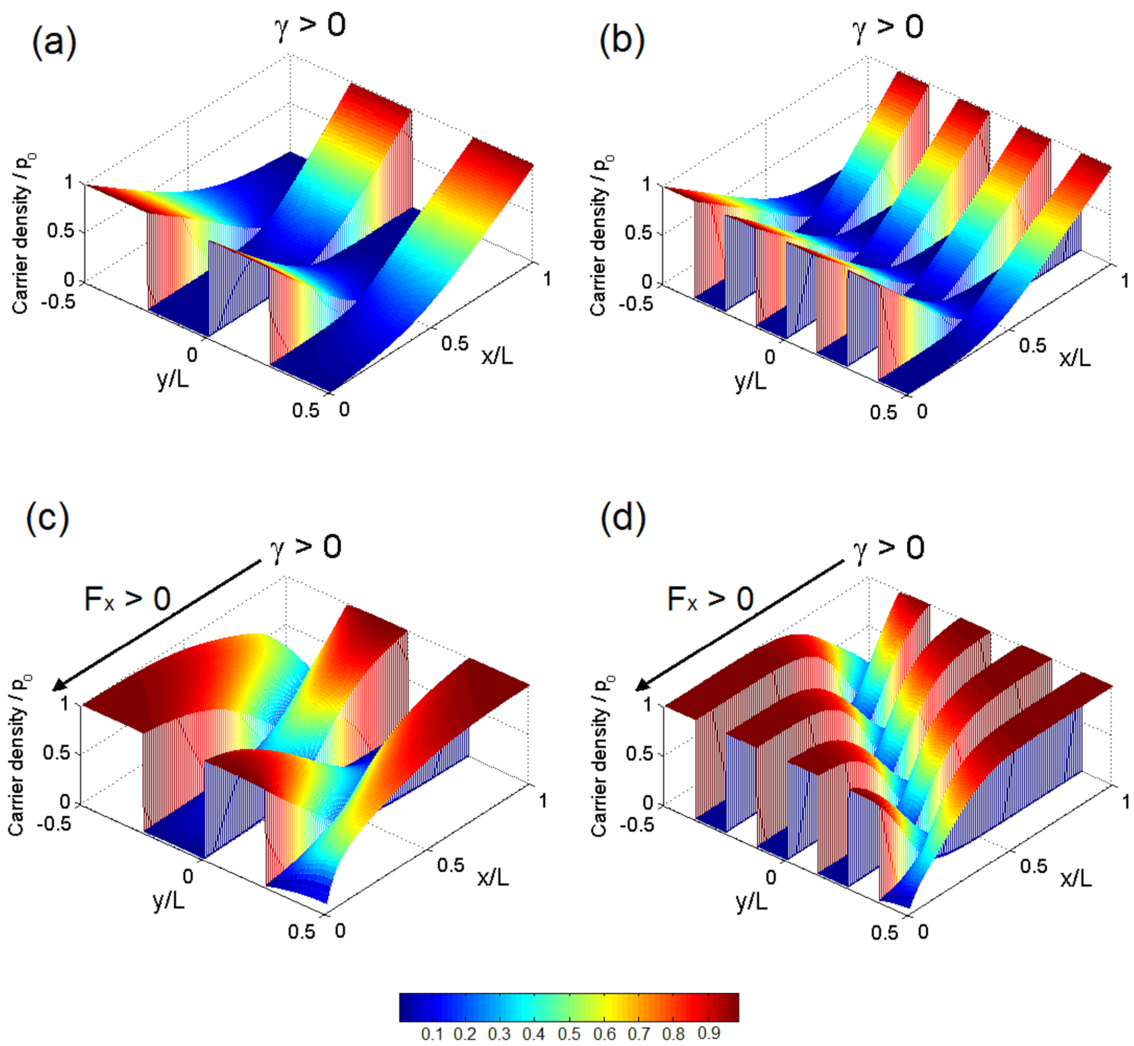

Figure 4.6: Normalized carrier density profiles of multiple-layer structures are shown for four cases: (a) 4-layer structure with F_x = 0, (b) 8-layer structure with F_x = 0, (c) 4-layer structure with F_x > 0, (d) 8-layer structure with F_x > 0 in which F_x is the same value as in (c). We take the value of γ to be the same in all calculations.

In Figs. 4.6(c) and 4.6(d), the asymmetric carrier density profiles at the interfaces are attributed to the opposite directions of carrier injections in the top and the bottom layer. To illustrate this feature with a counter example, Fig. 4.7(a) shows a symmetric 5-layer structure with electron injection layers at the top and the bottom. In that case, the normalized carrier density profile shown in Fig. 4.7(b) is symmetric, and the maximum interfacial recombination current occurs at $x/L = 0.5$.

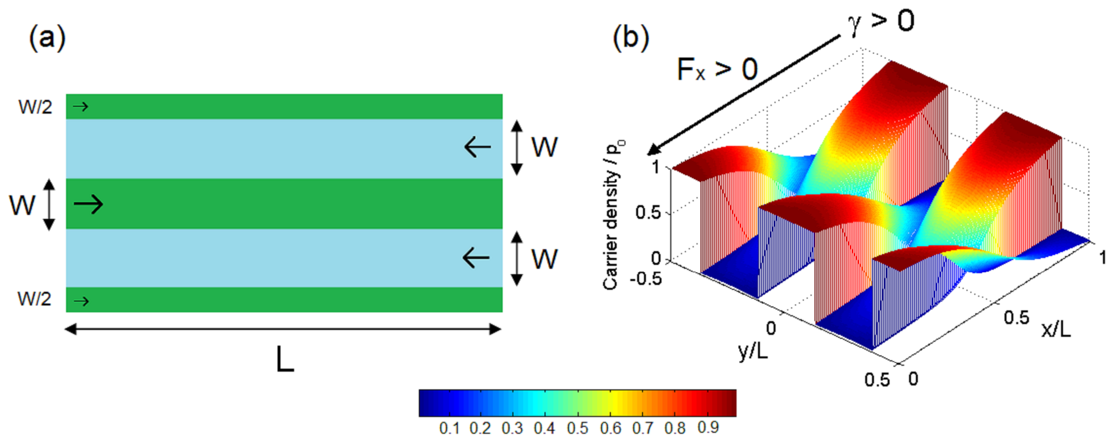

Figure 4.7: (a) Schematic diagram of a symmetric 5-layer structure with the same direction of carrier injections in the top and the bottom layer. (b) Normalized carrier density profile with the maximum recombination current at $x/L = 0.5$. The values of γ and F_x are the same as in Figs. 4.5 and 4.6.

Recombination currents are plotted as a function of x in Figs. 4.8–4.10. Generally the recombination reaches a maximum near the center of the interface but is suppressed near the injecting contacts. In Fig. 4.8, the solid curve represents the interfacial recombination profile for the case of Fig. 4.5(b), and the dashed curve represents the case of Fig. 4.5(d). It is apparent that the electric field leads to increasing recombination currents because of increasing injected carrier densities. In Figs. 4.9 and 4.10, recombination profiles of 4-layer structures are plotted. They correspond to the cases of Figs. 4.6(a) and 4.6(c), respectively. Obviously, the characteristics of interfacial recombination profiles in 2-layer and 4-layer structures are qualitatively similar.

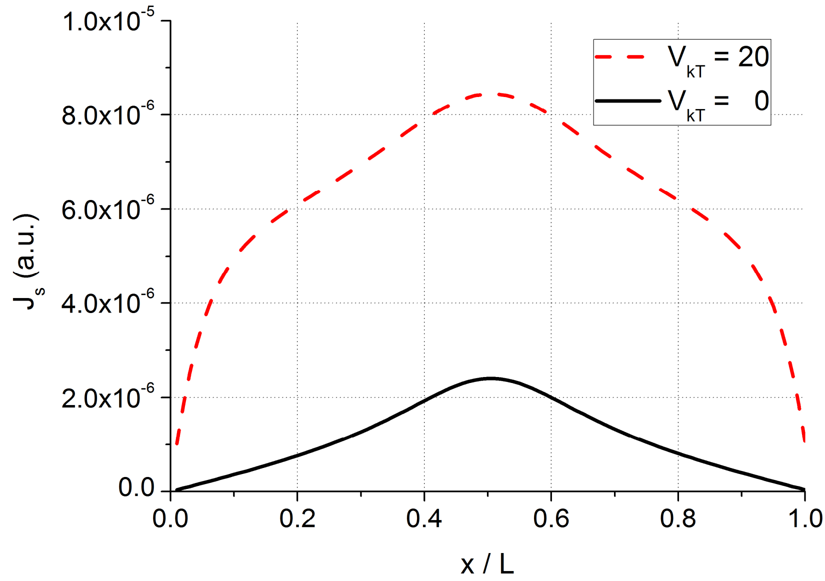

Figure 4.8: Characteristics of J_s versus x/L with and without the electric field. Recombination process reaches maximum at the center of the interface, and recombination current increases as a consequence of more injected carriers due to the electric field.

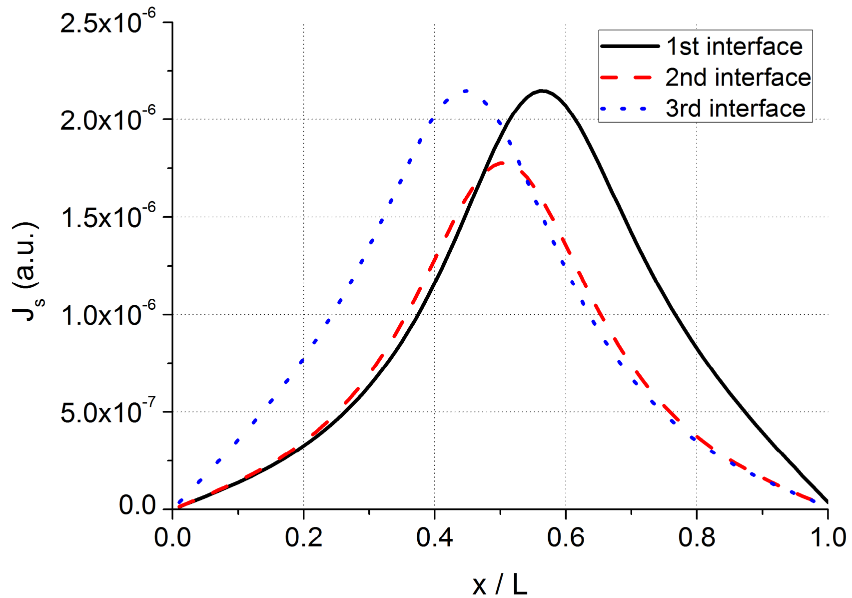

Figure 4.9: Characteristics of J_s versus x/L are shown for three interfaces labeled in Fig. 4.4(c), in the absence of the electric field.

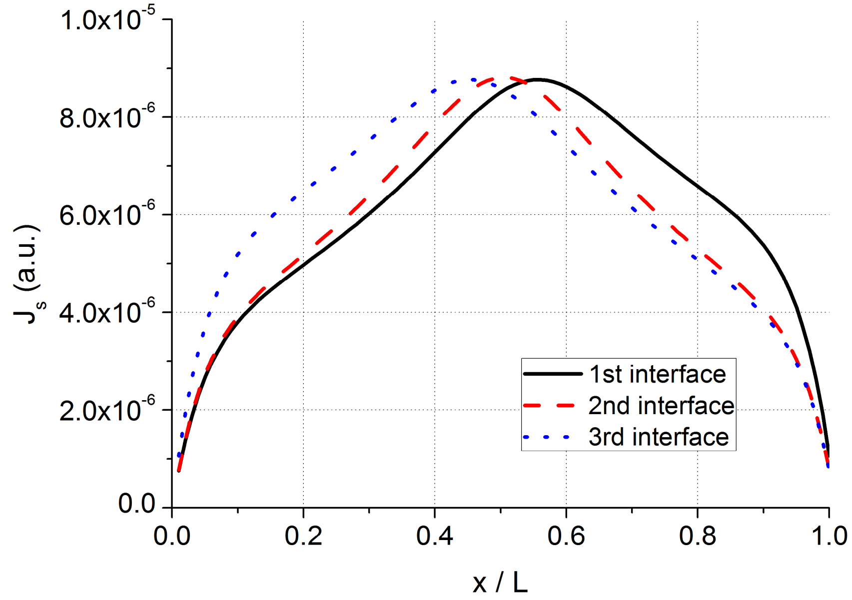

Figure 4.10: Characteristics of J_s versus x/L are shown for three interfaces labeled in Fig. 4.4(c), in the presence of the electric field.

4.3.2 Time scales of interfacial recombination and carrier transport

The dependence of interfacial recombination currents on time scales of both the recombination process at the interface and the carrier transport is explored. Since carriers recombining at the interface have to be transported from the injecting contacts, the consideration of the relationship between the interfacial recombination rate and carrier transport is important. In order to address the issue systematically, it is useful to define time scales for both interfacial recombination and carrier transport, as shown in Table 4.1. The time scale of the interfacial recombination, t_{rec}, is related to the length (L) of the interface, the interfacial recombination coefficient (γ), and the carrier density at the injecting contact (n_0 or p_0), while $t_{diff.L}$ and $t_{drift.L}$ are time scales related to diffusion and drift via L, D, μ, and F_x. In the following discussion, L is fixed as a constant for all calculated results. Another helpful term, t_L, is defined as the time scale of carrier

transport which includes both diffusion and drift. Without the electric field, $t_L = t_{diff.L}$, whereas $t_L = \min(t_{diff.L}, t_{drift.L})$ for $F_x > 0$. Essentially, it is the smallest time scale limits the whole process. As the result, the recombination rate limits the interfacial recombination current (I_{rec}) when $t_{rec} >> t_L$, but carrier transport restricts I_{rec} when $t_{rec} << t_L$. It is convenient to discuss recombination currents in terms of I_{rec} defined as

$$I_{rec} = \int_0^L J_s(x)dx . \quad (4.17)$$

Diffusion	$t_{diff.L} = L^2 / D$
Drift	$t_{drift.L} = L/(\mu F_x)$
Recombination	$t_{rec} = L/(\gamma \cdot n_0) = L/(\gamma \cdot p_0)$

Table 4.1: Time scales for interfacial recombination rate and carrier transport.

First, to explore geometric effects on the fraction of injected carriers which approach and recombine at the interface, we study the recombination ratio defined as I_{rec}/I_{in} where I_{in} is the current of the carrier injection at the injecting contact, i.e.,

$$I_{in} = \int_0^W J_n(x=0)dy = \int_0^{-W} J_p(x=L)dy . \quad (4.18)$$

where a bilayer structure with one interface (at $y = 0$) is considered. Nonetheless, the specific structure does not affect the results and conclusions reached. In Fig. 4.11, I_{rec}/I_{in} versus W/L is plotted for different values of t_{rec}/t_L, assuming constant t_L without electric field. Evidently, increasing t_{rec} gives rise to increasing recombination ratio. In addition, increasing W reduces the recombination ratio, indicating a decreasing fraction of injected carriers reaches the interface. Hence, recombination ratio depends on both the interfacial recombination rate and the thickness (W) of the carrier transport layer. Under certain

circumstances, for example, $W << L$ and $t_{rec} << t_L$, recombination ratio approaches 100% and almost all injected carriers recombine at the interface.

In Fig. 4.12, the influence of the electric field is considered, and the solid curve is the same as that in Fig. 4.11 for comparison. Assuming t_{rec} is constant, t_L decreases with increasing electric field and the recombination ratio decreases, as shown in Fig. 4.12. The increasing electric field facilitates carrier sweep from injecting to extracting contacts so that the fraction of carriers available to recombine at the interface is reduced. Figure 4.12 also shows decreasing recombination ratio with increasing t_{rec}/t_L, which is in agreement with Fig. 4.11. To sum up, recombination ratio varies with both t_{rec}/t_L and the thickness (W) of the carrier transport layers. This result lays the basis for the studies of the interfacial recombination current in multiple layers with different W but a constant W_T.

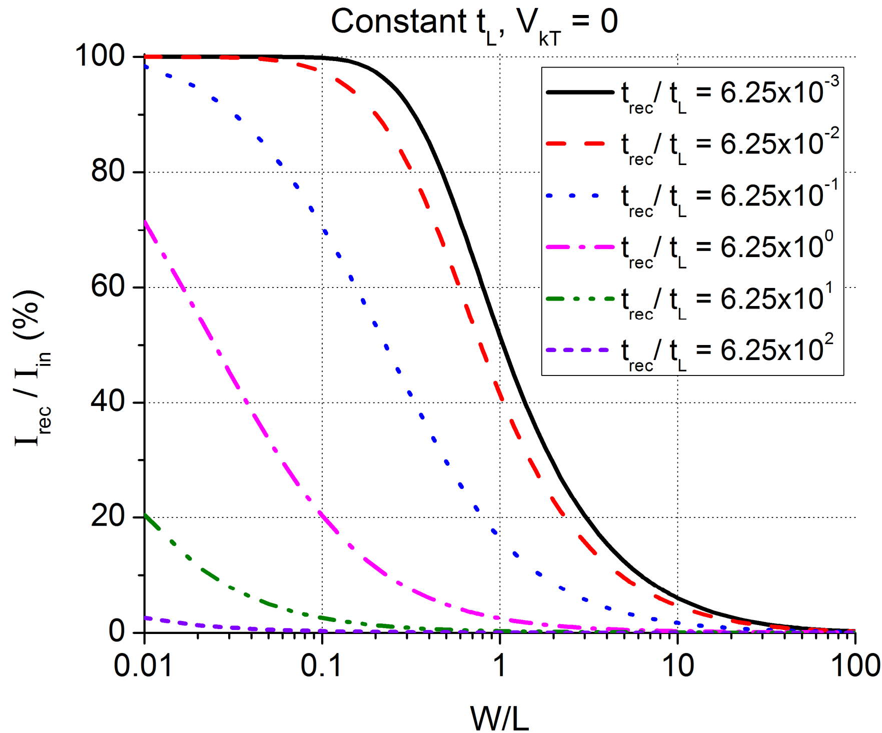

Figure 4.11: Recombination ratio (I_{rec}/I_{in}) versus W/L. The ratio depends on the interfacial recombination rate and the thickness (W) of the carrier transport layer.

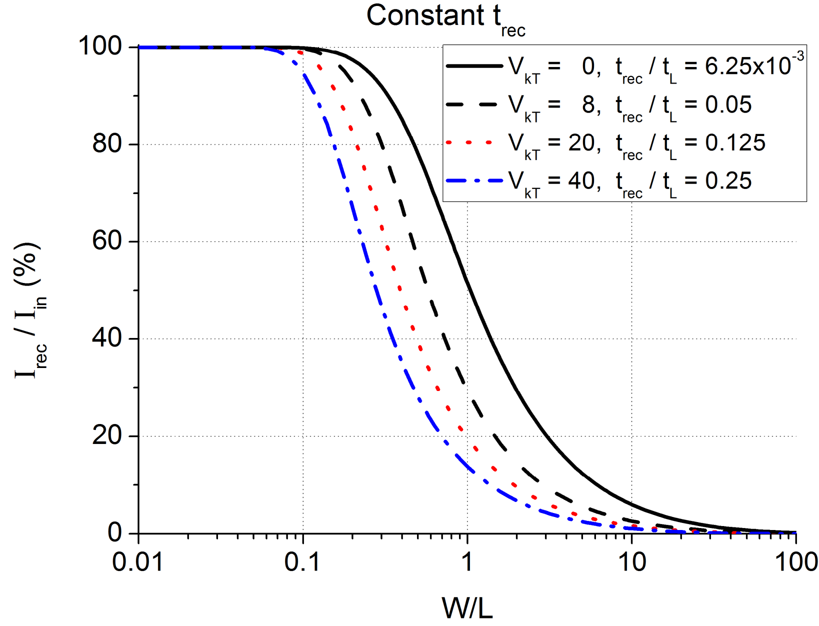

Figure 4.12: Recombination ratio (I_{rec}/I_{in}) versus W/L under the influence of the electric field. For comparison, the solid curve is the same as that in Fig. 4.11.

Next, we explore the effect of W_T on interfacial recombination currents in the absence of an electric field. Following the preceding discussion, one has to keep in mind that the decreasing recombination ratio does not necessary result in decreasing recombination currents. Even though the recombination ratio decreases with increasing W, the recombination current may increase primarily due to the added injected carriers contributed by the increasing W. In other words, characteristics of the recombination current depend not only on the recombination ratio (I_{rec}/I_{in}) but also on the amount of injected carriers. For $W_T = 2W$, we plot I_{rec} versus W_T/L in Fig. 4.13, which exhibits two competing effects. When $W_T < L$, I_{rec} increases with increasing W_T as a consequence of the additional injected carriers. The linear region in solid and dashed curves ($W_T/L < 0.1$) is attributable to situations in which the recombination ratio attains its maximum, as shown in the corresponding solid and dashed curves in Fig. 4.11. Under this condition, injected carriers which increase linearly with W_T determine I_{rec}, as indicated by the linear relationship observed. When $W_T > L$, however, decreasing recombination ratio has a

more pronounced effect on I_{rec}, which decreases with increasing W_T.

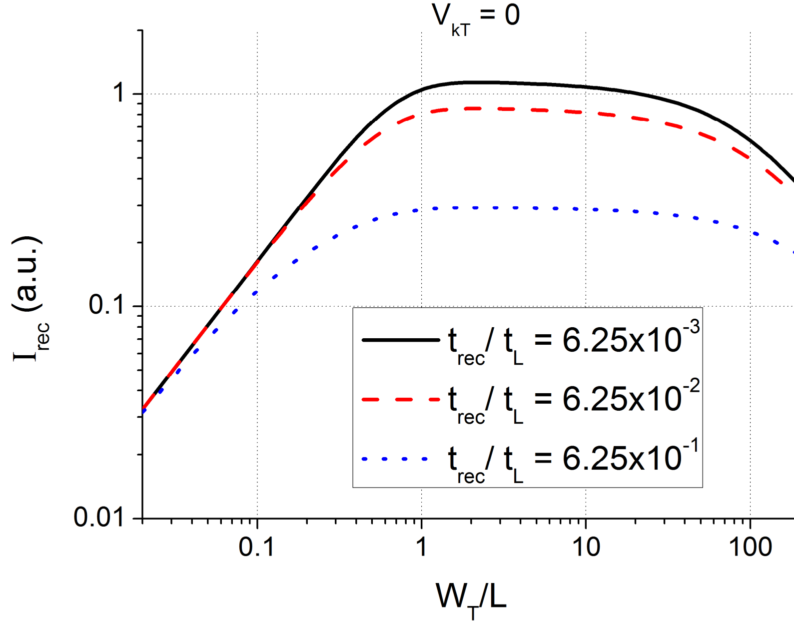

Figure 4.13: Characteristics of I_{rec} versus W_T/L indicates two competing effects.

Finally, we discuss the dependence of the interfacial recombination current on the time scales of both interfacial recombination and carrier transport. In order to exclude the effect of W_T on the interfacial recombination current, I_{rec} is normalized by W_T and characteristics of I_{rec}/W_T versus t_{rec}/t_L as plotted in Fig. 4.14 for zero electric field. When $t_{rec}/t_L >> 1$, the recombination rate limits the recombination current which varies linearly with t_{rec}/t_L. On the other hand, carrier transport as a limiting process ($t_{rec}/t_L << 1$) yields constant recombination current with respect to recombination rate. One interesting point to note in Fig. 4.14 is that the solid, dashed, and dotted curves represent the cases of $W << L$ and $t_{rec} << t_L$, and they merge in the range of maximum recombination ratio, indicating that the normalized recombination current (I_{rec}/W_T) reaches a maximum value when all the injected carriers recombine. This essential physical point may extend to the idea that due to the complete recombination of injected carriers, the resulting I_{rec} reaches its maximum value, and the increasing number of interfaces in the structure with a

constant W_T still leads to the same value of the interfacial recombination current. More detailed investigations addressing this point will be presented in the following section.

The time scale of carrier transport dominated by the electric field is also of interest. Time t_L associated with carrier transport decreases with increasing electric field. In order to present the effect of the electric field on the time scale of carrier transport, I_{rec}/W_T is expressed through the terms involving $t_{diff.L}$ only. In Fig. 4.15, compared with the case of zero electric field, the characteristics of I_{rec}/W_T versus $t_{rec}/t_{diff.L}$ shift toward the left when $V_{kT} > 0$. The solid curve represents the case without the electric field and is the same as that in Fig. 4.14. The transition of I_{rec}/W_T occurs at about $t_{rec}/t_{diff.L} = 1$ (since diffusion is the only factor in carrier transport). Considering the effect of the electric field, for example, dashed and dotted curves, the time scale of carrier transport decreases and therefore, the transition region shifts. The three dotted straight lines parallel to each other denote the points at which $t_{rec}/t_L = 1$, where $t_L = t_{diff,L}$ for $V_{kT} = 0$ and $t_L = \min(t_{diff.L}, t_{drift.L})$ for $V_{kT} > 0$. Also indicated are the increasing interfacial recombination current with increasing electric field, regardless of the decreasing recombination ratio associated with the non-zero electric field.

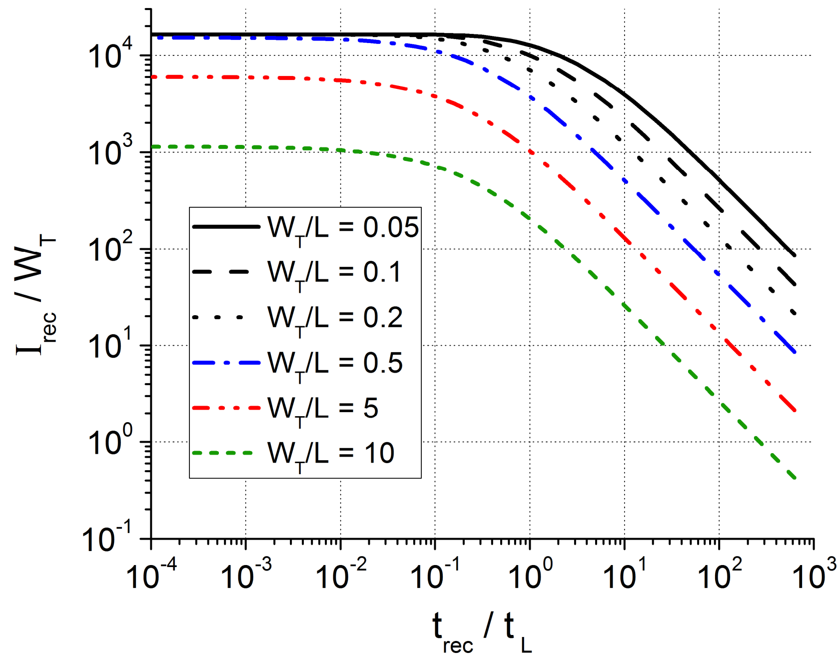

Figure 4.14: Characteristics of I_{rec}/W_T versus t_{rec}/t_L for six different values of W_T/L where $W_T = 2W$, in the absence of the electric field.

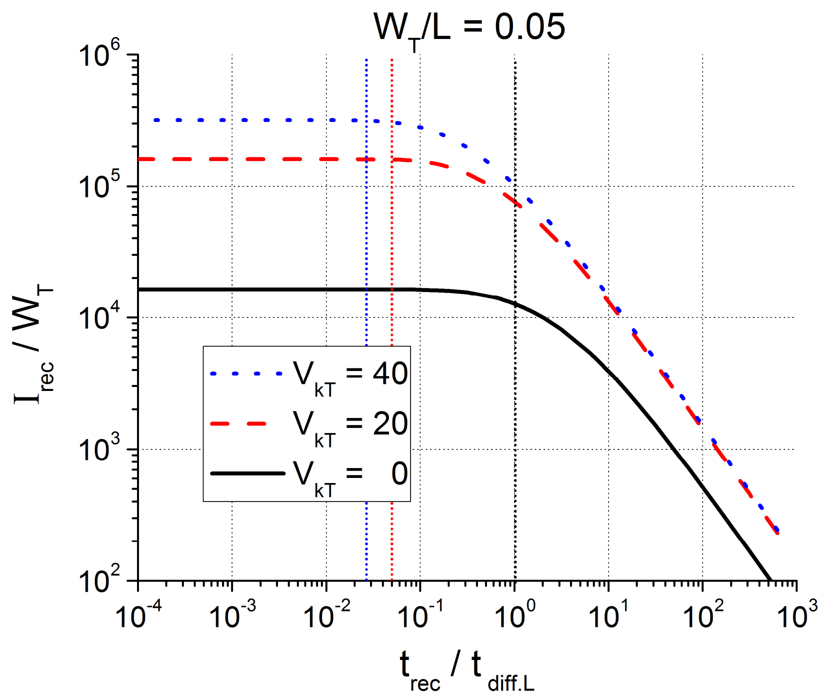

Figure 4.15: Characteristics of I_{rec}/W_T versus $t_{rec}/t_{diff.L}$ with and without the influence of the field.

4.3.3 Geometric effects of multiple interfaces on interfacial recombination

Since the recombination occurs only at the interface, it is of interest to explore how the number of interfaces in a given device volume affects the recombination current. Therefore, interfacial recombination current of multiple interfaces is examined assuming constant L and W_T. From the preceding discussion, we learn that the recombination ratio depends not only on the recombination rate (t_{rec}) but also on the layer thickness (W). In addition, I_{rec}/W_T approaches a maximum value as a consequence of complete recombination of all injected carriers. Here we calculate (total) interfacial recombination currents of 2-layer ($I_{2\text{-}lays}$), 4-layer ($I_{4\text{-}lays}$), and 8-layer ($I_{8\text{-}lays}$) structures keeping W_T constant, as shown in Fig. 4.4, and plot the current ratio, $I_{4\text{-}lays}/I_{2\text{-}lays}$ and $I_{8\text{-}lays}/I_{2\text{-}lays}$ with respect to W_T/L ranging from 0.02 to 200, where L is still held fixed. Intuitively, increasing number of interfaces increases the recombination current, and the current ratio, $I_{4\text{-}lays}/I_{2\text{-}lays}$ and $I_{8\text{-}lays}/I_{2\text{-}lays}$, should be equal to the ratio of the number of interfaces, i.e. three and seven, respectively. However, the calculated results show a quite different story: the current ratio significantly varies with W_T under certain conditions, indicating that geometric effects impact the interfacial recombination current dramatically.

First, the case of relatively slow recombination rate compared with carrier transport is discussed. In Fig. 4.16, the current ratio versus W_T/L is plotted in the absence and presence of the electric field. $I_{4\text{-}lays}/I_{2\text{-}lays}$ and $I_{8\text{-}lays}/I_{2\text{-}lays}$ increase with increasing W_T for $W_T < L$. Subsequently, when $W_T > L$ the current ratios reach the plateau of the ideal values, three and seven, respectively. Considering $W_T < L$, the current ratios are lower compared to the ideal values as a consequence of the interfacial coupling effect due to the short distance between interfaces, i.e., the recombination current at one interface may influence the recombination current at a neighboring interface. When $W_T > L$, the resulting recombination current associated with each of the additional interfaces with proportionally decreasing layer thickness (W) is the same as that of the one-interface bilayer ($I_{2\text{-}lays}$) structure. This result is attributed to the extremely small recombination ratio in the range of the layer thickness (W) considered, as shown in the short-dashed curve ($t_{rec}/t_L = 625$) in Fig. 4.11. In other words, interfaces are independent of each other

and the interfacial coupling effect vanishes. Essentially, the recombination ratio is related to the interfacial coupling effect which plays a significant role for the current ratio. Increasing recombination ratio enhances the interfacial coupling effect which results in decreasing current ratios, and vice versa. For instance, the recombination ratio decreases in the presence of the electric field, and thus, the coupling effect between interfaces is reduced, leading to increasing current ratios, as shown in Fig. 4.16.

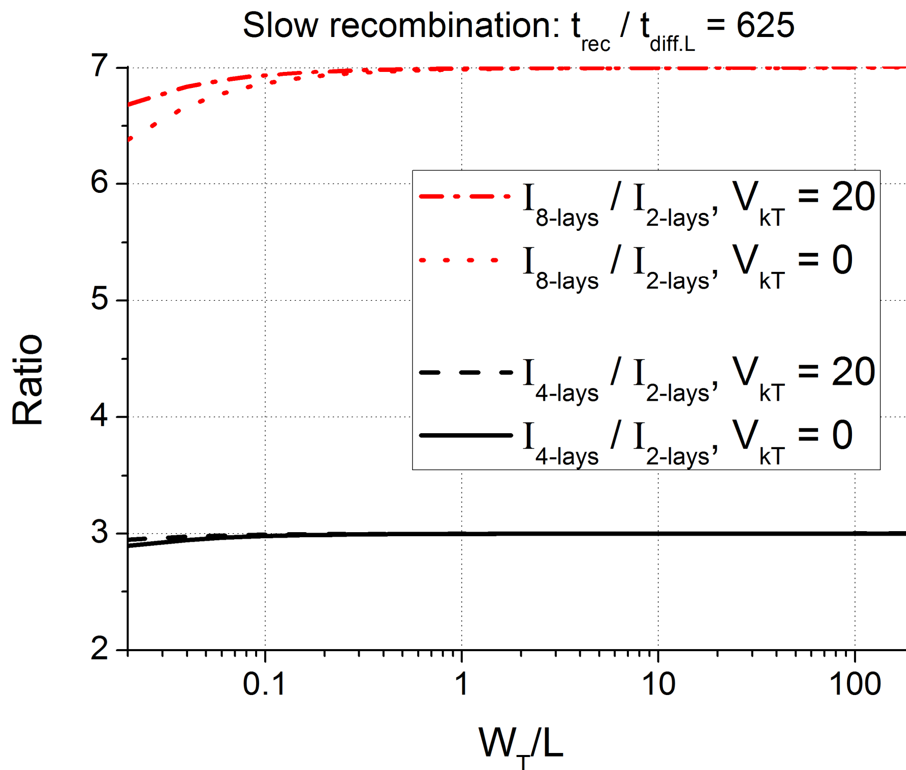

Figure 4.16: Current ratios ($I_{8\text{-}lays}/I_{2\text{-}lays}$ and $I_{4\text{-}lays}/I_{2\text{-}lays}$) versus W_T/L, in the case of slow recombination rate with and without the electric field.

Second, the case of relatively large recombination rate compared with carrier transport is explored. In Fig. 4.17, the current ratio versus W_T/L is plotted without the influence of the electric field. In contrast to the previous case, $I_{4\text{-}lays}/I_{2\text{-}lays}$ and $I_{8\text{-}lays}/I_{2\text{-}lays}$ equal unity as $W_T << L$ and subsequently increase with increasing W_T as $W_T > L$. Qualitatively speaking, the recombination ratio increases with any additional interfaces due to the proportionally decreasing layer thickness (W), implying that $I_{4\text{-}lays}/I_{2\text{-}lays}$ and $I_{8\text{-}lays}/I_{2\text{-}lays}$ should be both larger than unity for any given W_T. However, when $W_T << L$, the recombination ratio already reaches the maximum for the one-interface bilayer structure, giving rise to the maximum recombination current. Hence, the current ratios are equal to unity as a consequence of the recombination current remaining the same even with additional interfaces. When $W_T > L$, the recombination ratio diminishes with increasing W_T, resulting in the increasing current ratios. Generally speaking, in the complete range of W_T considered here, the maximum recombination ratio decreases with increasing W_T, and consequently, the interfacial coupling effect decreases, leading to increasing current ratios shown in Fig. 4.17. Also evident is that the current ratios marginally saturate at the ideal values before increasing further with increasing W_T. This phenomenon may be due to the two competing effects on the recombination current shown in Fig. 4.13, and more investigations are needed for the case of $W_T > L$ with $t_{rec} << t_L$.

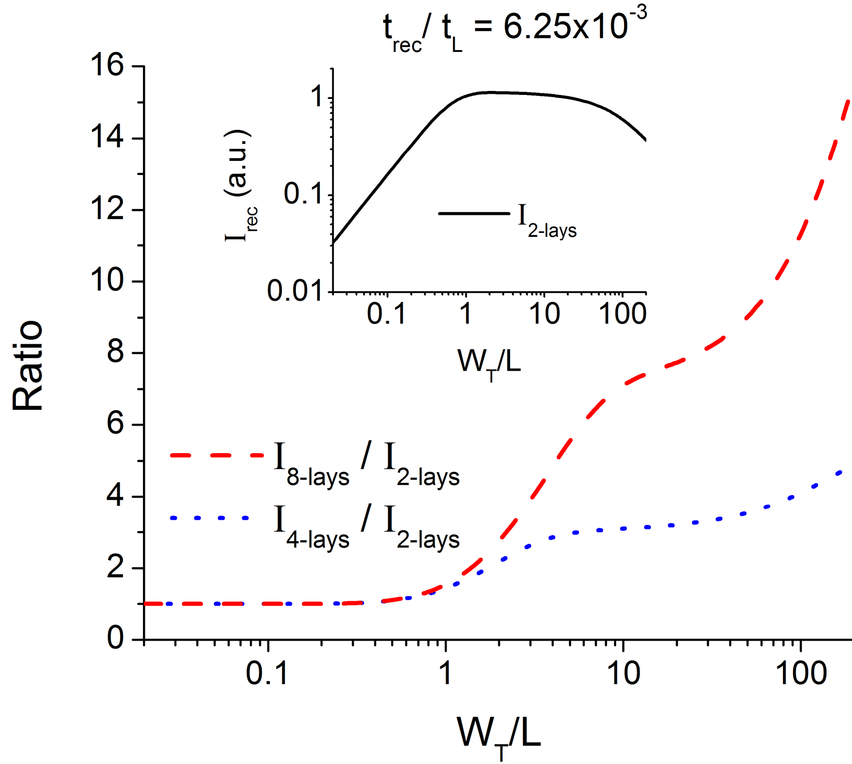

Figure 4.17: Current ratios ($I_{8\text{-}lays}/I_{2\text{-}lays}$ and $I_{4\text{-}lays}/I_{2\text{-}lays}$) versus W_T/L, in the case of fast recombination rate in the absence of the electric field. The dashed and dotted curves overlap at unity when $W_T << L$. Inset: Characteristics of recombination current ($I_{2\text{-}lays}$) versus W_T/L for the one-interface bilayer structure.

It is instructive to express $I_{N\text{-}lays}$ analytically in the case of $W_T << L$ and $t_{rec} << t_L$, where N is an integer and $N > 1$. The continuity equation modified from Eqs. (4.12) and (4.13) becomes

$$D_n(d^2n/dy^2) + G = 0\,, \tag{4.19}$$

assuming that the variation of the carrier density in x-direction is negligible compared with that in y-direction. Thus, the transport rate in x-direction, G, is constant and the carrier density only depends on x parametrically. The carrier density as a function of y is given by

$$n(y) = n_W - (G/2D_n)\cdot(y-W)^2\,, \tag{4.20}$$

where n_W denotes the carrier density at $y = W$. To validate Eq. (4.20), normalized carrier density profiles with respect to y, shown in Fig. 4.18 are calculated for five different x-locations. The parabolic dependence in Eq. (4.20) is in good agreement with the carrier density profile obtained numerically.

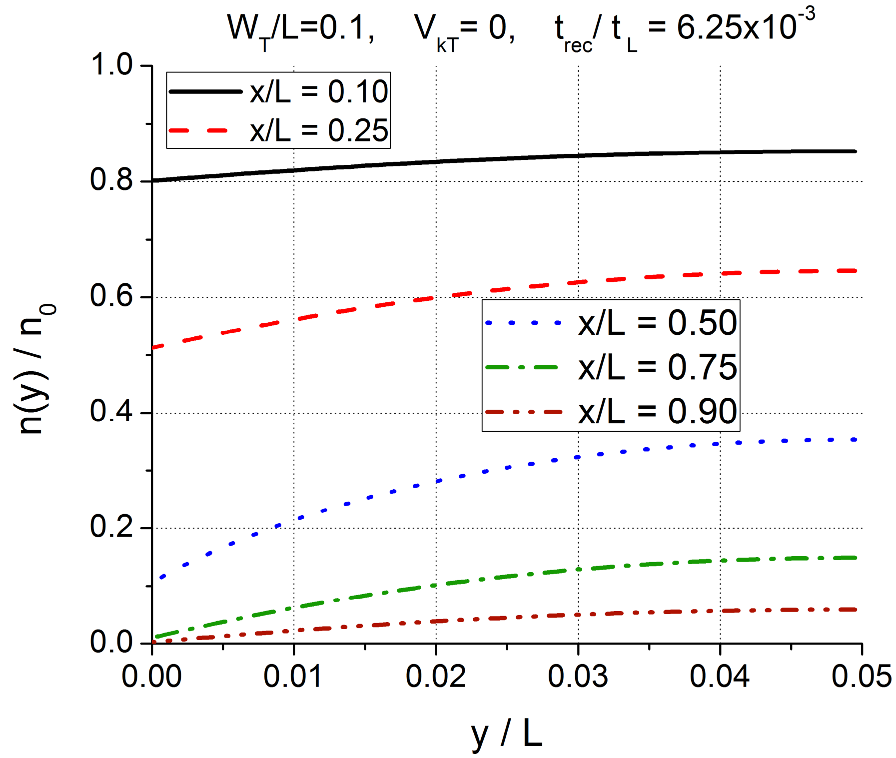

Figure 4.18: Normalized carrier density profiles with respect to the *y*-direction, for different points in the *x*-direction. Carrier densities show parabolic dependence on *y* and vary with *x* parametrically.

Moreover, the recombination current related to the diffusion current at the interface is given by

$$I_{rec} \propto D_n(dn/dy)\big|_{y=0} = WG\,, \tag{4.21}$$

where I_{rec} exhibits linear relationship with W, as in good agreement with the inset of Fig. 4.17. For multiple-interface structures, $I_{N\text{-}lays}$ is given by

$$I_{N-lays} = N \cdot I_{rec} = NWG = W_T G \, , \tag{4.22}$$

which is linearly proportional to W_T. Equation (4.22) is consistent with the calculated results in which the recombination current is independent of the number of interfaces provided that W_T is constant.

Compared with the results in the absence of an electric field, the current ratios increase under the influence of the electric field, as shown in Fig. 4.19. Clearly, the increasing current ratios result from the electric field which serves to reduce the recombination ratio.

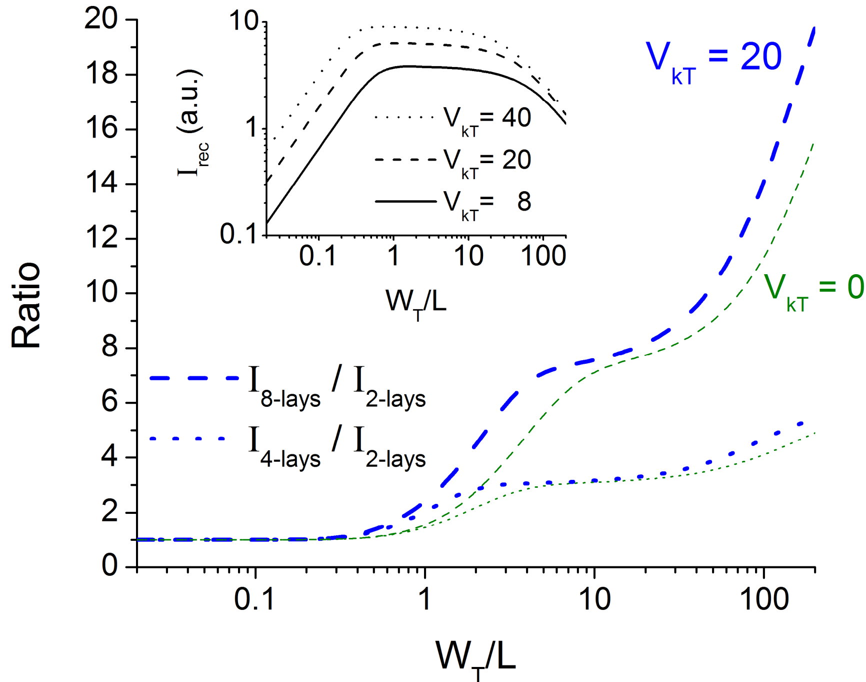

Figure 4.19: Current ratios ($I_{8\text{-}lays}/I_{2\text{-}lays}$ and $I_{4\text{-}lays}/I_{2\text{-}lays}$) versus W_T/L, in the case of large recombination rate in the presence of the electric field. Compared with the case without the electric field, current ratios increase as a consequence of reduced interfacial coupling. Inset: Characteristics of recombination current ($I_{2\text{-}lays}$) versus W_T/L for different values of the electric field.

4.3.4 Carrier balance

In the previous discussion, the values of electron and hole mobilities are taken to be the same. However, electron and hole mobilities are often quite different in practice. Therefore, effects of different electron and hole mobilities on interfacial recombination currents are of great importance. Here we explore the case of relatively fast recombination compared with carrier transport. In Fig. 4.20, normalized carrier density profiles calculated at the interface are plotted, and the maximum of the recombination current shifts toward the contact which injects the carrier with smaller mobility. Thus, carriers with smaller mobility limit recombination at the interface. Under the influence of an electric field, the carrier density increases and the maximum of the recombination current shifts further, as shown in Fig. 4.21.

In the absence of an electric field, the recombination current is examined on the basis of different time scales for electron and hole transport because $\mu_n \neq \mu_p$. Characteristics of I_{rec}/W_T versus $t_{rec}/t_{L-\mu_0}$ are plotted in Fig. 4.22 for three different cases in which μ_n and μ_p vary: first, $\mu_n = \mu_p = \mu_0$; second, $\mu_n = 10\mu_0$, $\mu_p = \mu_0$; third, $\mu_n = \mu_p = 10\mu_0$, and $t_{L-\mu_0} = eL^2/(\mu_0 kT)$. The solid and dotted curves are related to the cases of equal carrier mobilities but with different values in which the former is ten times larger than the latter. As a result, these two curves show similar characteristics of I_{rec} with one transition, i.e., the slope changes only once. However, the dashed curve represents the case of $\mu_n > \mu_p$ and its slope changes twice, as a consequence of the two different time scales of carrier transport. The recombination current depends on the recombination rate when $t_{rec} >> \max(t_{L-\mu_n}, t_{L-\mu_p})$, whereas the recombination current is constant with respect to the recombination rate when $t_{rec} << \max(t_{L-\mu_n}, t_{L-\mu_p})$.

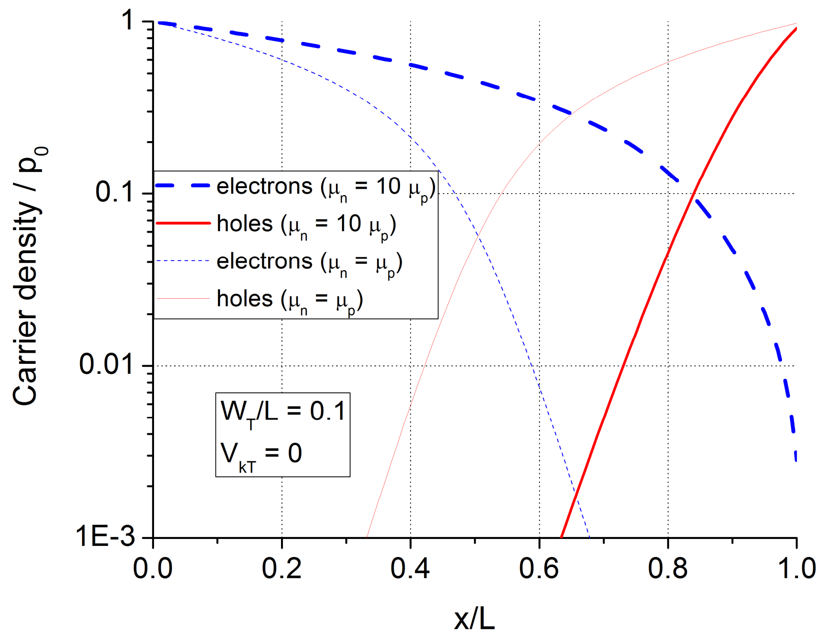

Figure 4.20: Normalized carrier density profiles calculated at the interface as a function of *x*/*L* without the electric field. Carriers with smaller mobility limit the recombination process.

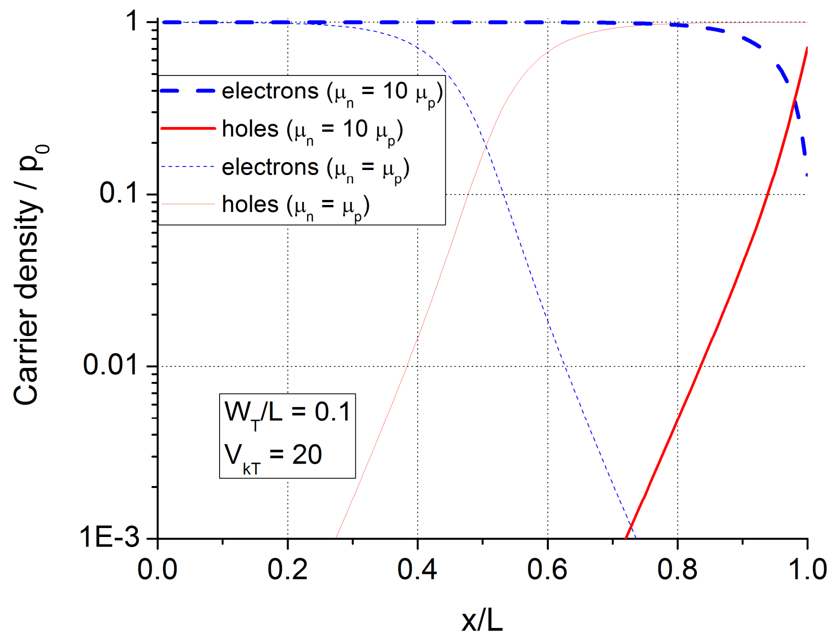

Figure 4.21: Normalized carrier density profiles taken at the interface as a function of *x*/*L* with the electric field which increases the amount of injected carriers.

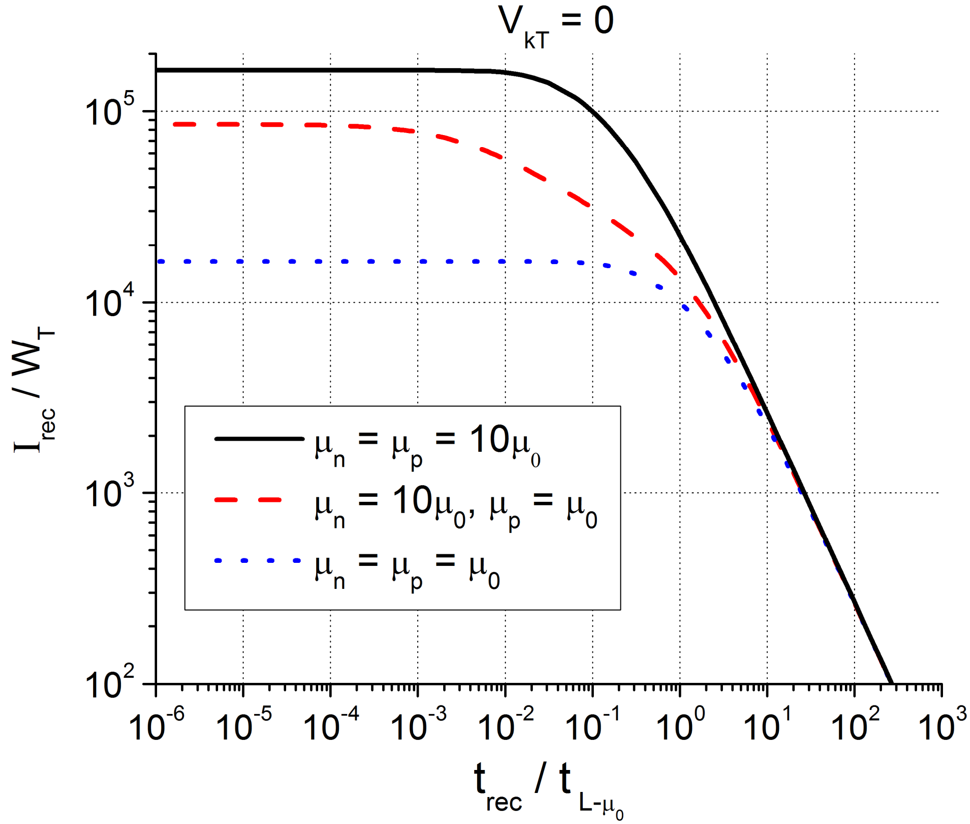

Figure 4.22: Characteristics of I_{rec}/W_T versus $t_{rec}/t_{L-\mu_0}$ for three different sets of parameters.

The current ratios ($I_{4\text{-}lays}/I_{2\text{-}lays}$ and $I_{8\text{-}lays}/I_{2\text{-}lays}$) for different electron and hole mobilities are also studied. In Fig. 4.23, the current ratios versus W_T/L are plotted, indicating that the ratios increase monotonically with increasing W_T in the range considered. Furthermore, the current ratios are always larger than unity, implying that the interfacial coupling effect does not reach its maximum even at $W_T/L = 0.02$.

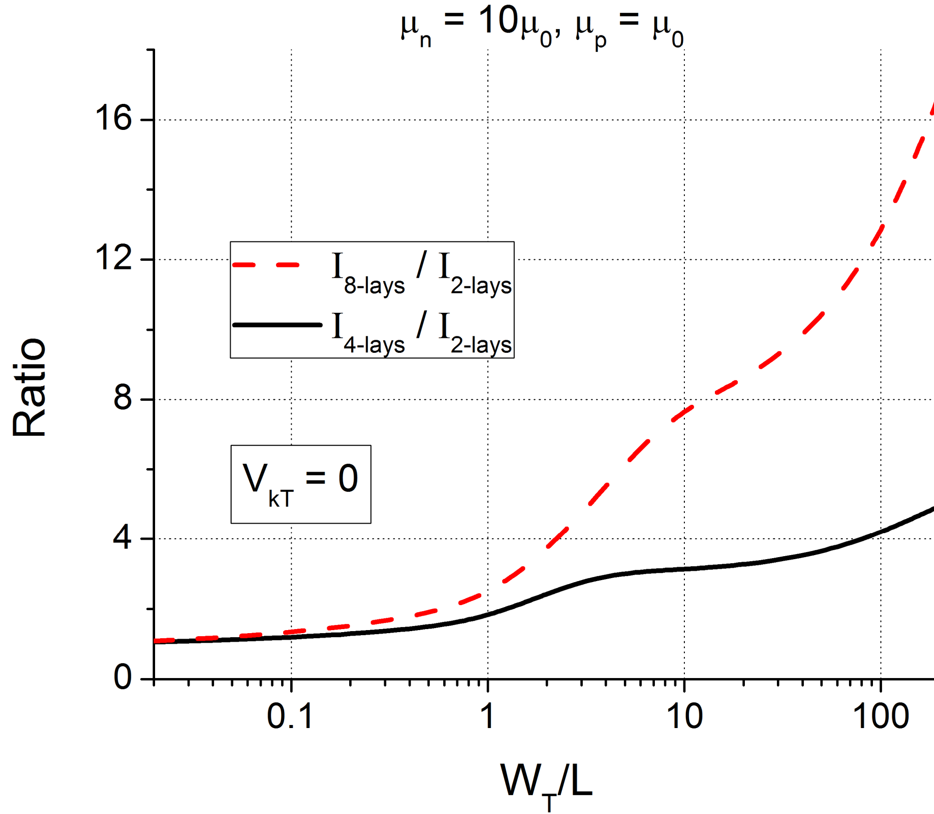

Figure 4.23: Current ratios ($I_{8\text{-}lays}/I_{2\text{-}lays}$ and $I_{4\text{-}lays}/I_{2\text{-}lays}$) versus W_T/L in the absence of the electric field where $\mu_n > \mu_p$. The current ratios both increase monotonically with increasing W_T.

4.4 Conclusion

In organic bulk heterojunction photovoltaic devices, the donor/acceptor heterojunction is distributed throughout the bulk of the composite materials, enabling efficient exciton dissociation. In this thesis, we explore the geometric effects of the morphology on the related process of the carrier recombination at the interface. We investigate the transport of initially separated charge carriers toward the interfaces, followed by electron-hole pair recombination. Interfaces perpendicular and parallel to the current direction are examined. The interfacial recombination currents are calculated

with different parameters, for instance, electric field, layer thickness, the number of interfaces, charge carrier mobility, and interfacial recombination rate. In the bilayer structure with the perpendicular interface, all carriers recombine at the interface and the recombination current equals the total current assuming that the barrier is large enough to prevent injection across the interface. Under this condition, the carrier density at the interface increases with increasing electric field. In the bilayer structure with the parallel interface, the situation becomes more complex, because not all carriers injected need to recombine at the interface. Depending on the relative magnitude of the time scales of recombination and carrier transport, the fraction of injected carriers that reach the interface and subsequently recombine varies. The recombination ratio approaches its maximum value as the layer thickness becomes much smaller than the layer length. The maximum recombination ratio gives rise to maximum recombination current, which is independent of the number of interfaces in a constant-volume structure. This result is very interesting in that more interfaces in a given volume of the structure do not necessarily lead to an increasing recombination current. We also explore the carrier balance and effects of different electron and hole mobilities on the interfacial recombination current. Different time scales for the electron and hole transport alter the characteristics of the recombination current.

5 Summary and suggestions for future work

5.1 Transient charge carrier transport

5.1.1 Summary

We have modeled the transient charge carrier transport characteristics of OFET capacitors and compared calculated results to experimental data. Numerical and approximate analytical models for the formation and the depletion of the conducting channel can explain qualitatively the asymmetric characteristics between injection and extraction currents versus time observed in the experiments. The origin of the peak in the *I-V* characteristics can be illustrated well by both the resistor-capacitor circuit model charging the channel with a linear gate voltage profile and the geometric model which is used as a basis for the definition of an effective mobility. In order to include carrier dynamics, we construct a full numerical model with which the effect of traps on the effective carrier mobility in a wide range of trapping parameters can be studied. Trapping processes that are slow on the relevant time scale of the transient region have negligible impact on the effective mobility, but they may manifest themselves in threshold shifts that are observed during charge carrier extraction. Compared with the time scale of the transient region, very fast traps give rise to an average (steady state) mobility, while the effective mobility characterizing the injection transient is itself time dependent in the case of traps with time constants that are comparable to the transient time scale.

For carrier extraction transient with a step function gate voltage profile, a resistor-capacitor circuit model successfully explains the puzzling experimental data, which show very different characteristics of the current versus time depending on the final state of the channel. The conducting channel is depleted by an abrupt change of the (discharging)

gate voltage that leads to partially or completely depleted channels. In the long time limit, for the partially depleted channel, the current decreases approximately exponentially with the extraction rate related to the discharging voltage, while an approximate power law time dependence arises in the case of completely depleted channels. We investigate the carrier extraction dynamics by using a resistor-capacitor equivalent circuit model with a time-dependent resistance that describes the increasing resistance during channel depletion. The model leads to analytical results with two distinct current characteristics (exponential or power law relation with respect to time) depending on the final gate voltages. With traps, numerical results show that trapped carriers increase the channel resistance, giving rise to slower carrier extraction rates in both scenarios. Nevertheless, the effects of traps do not alter the basic finding that the discharging voltage has a strong impact on the current versus time characteristics.

5.1.2 Suggestions for future work

The measurement of the displacement currents associated with charge carrier injection and extraction from an OFET channel offers many opportunities for the study of traps. For the linear gate voltage profile, the integration of the displacement current over the cycle yields the total charge carrier density trapped, which then can give rise to threshold shifts for subsequent cycles. Clearly, a key feature of these experiments is the control of the time scales, which are determined by the channel length, the ramp rate, and free carrier mobility. Consequently, even in this simple case trapping and detrapping time scales can, to some extent, be separated through a systematic variation of r_V. However, modifying the voltage versus time profile, for example, by holding the voltage constant at either its maximum and/or its minimum value, should add considerable flexibility by allowing for the independent control of the initial state of the device for the charge injecting and/or the charge carrier extracting sweep.

Figure 5.1 shows a modified gate voltage profile (dashed line) for obtaining more information about traps. In this example, holes are injected into the channel beginning at

$t = 0$ s. Starting at $t = 1$ s, a constant gate voltage is applied for 5 seconds, followed by a decreasing gate voltage. During the time period (t_{const}) of constant gate voltage, trapping/detrapping events affect the characteristics of the current.

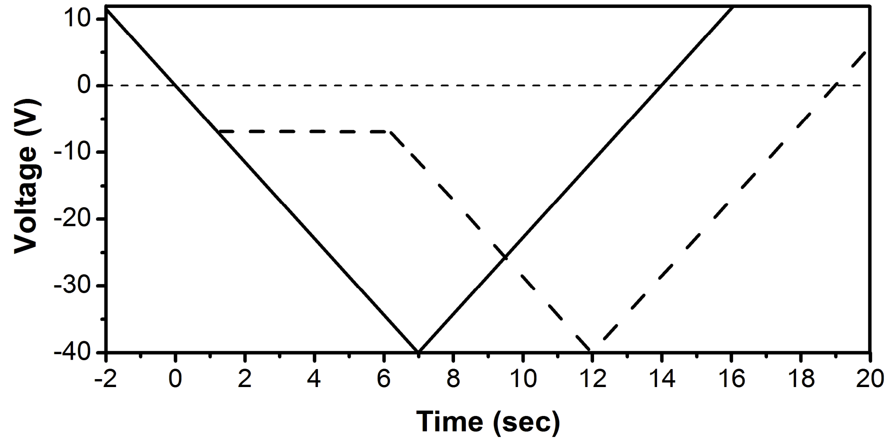

Figure 5.1: Modified gate voltage versus time profile for t_{const} = 5 s.

Figure 5.2 presents calculated results in which the gate voltage is held constant for 5 seconds at various values (with trapping parameters $\tau_{cap} = 0.01$ s and $\tau_{emi} = 0.5$ s). Evidently, characteristics of the 2nd injection processes (current peak, for example) are varied by the different initial conditions. Current peaks in the transient process of the 2nd injection period imply that essentially no (injected) mobile carriers exist in the channel as previously injected holes have been trapped, with the fraction of injected holes trapped depending on τ_{cap}, τ_{emi}, and t_{const}. In other words, we may vary not only the starting time but also the time period for which the gate voltage stays constant, and investigate trapping/detrapping events through the difference of the current peaks between the 1st and 2nd injection process. Figure 5.3 shows experimental results with similar current peaks in the transient process of the 2nd injection period as Fig. 5.2, except that the gate voltage is held constant for a much longer time ($t_{const} \approx 70$ s). In our device model, though, it is currently impractical to simulate such long periods of time due to the relatively small discretized time interval discussed in Appendix B. Hence, shorter time constants for the traps are chosen for the example calculations than would be appropriate for a quantitative simulation of the kind of device studied experimentally.

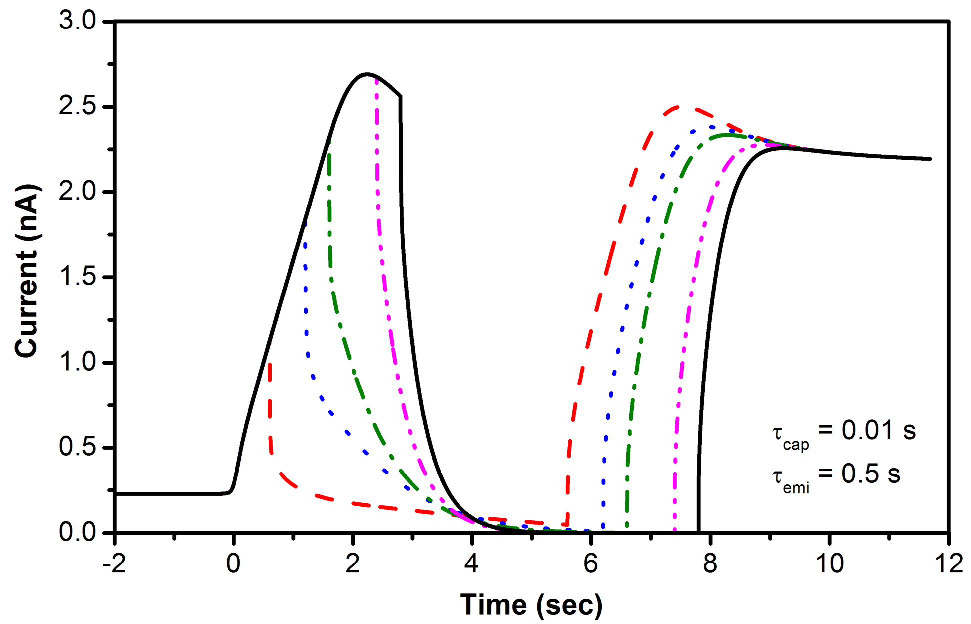

Figure 5.2: Calculated results (with traps) for various modified gate voltage profiles, holding the voltage constant at different values for 5 s.

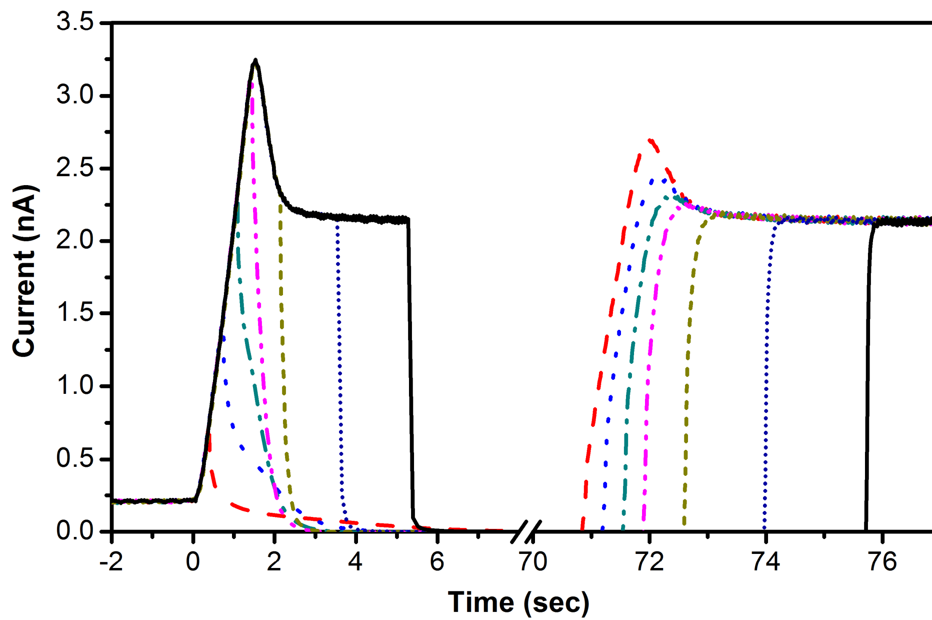

Figure 5.3: (Courtesy of Yan Liang): Experimental results for various modified gate voltage profiles, holding the voltage constant at different values for ~70 s.

5.2 Geometric effects on interfacial recombination

5.2.1 Summary

Morphological effects on electronic processes in organic bulk heterojunction structures are of critical importance in the interest of high efficiency organic photovoltaic cells. We discuss geometric effects on charge carrier recombination at the interface. Carrier recombination at the interface is studied for two bilayer structures with interfaces perpendicular and parallel to the current direction, which idealize the island-like morphology of mixed materials. In the bilayer model with the perpendicular interface, increasing electric field results in increasing carrier density at the interface where all injected carrier recombine. In the bilayer model with parallel interface, carriers injected from the respective contacts approach the interface and subsequently recombine. Recombination currents at the interface depend on the geometry and on parameters that set the time scales of the interfacial recombination and carrier transport. Under certain conditions, it is found that the resulting (total) recombination current of multiple-interface structures is the same as that of the single-interface structure. This result is of importance in that more interfaces of a given thickness of the structure do not necessarily lead to the increasing total recombination current. Carrier balance is also explored and effects of different electron and hole mobilities on the interfacial recombination current are presented.

5.2.2 Suggestions for future work

The effects of carrier balance need to be investigated in more detail, especially for the bilayer model with the perpendicular interface. In addition, it is simplistic to assume a uniform electric field in the carrier transport layers. The models, therefore, should be completed by adding Poisson's equation to account for the relation between the charge

distribution and the non-uniform electric field. Another important step is to examine the recombination current for a combination of perpendicular and parallel interfaces. Depending on the geometry, charge carrier mobility, and interfacial recombination rates, a certain fraction of injected carriers contributes to the recombination current at parallel interfaces, while the rest recombines completely at perpendicular interfaces. For the more complex morphology, one may also approximate recombination currents at multiple interfaces by considering a simpler (one-interface) structure with the current ratio discussed in Chapter 4. An analytical expression for the average interfacial recombination coefficient with respect to morphological parameters is currently the goal for the formulation of a simple one-dimensional model. Longer term it would be desirable to extend this type of modeling to the reverse process, i.e. electron-hole generation at the interface due to excitons dissociation. This time-reverse of the process examined here is a critical mechanism in the operation of organic photovoltaic cells.

References

[1] G.E. Moore, *Proc. of the IEEE* **86**, 82-85 (1998).

[2] C. W. Tang, *Appl. Phys. Lett.* **48**, 183 (1986).

[3] N. R. Armstrong, W. Wang, D. M. Alloway, D. Placencia, E. Ratcliff, and M. Brumbach, *Macromol. Rapid Commun.* **30**, 717 (2009).

[4] J. Y. Kim, Y. Qin, D. A. Stevens, O. Ugurlu, V. Kalihari, M. A. Hillmyer, and C. D. Frisbie, *J. Phys. Chem. C* **113**, 10790 (2009).

[5] Y. Zheng and J. Xue, *Polymer Reviews* **50**, 420 (2010).

[6] R. Pandey and R. J. Holmes, *Adv. Mater.* **22**, 5301 (2010).

[7] R. Pandey and R. J. Holmes, *Appl. Phys. Lett.* **100**, 083303 (2012).

[8] C. W. Tang and S. A. van Slyke, *Appl. Phys. Lett.* **51**, 913 (1987).

[9] J. H. Burroughes, D. D. C. Bradley, A. R. Brown, R. N. Marks, K. Mackay, R. H. Friend, P. L. Burns, and A. B. Holmes, *Nature* **347**, 539 (1990).

[10] D. Braun and A. J. Heeger, *Appl. Phys. Lett.* **58**, 1982 (1991).

[11] H. Baessler, *Polym. Adv. Technol.* **9**, 402 (1998).

[12] G. Parthasarathy, J. Liu, and A. R. Duggal, *Electrochem. Soc. Interface* **12**, 42 (2003).

[13] A. C. Morteani, A. S. Dhoot, J.-S. Kim, C. Silva, N. C. Greenham, C. Murphy, E. Moons, S. Cina, J. H. Burroughes, and R. H. Friend, *Adv. Mater.* **15**, 1708 (2003).

[14] N. C. Erickson and R. J. Holmes, *Appl. Phys. Lett.* **97**, 083308 (2010).

[15] N. C. Erickson and R. J. Holmes, *J. Appl. Phys.* **110**, 084515 (2011).

[16] A. Tsumura, H. Koezuka, and T. Ando, *Appl. Phys. Lett.* **49**, 1210 (1986).

[17] C. Reese, Mark Roberts, M.-mang Ling, and Z. Bao, *Materials Today* **7**, 20-27 (2004).

[18] H.E. Katz and J. Huang, *Ann. Rev. of Mater. Res.* **39**, 71-92 (2009).

[19] H. Klauk, *Chem. Soc. Rev.* **39**, 2643-66 (2010).

[20] T. Sekitani and T. Someya, *Adv. Mater.* **22**, 2643 (2010).

[21] R. H. Friend, R. W. Gymer, A. B. Holmes, J. H. Burroughes, R. N. Marks, C. Taliani, D. D. C. Bradley, D. A. D. Santos, J. L. Bredas, M. Loglund, and W. R. Salaneck, *Nature* **397**, 121 (1999).

[22] J. Shinar and R. Shinar, *J. Phys. D: Appl. Phys.* **41**, 133001 (2008), and references therein.

[23] B. Kippelen and J. L. Bredas, *Energy Environ. Sci.* **2**, 251 (2009).

[24] *ITRI (Industrial Technology Research Institute) Is Awarded as Gold Winner for Its FlexUPD at the WSJ Technology Innovation Awards*, http://www.itri.org.tw, last modified Sept. 2010, http://www.itri.org.tw/eng/econtent/news/news01_01.aspx?sid=5. Accessed: Mar. 21st, 2012.

[25] G. Horowitz, *Adv. Mater.* **10**, 365 (1998).

[26] C. D. Dimitrakopoulos and P. R. L. Malenfant, *Adv. Mater.* **14**, 99 (2002).

[27] C. R. Newman, C. D. Frisbie, D. A. da Silva, J. L. Bredas, P. C. Ewbank and K. R. Mann, *Chem. Mater.* **16**, 4436 (2004).

[28] D. Braga and G. Horowitz, *Adv. Mater.* **21**, 1473 (2009).

[29] S. R. Forrest, *Nature* **428**, 911 (2004).

[30] M. Bendikov, F. Wudl and D. F. Perepichka, *Chem. Rev.* **104**, 4891 (2004).

[31] A. R. Murphy and J. M. J. Frechet, *Chem. Rev.* **107**, 1066 (2007).

[32] A. Pron and P. Rannou, *Prog. Polym. Sci.* **27**, 135 (2002).

[33] H. Sirringhaus, *Adv. Mater.* **17**, 2411 (2005).

[34] Y.-Y. Lin, D. J. Gundlach, S. F. Nelson, and T. N. Jackson, *IEEE Trans. Electr. Dev.* **44**, 1325 (1997).

[35] D. J. Gundlach, Y.-Y. Lin, T. N. Jackson, S. F. Nelson, and D. G. Schlom, *IEEE Electr. Dev. Lett.* **18**, 87 (1997).

[36] H. Kakuta, T. Hirahara, I. Matsuda, T. Nagao, S. Hasegawa, N. Ueno, and K. Sakamoto, *Phys. Rev. Lett.* **98**, 247601 (2007).

[37] T. W. Kelley, L. D. Boardman, T. D. Dunbar, D. V. Muyres, M. J. Pellerite, and T. P. Smith, *J. Phys. Chem. B* **107**, 5877 (2003).

[38] T. W. Kelley, P. F. Baude, C. Gerlach, D. E. Ender, D. Muyres, M. A. Haase, D. E. Vogel, and S. D. Theiss, *Chem. Mater.* **16**, 4413 (2004).

[39] A. Facchetti, M. Yoon, and T. J. Marks, *Adv. Mater.* **17**, 1705 (2005).

[40] M. Matters, D. M. de Leeuw, M. J. C. M. Vissenberg, C. M. Hart, P. T. Herwig, T. Genus, C. M. J. Mutsaers, and C. J. Drury, *Optical Mater.* **12**, 189 (1999).

[41] B. Crone, A. Dodabalapur, Y.-Y. Lin, R. W. Filas, Z. Bao, A. LaDuca, R. Sarpeshkar, H. E. Katz, and W. Li, *Nature* **403**, 521 (2000).

[42] G. H. Gelinck, T. C. T. Genus, and D. M. de Leeuw, *Appl. Phys. Lett.* **77**, 1487 (2000).

[43] W. Fix, A. Ullmann, J. Ficker, and W. Clemens, *Appl. Phys. Lett.* **81**, 1735 (2002).

[44] A. Knobloch, A. Manuelli, A. Bernds, and W. Clemens, *J. Appl. Phys.* **96**, 2286 (2004).

[45] P. H. Woebkenberg, J. Bell, D. D. C. Bradley, T. D. Anthopoulos, F. Kooistra, J. C. Hummelen, and D. M. de Leeuw, *Appl. Phys. Lett.* **92**, 143310 (2008).

[46] J. Smith, R. Hamilton, M. Heeney, D. M. de Leeuw, E. Cantatore, J. E. Anthony, I. McCulloch, D. D. C. Bradley, and T. D. Anthopoulos, *Appl. Phys. Lett.* **93**, 253301 (2008).

[47] J. H. Cho, J. Lee, Y. Xia, B. Kim, Y. Y. He, M. J. Renn, T. P. Lodge, C. D. Frisbie, *Nature Material* **7**, 900 (2008).

[48] Y. Xia, W. Zhang, M. Ha, J. H. Cho, M. J. Renn, C. H. Kim, C. D. Frisbie, *Adv. Funct. Mater.* **20**, 587 (2010).

[49] K.-J. Baeg, D. Khim, D.-Y. Kim, S.-W. Jung, J. B. Koo, I.-K. You, H. Yan, A. Facchetti, and Y.-Y. Noh, *J. Polym. Sci. B: Polym. Phys.* **49**, 62 (2011).

[50] A. C. Huebler, G. C. Schmidt, H. Kempa, K. Reuter, M. Hambsch, and M. Bellmann, *Org. Electronics* **12**, 419 (2011).

[51] W. S. C. Roelofs, S. G. J. Mathijssen, J. C. Bijleveld, D. Raiteri, T. C. T. Genus, M. Kemerink, E. Cantatore, R. A. J. Janssen, and D. M. de Leeuw, *Appl. Phys. Lett.* **98**, 203301 (2011).

[52] A. Assadi, C. Svensson, M. Willander, and O. Inganaes, *Appl. Phys. Lett.* **53**, 195 (1988).

[53] H. Sirringhaus, P. J. Brown, R. H. Friend, M. M. Nielsen, K. Bechgaard, B. M. W. Langeveld-Voos, A. J. H. Spiering, R. A. J. Janssen, E. W. Meijer, P. Herwig, and D. M. de Leeuw, *Nature* **401**, 685 (1999).

[54] J.-F. Chang, B. Sun, D. W. Breiby, M. M. Nielsen, T. I. Soelling, M. Giles, I. McCulloch, and H. Sirringhaus, *Chem. Mater.* **16**, 4772 (2004).

[55] D. M. DeLongchamp, B. M. Vogel, Y. Jung, M. C. Gurau, C. A. Richter, O. A. Kirillov, J. Obrzut, D. A. Fischer, S. Sambasivan, L. J. Richter, and E. K. Lin, *Chem. Mater.* **17**, 5610 (2005).

[56] S. Cho, K. Lee, J. Yuen, G. Wang, D. Moses, A. J. Heeger, M. Surin, and R. Lazzaroni, *J. Appl. Phys.* **100**, 114503 (2006).

[57] V. Podzorov, E. Menard, A. Borissov, V. Kiryukhin, J. A. Rogers, and M. E. Gershenson, *Phys. Rev. Lett.* **93**, 086602 (2004).

[58] D. H. Kim, J. T. Han, Y. D. Park, Y. Jang, J. H. Cho, M. Hwang, and K. Cho, *Adv. Mater.* **18**, 719 (2006).

[59] M. M. Payne, S. R. Parkin, J. E. Anthony, C.-C. Kuo, and T. N. Jackson, *J. Am. Chem. Soc.* **127**, 4986 (2005).

[60] Y. Xia, V. Kalihari, C. D. Frisbie, N. K. Oh, and J. A. Rogers, Appl. Phys. Lett. 90, 162106 (2007).

[61] V. Sholin, S. A. Carter, R. A. Street, and A. C. Arias, *Appl. Phys. Lett.* **92**, 063307 (2008).

---

[62] B. Kahn, *Developments in Printable Organic Transistor*, (Pira International Ltd, Leatherhead, U.K., 2005).

[63] M. Pope and C. E. Swenberg, *Electronic Processes in Organic Crystals and Polymers*, 2nd ed. (Oxford, New York, 1999).

[64] M. Pope and C. E. Swenberg, *Ann. Rev. Phys. Chem.* **35**, 613 (1984).

[65] Xia Yu, *Fabrication and Characterization of Organic Single Crystal and Printed Polymer Transistors*, Ph.D. dissertation, University of Minnesota, 2009.

[66] F. Ortmann, F. Bechstedt, and K. Hannewald, *Phys. Stat. Sol. B* **428**, 511 (2011).

[67] N. F. Mott, *Contemp. Phys.* **10**, 125 (1969).

[68] P. G. Le Comber and W. E. Spear, *Phys. Rev. Lett.* **25**, 509 (1970).

[69] M. E. Gershenson, V. Podzorov, A. F. Morpurgo, *Rev. Mod. Phys.* **78**, 973 (2006).

[70] S. E. Shaheen, D. S. Ginley, and G. E. Jabbour, *MRS Bull.* **30**, 10 (2005).

[71] Y. L. Loo and I. McCulloch, *MRS Bull.* **33**, 653 (2008).

[72] C. J. Brabec and J. R. Durrant, *MRS Bull.* **33**, 670 (2008).

[73] S. Sun and N. S. Sariciftci, eds., *Organic Photovoltaics: Mechanisms, Materials, and Devices*, (Taylor and Francis, Boca Raton, FL, 2005).

[74] B. C. Thompson and J. M. J. Frechet, *Angew. Chem. Int. Ed.* **47**, 58 (2008).

[75] Bryan W. Boudouris, *Polythiophene-Containing Block Copolymers for Organic Photovoltaic Applications*, Ph.D. dissertation, University of Minnesota, 2009.

[76] *Heliatek achieves new world record for organic solar cells with certified 9.8% cell efficiency*, http://www.heliatek.com, last modified Dec. 2011, http://www.heliatek.com/?p=1346&lang=en. Accessed: Mar. 21st, 2012.

[77] *Achieving the world's highest photoelectric conversion efficiency of more than 10%*, http://www.m-kagaku.co.jp, last modified June 2011, http://www.m-kagaku.co.jp/english/aboutmcc/RC/special/feature1.html. Accessed: Mar. 21st, 2012.

[78] R. N. Marks, J. J. M. Halls, D. D. C. Bradley, R. H. Friend, and A. B. Holmes, *J. Phys.: Condens. Matter* **5**, 1379 (1994).

[79] S. Barth and H. Baessler, *Phys. Rev. Lett.* **79**, 4445 (1997).

[80] V. M. Kenkre, P. E. Parris, and D. Schmidt, *Phys. Rev. B* **32**, 4946 (1985).

[81] A. A. Zakhidov and K. Yoshino, *Synth. Met.* **64**, 155 (1994).

[82] B. A. Gregg, J. Sprague, M. Peterson, *J. Phys. Chem. B* **101**, 5362 (1997).

[83] T. Offermans, P. A. van Hal, S. C. J. Meskers, M. M. Koetse, R. and A. J. Janssen, *Phys. Rev. B* **72**, 045213 (2005).

[84] A. C. Morteani, P. Sreearunothai, L. M. Herz, R. H. Friend, and C. Silva, *Phys. Rev. Lett.* **92**, 247402 (2004).

[85] A. K. Ghosh and T. Feng, *J. Appl. Phys.* **49**, 5982 (1978).

[86] J. J. M. Halls and R. H. Friend, *Synth. Met.* **85**, 1307 (1996).

[87] J. J. M. Halls, K. Pichler, R. H. Friend, S. C. Moratti, and A. B. Holmes, *Appl. Phys. Lett.* **68**, 3120 (1996).

[88] V. I. Arkhipov, P. Heremans, and H. Baessler, *Appl. Phys. Lett.* **82**, 4605 (2003).

[89] P. Peumans and S. R. Forrest, *Chem. Phys. Lett.* **398**, 27 (2004).

[90] S. Westenhoff, I. A. Howard, J. M. Hodgkiss, K. R. Kirov, H. A. Bronstein, C. K. Williams, N. C. Greenham, and R. H. Friend, *J. Am. Chem. Soc.* **130**, 13653 (2008).

[91] D. Veldman, Oe. Ipek, S. C. J. Meskers, J. Sweelssen, M. M. Koetse, S. C. Veenstra, J. M. Kroon, S. S. van Bavel, J. Loos, and R. A. J. Janssen, *J. Am. Chem. Soc.* **130**, 7721 (2008).

[92] M. Schubert, C. Yin, M. Castellani, S. Bange, T. L. Tam, A. Sellinger, H.-H. Hoerhold, T. Kietzke, and D. Neher, *J. Chem. Phys.* **130**, 094703 (2009).

[93] K. Maturova, S. S. van Bavel, M. M. Wienk, R. A. J. Janssen, and M. Kemerink, *Nano Lett.* **9**, 3032 (2009).

[94] R. Giridharagopal and D. S. Ginger, *J. Phys. Chem. Lett.* **1**, 1160 (2010).

[95] Derek M. Stevens, *Examination of Structure-Performance Correlations in Low Band Gap Polymer Solar Cells*, Ph.D. dissertation, University of Minnesota, 2010.

[96] C. Mueller, T. A. M. Ferenczi, M. Campoy-Quiles, J. M. Frost, D. D. C. Bradley, P. Smith, N. Stingelin-Stutzmann, and J. Nelson, *Adv. Mater.* **20**, 3510 (2008).

[97] J. Peet, M. L. Senatore, A. J. Heeger, and C. G. Bazan, *Adv. Mater.* **21**, 1521 (2009).

[98] M. Kitamura and Y. Arakawa, *J. Phys.: condens. Matter* **20**, 184011 (2008).

[99] C. D. Dimitrakopoulos, A. R. Brown and A. Pomp, *J. Appl. Phys.* **80**, 2501 (1996).

[100] Y. Y. Lin, D. J. Gundlach, S. F. Nelson and T. N. Jackson, *IEEE Electr. Device. Lett.* **18**, 606 (1997).

[101] M. Shtein, J. Mapel, J. B. Benziger and S. R. Forrest, *Appl. Phys. Lett.* **81**, 268 (2002).

[102] D. Knipp, R. A. Street, A. Volkel and J. Ho, *J. Appl. Phys.* **93**, 347 (2003).

[103] T. Manaka, E. Lim, R. Tamura and M. Iwamoto, *Nat. Photonics* **1**, 581 (2007).

[104] T. Manaka, F. Liu, M. Weis and M. Iwamoto, *Phys. Rev. B* **78**, 121302 (2008).

[105] T. Manaka, F. Liu, M. Weis and M. Iwamoto, *J. Phys. Chem. C* **113**, 10279 (2009).

[106] T. Manaka, F. Liu, M. Weis and M. Iwamoto, *J. Appl. Phys.* **107**, 043712 (2010).

[107] L. Dunn, D. Basu, L. Wang and A. Dodabalapur, *Appl. Phys. Lett.* **88**, 063507 (2006).

[108] L. Dunn and A. Dodabalapur, *J. Appl. Phys.* **107** 113714 (2010).

[109] R. Dost, A. Das and M. Grell, *J. Appl. Phys.* **104**, 084519 (2008).

[110] M. Weis, J. Lin, D. Taguchi, T. Manaka and M. Iwamoto, *J. Phys. Chem. C* **113**, 18459 (2009).

[111] D. Basu, L. Wang, L. Dunn, B. Yoo, S. Nadkarni, A. Dodabalapur, M. Heeney and I. McCulloch, *Appl. Phys. Lett.* **89**, 242104 (2006).

[112] S. Egusa, N. Geemma, A. Miura, K. Mizushima, and M. Azuma, *J. Appl. Phys.* **71**, 2042 (1992).

[113] S. Egusa, A. Miura, N. Gemma, and M. Azuma, *Jpn. J. Appl. Phys. 1* **33**, 2741 (1994).

[114] S. Ogawa, Y. Kimura, H. Ishii and M. Niwano, *Jpn. J. Appl. Phys. 2* **42**, L1275 (2003).

[115] S. Ogawa, T. Naijo, Y. Kimura, H. Ishii and M. Niwano, *Appl. Phys. Lett.* **86**, 252104 (2005).

[116] S. Ogawa, T. Naijo, Y. Kimura, H. Ishii and M. Niwano, *Synthetic Met.* **153**, 253 (2005).

[117] Y. Majima, D. Kawakami, S. Suzuki and Y. Yasutake, *Jpn. J. Appl. Phys. 1* **46**, 390 (2007).

[118] S. Ogawa, Y. Kimura, M. Niwano and H. Ishii, *Appl. Phys. Lett.* **90**, 033504 (2007).

[119] Y. Xia, V. Kalihari, C. D. Frisbie, N. K. Oh and J. A. Rogers, *Appl. Phys. Lett.* **90**, 162106 (2007).

[120] S. Suzuki, Y. Yasutake and Y. Majima, *Jpn. J. Appl. Phys.* **47**, 3167 (2008).

[121] E. Pavlica and G. Bratina, *J. Phys. D Appl. Phys.* **41**, 135109 (2008).

[122] S. Yoshita, R. Tamura, D. Taguchi, M. Weis, E. Lim, T. Manaka and M. Iwamoto, *J. Appl. Phys.* **106**, 024505 (2009).

[123] S. Suzuki, Y. Yasutake and Y. Majima, *Org. Elect.* **11**, 594 (2010).

[124] N. Abiko, K. Sugi, T. Suenaga, Y. Kimura, H. Ishii and M. Niwano, *Jpn. J. Appl. Phys.* **45**, 442 (2006).

[125] Y. Noguchi, N. Sato, Y. Tanaka, Y. Nakayama and H. Ishii, *Appl. Phys. Lett.* **92**, 203306 (2008).

[126] S. Lee, J. Hur and S. Lim, *J. Soc. Inf. Display* **18**, 103 (2010).

[127] R. Liu, Y. L. Lei, P. Chen, Q. L. Song and Z. H. Xiong, *J. Phys. D Appl. Phys.* **42** (2009).

[128] Yan Liang, *Examination of transient carrier behaviors in organic field-effect devices via displacement current measurement*, Ph.D. dissertation, University of Minnesota, 2011.

[129] Y. Liang, C. D. Frisbie, H.-C. Chang, and P. P. Ruden, *J. Appl. Phys.* **105**, 024514 (2009).

[130] H.-C. Chang, P. P. Ruden, Y. Liang, and C. D. Frisbie, *J. Appl. Phys.* **107**, 104502 (2010).

[131] G. Horowitz, R. Hajlaoui, and P. Delannoy, *J. Phys.* III **5**, 355 (1995).

[132] S. M. Sze, *Physics of Semiconductor Devices*, 2nd ed. (Wiley, New York, 1982).

[133] P. T. Landsberg and O. Engstroem, in *Handbook on Semiconductors*, edited by P. T. Landsberg (Elsevier, New York, 1992), Vol. 1.

[134] C. R. Newman, R. J. Chesterfield, M. J. Panzer, and C. D. Frisbie, *J. Appl. Phys.* **98**, 084506 (2005).

[135] Y. Liang, H.-C. Chang, P. P. Ruden, and C. D. Frisbie, *J. Appl. Phys.* **110**, 064514 (2011).

[136] A. C. Durr, F. Schreiber, M. Kelsch, H. D. Carstanjen, and H Dosch, *Adv. Mater.* **14**, 961 (2002).

[137] J. H. Cho, D. H. Kim, Y. Jang, W. H. Lee, K. Ihm, J. H. Hans, S. Chung, and K. Cho, *Appl. Phys. Lett.* **89**, 132101 (2006).

[138] N. J. Watkins, L. Yan, and Y. L. Gao, *Appl. Phys. Lett.* **80**, 4384 (2002).

[139] N. Koch, A. Kahn, J. Ghijsen, J. J. Pireaux, J. Schwartz, R. L. Johnson, and A. Elschner, *Appl. Phys. Lett.* **82**, 70 (2003).

[140] L. Diao, C. D. Frisbie, D. D. Schroepfer, and P. P. Ruden, *J. Appl. Phys.* **101**, 014510 (2007).

[141] I. Kymissis, C. D. Dimitrakopoulos, and S. Purushothaman, *IEEE Trans. Electron. Dev.* **48**, 1060 (2001).

[142] D. J. Gundlach, L. Zhou, J. A. Nichols, T. N. Jackson, P. V. Necliudov, and M. S. Shur, *J. Appl. Phys.* **100**, 024509 (2006).

[143] K. Asadi, Y. Wu, F. Gholamrezaie, P. Rudolf, and P. W. M. Blom, *Adv. Mater.* **21**, 4109 (2009).

[144] K. Ihm, S. M. Chung, T. H. Kang, and S. W. Cheong, *Appl. Phys. Lett.* **93**, 141906 (2008).

[145] T. Sawabe, K. Okamura, T. Sueyoshi, T. Miyamoto, K. Kudo, N. Ueno, and M. Nakamura, *Appl. Phys. A* **95**, 225 (2009).

[146] M. Nakamura, N. Goto, N. Ohashi, M. Sakai, and K. Kudo, *Appl. Phys. Lett.* **86**, 122112 (2005).

[147] X. H. Zhang, B. Domercq, and B. Kippelen, *Synth. Met.* **159**, 2371 (2009).

[148] S. D. Wang, T. Minari, T. Miyadera, K. Tsukagoshi, and Y. Aoyagi, *Appl. Phys. Lett.* **91**, 203508 (2007).

[149] C. A. Di, G. Yu, Y. Q. Liu, Y. L. Guo, Y. Wang, W. P. Wu, and D. B. Zhu, *Adv. Mater.* **20**, 1286 (2008).

[150] S. D. Wang, T. Minari, T. Miyadera, Y. Aoyagi, and K. Tsukagoshi, *Appl. Phys. Lett.* **92**,063305 (2008).

[151] E. Moons, *J. Phys.: Condens. Matter* **14**, 12235 (2002).

[152] F. Padinger, R. S. Rittberger, and N. S. Sariciftci, *Adv. Funct. Mater.* **13**, 85 (2003).

[153] W. L. Ma, C. Y. Yang, X. Gong, K. Lee, and A. J. Heeger, *Adv. Funct. Mater.* **15**, 1617 (2005).

[154] I. Juric, I. Batistic, and E. Tutis, *Phys. Rev. B* **77**, 165304 (2008).

Appendix

A. Hopping transport in disordered semiconductors

In this Appendix, we discuss hopping transport in disordered semiconductors. Carrier transport in disordered systems plays an essential role in several rapidly evolving research fields, such as amorphous inorganic and organic semiconductors. In these materials, the most important quantity related to the device performance is the charge carrier mobility, which arises predominantly from hopping processes between localized states. The hopping process consists of the energy activation and tunneling mechanism. Detailed balance implies a relationship between the space-dependent with energy-dependent terms. We present two distinct hopping characteristics, nearest-neighbor and variable-range hopping.

The hopping rate[1,2,3] ν_{ij} of carriers over a distance r_{ij} from a localized state i to a localized state j with respective energies ε_i and ε_j is given by

$$\nu_{ij} = \begin{cases} \nu_o \exp(-2r_{ij}/\alpha)\exp(\frac{\varepsilon_i - \varepsilon_j}{kT}), & \varepsilon_i < \varepsilon_j, \\ \nu_o \exp(-2r_{ij}/\alpha), & \varepsilon_i \geq \varepsilon_j, \end{cases} \tag{A.1}$$

where α is the localization length related to the electronic wave function of the localized state, k is the Boltzmann constant, T is the temperature, ν_o is the phonon frequency which is independent of ε_i and ε_j. As shown in Fig. A.1, the main features of the hopping rate are the exponential dependence on position and on energy, which are related to tunneling

[1] N. F. Mott and E. A. Davis, *Electronic Processes in Non-Crystalline Materials*, 2nd ed. (Oxford University, Oxford, 1979).
[2] H. Overhof, *J. Non-Cryst. Solids* **227**, 15 (1998).
[3] C. Godet, *Philos. Mag. B* **81**, 205 (2001).

and thermal activation, respectively. Equation (A.1) also satisfies detailed balance between forward and backward processes:

$$\nu_{ij} = \nu_{ji} \exp[(\varepsilon_i - \varepsilon_j)/kT]. \tag{A.2}$$

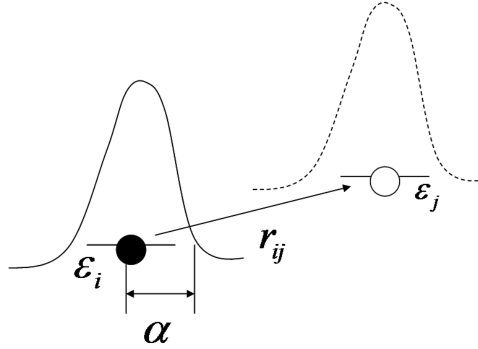

Figure A.1: Hopping process between two localized states related to energy difference (ε_i – ε_j) and the spatial distance r_{ij}, where α is the localization length.

The energy-dependent term in Eq. (A.1) may be neglected if the thermal energy kT is relatively large compared with the energy spread of the localized states. Under this condition, the hopping process solely depends on the spatial distance between localized states and nearest-neighboring hopping is dominant. Considering a system with localized states randomly distributed in space with the concentration N_o, the hopping rate is then given by

$$\nu_{ij} \propto \exp\left(-\frac{1}{\alpha N_o^{1/3}}\right), \tag{A.3}$$

where $N_o\alpha^3 << 1$.

At low temperatures, the hopping process depends on both the spatial and energy-dependent terms, and carriers may hop to distant states if they are energetically favored, as shown in Fig. A.2. Thus, the phenomenon of variable-range hopping plays a

significant role, and the most probable transitions are between those states which require little activation energy. In other words, the hopping distance r_{ij} increases with decreasing temperature. Since the thermal activation is of critical importance, there is substantial interest in obtaining the temperature dependence of the electrical conductivity associated with variable-range hopping. First, the space-dependent term in Eq. (A.1) may be substituted in the following way.[4] Assuming that an electron hops upward between localized states a distance r_{ij} apart, the number of states n_s situated between energy ε and $\varepsilon+\Delta\varepsilon$ within a sphere of radius r_{ij} is given by

$$n_s = \frac{4\pi}{3}(r_{ij})^3 \cdot g(\varepsilon) \cdot \Delta\varepsilon\,, \qquad \text{(A.4)}$$

where $g(\varepsilon)$ is the density of states. For the successful hopping process, there must be at least one state for the electron to hop to, i.e., n_s must be an integer equal or greater than one. This criterion relates the r_{ij} and the energy difference $\Delta\varepsilon$

$$r_{ij} \geq \left[\frac{3}{4\pi \cdot g(\varepsilon) \cdot \Delta\varepsilon}\right]^{1/3}. \qquad \text{(A.5)}$$

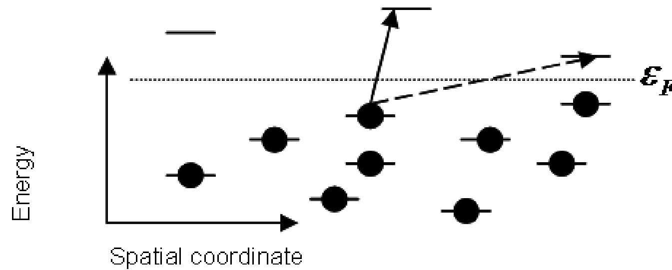

Figure A.2: The solid line represents nearest-neighbor hopping, while the dashed line represents variable range hopping.

[4] Kazuo Morigaki, *Physics of Amorphous Semiconductors*, (Imperial College Press, London, 1999).

Combining Eqs. (A.1) and (A.5) yields

$$\nu_{ij} \le \nu_o \exp\left\{-\left[\frac{6}{\alpha^3\pi\cdot g(\varepsilon)\cdot\Delta\varepsilon}\right]^{1/3} - \frac{\Delta\varepsilon}{kT}\right\}, \tag{A.6}$$

where $\Delta\varepsilon = \varepsilon_j - \varepsilon_i > 0$. Second, one has to calculate the most probable energy difference in Eq. (A.6) to relate the temperature and $\Delta\varepsilon$ at the maximum hopping rate. Therefore, differentiating the maximum hopping rate in Eq. (A.6) with respect to $\Delta\varepsilon$ yields the average energy difference $\Delta\bar{\varepsilon}$:

$$\frac{\partial \nu_{ij}}{\partial(\Delta\varepsilon)}\Big|_{\Delta\varepsilon=\Delta\bar{\varepsilon}} = 0\,, \tag{A.7}$$

$$\Delta\bar{\varepsilon} = \left[\frac{2(kT)^3}{9\alpha^3\pi\cdot g(\varepsilon)}\right]^{1/4}. \tag{A.8}$$

Substituting Eq. (A.8) into Eq. (A.6) yields

$$\nu = \nu_o \exp[-(T_o/T)^{1/4}], \tag{A.9}$$

where $\nu = \max(\nu_{ij})$, $T_o = B/[\alpha^3\pi\cdot g(\varepsilon)\cdot k]$, and B is a dimensionless numerical constant.[5] The average (most probable) hopping distance $\bar{R}$ can be determined from Eqs. (A.5) and (A.8),

$$\bar{R} = \left[\frac{9}{8}\frac{\alpha}{\pi\cdot g(\varepsilon)\cdot k}\right]^{1/4} T^{-1/4}. \tag{A.10}$$

---

[5] $B = 3\cdot 2^{7/12} - 2^{1/4}\cdot 3^{-1/2}$.

Third, one has to relate hopping process to the conductivity.[6] We consider localized states situated on two planes separated by the average hopping distance $\overline{R}$. There are S localized states on one plan and $(S + \overline{R} \cdot dS/dx)$ on the other. The net number of hopping events between the planes per unit time is $(-\nu \cdot \overline{R} dS/dx)$. The density of electrons participating in the hopping transport is given by $n = g(\varepsilon_F) \cdot kT$, where ε_F denotes the Fermi level. Therefore, $S = \overline{R} \cdot n$ and the net number of hopping events per unit area per unit time equals $(-\nu \cdot \overline{R}^2 \cdot dn/dx)$. Thus, the diffusivity is $\nu \cdot \overline{R}^2$ and the electrical conductivity follows as,

$$\sigma = ne\mu = g(\varepsilon_F) \cdot e^2 \nu \cdot \overline{R}^2, \tag{A.11}$$

where Einstein's relation has been applied. Combining Eqs. (A.9), (A.10), and (A.11) yields

$$\sigma = \sigma_o \exp[-(T_o/T)^{1/4}], \tag{A.12}$$

where $\sigma_o = \left[\frac{9\alpha \cdot e^4 (\nu_o)^2 g(\varepsilon_F)}{8\pi k} \right]^{1/2} T^{-1/2}$. Equation (A.12) shows that the conductivity depends on T as $\exp[-(T_o/T)^{1/4}]$.

[6] Charles Kittel, *Introduction to Solid State Physics*, 7th ed. (John Wiley & Sons, New York, 1996).

B. Numerical method for the displacement current device model

As discussed in section 2.3.4, the sheet concentrations of mobile and trapped holes at position x and time t are given by

$$\frac{\partial p}{\partial t} = \frac{e\mu}{C'}\left[\frac{\partial}{\partial x}\left(p\frac{\partial p}{\partial x}\right) + \frac{\partial}{\partial x}\left(p\frac{\partial p_T}{\partial x}\right)\right] + D\frac{\partial^2 p}{\partial x^2} + \left.\frac{\partial p}{\partial t}\right|_{traps} . \tag{B.1}$$

$$\frac{\partial p_T}{\partial t} = \tilde{c}p(N_T - p_T) - \tilde{e}p_T = -\left.\frac{\partial p}{\partial t}\right|_{traps} . \tag{B.2}$$

We discretize Eqs. (B.1) and (B.2). In the explicit (Forward Euler) method as shown in Fig. B.1, the first- and second-order partial derivatives of mobile hole concentration are given by

$$\frac{\partial p}{\partial x} = \frac{p_{i+1}^m - p_i^m}{\Delta x} , \tag{B.3}$$

$$\frac{\partial^2 p}{\partial x^2} = \frac{p_{i+1}^m - 2p_i^m + p_{i-1}^m}{(\Delta x)^2} , \tag{B.4}$$

$$\frac{\partial p}{\partial t} = \frac{p_i^{m+1} - p_i^m}{\Delta t} , \tag{B.5}$$

where m and i are the indices for time and position, respectively. Substituting Eqs. (B.3)–(B.5) into Eqs. (B.1) and (B.2), and collecting terms gives

$$p_i^{m+1} = p_i^m + \frac{e\mu\Delta t}{C'}\left\{\frac{1}{\Delta x}\left[\frac{1}{2}(p_{i+1}^m + p_i^m)\frac{p_{i+1}^m - p_i^m}{\Delta x} - \frac{1}{2}(p_i^m + p_{i-1}^m)\frac{p_i^m - p_{i-1}^m}{\Delta x}\right]\right.$$
$$\left. + \frac{1}{\Delta x}\left[\frac{1}{2}(p_{i+1}^m + p_i^m)\frac{p_{T\,i+1}^{\ m} - p_{T\,i}^{\ m}}{\Delta x} - \frac{1}{2}(p_i^m + p_{i-1}^m)\frac{p_{T\,i}^{\ m} - p_{T\,i-1}^{\ m}}{\Delta x}\right]\right\} \quad , \tag{B.6}$$
$$+ \frac{D\Delta t}{(\Delta x)^2}(p_{i+1}^m - 2p_i^m + p_{i-1}^m) + \Delta t \cdot [-\tilde{c}(N_T - p_{T\,i}^{\ m})p_i^m + \tilde{e} \cdot p_{T\,i}^{\ m}]$$

$$p_{T\,i}^{\ m+1} = p_{T\,i}^{\ m} + \Delta t \cdot [\tilde{c}(N_T - p_{T\,i}^{\ m})p_i^m - \tilde{e} \cdot p_{T\,i}^{\ m}] . \tag{B.7}$$

It should be noted that the explicit method is both convergent and stable if $\frac{D\Delta t}{(\Delta x)^2}$, $\frac{e\mu\Delta t}{2C'(\Delta x)^2}p_i^m$, and $\frac{e\mu\Delta t}{2C'(\Delta x)^2}p_{T\,i}^{\ m}$ are less or equal to 0.5 individually.[7] Consequently, we decrease Δt with increasing p_i^m as follows:

$$\Delta t = \left[\frac{\beta(\Delta x)^2}{D}\right] \cdot \left[\frac{kT}{kT + e(p_{i=1}^m + p_{T\,i=1}^{\ m})/C'}\right], \tag{B.8}$$

where $p_{i=1}^m = p(x=0,t)$ and $p_{T\,i=1}^{\ m} = p_T(x=0,t)$.

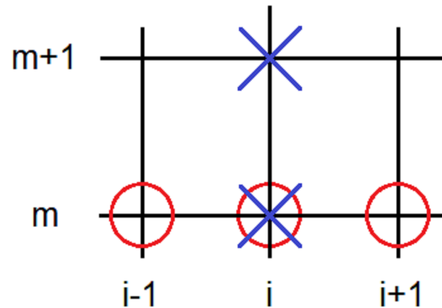

Figure B.1: A computational molecule for the explicit form.

[7] S. C. Chapra and R. P. Canale, *Numerical Methods for Engineers*, 5th ed. (McGraw-Hill, New York, 2006).

C. Analytical solutions for the non-linear resistor-capacitor circuit model

In this appendix, we present a detailed derivation of analytical solutions for the non-linear resistor-capacitor circuit and the resultant displacement current.[8] As discussed in sections 2.3.3 and 3.3.1, the current for $t > 0$ is given by

$$I(t) = WLC'\frac{dV_C(t)}{dt} = \frac{V_G(t) - V_C(t)}{R_{ch}(t)} = \frac{V_G(t) - V_C(t)}{L/[We\mu p(t)]}, \tag{C.1}$$

as shown in Fig. C.1. The total hole density, $P(t)$, is proportional to the potential across the capacitance,

$$eP(t)WL = \begin{cases} -CV_C(t), & V_C(t) < 0 \\ 0, & V_C(t) \geq 0 \end{cases}, \tag{C.2}$$

where the threshold voltage is set to zero. For the discussion here, effects of traps are neglected, i.e., $p(t) = P(t)$, and therefore,

$$\frac{dV_C}{dt} = \frac{\mu}{L^2}[(V_C)^2 - V_G V_C]. \tag{C.3}$$

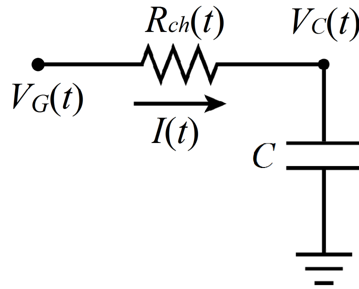

[8] G. B. Arfken and H. J. Weber, *Mathematical Methods for Physicists*, 6th ed. (Elsevier, New York, 2005).

Figure C.1: The model resistor-capacitor circuit.

C.1 Linear voltage profile

We discuss the case for which the gate voltage profile changes linearly with time. The initial conditions are given by

$$\begin{aligned} &V_G(t=0) = V_C(t=0) = 0 \\ &V_G(t>0) = -|r_V|t \end{aligned} . \tag{C.4}$$

Thus, from Eq. (C.3) one needs to solve the following differential equation

$$\frac{dV_C(t)}{dt} = \frac{\mu}{L^2}[(V_C)^2 - r_V t V_C] = \frac{\mu}{L^2}[V_C(t)]^2 - \frac{\mu r_V}{L^2} \cdot t \cdot V_C(t) . \tag{C.5}$$

Since $V_G(t=0) = V_C(t=0)$ and V_C approximately equals V_G in the long time limit, it is helpful to define $f(t)$ as

$$V_C(t) = V_G(t) - f(t) = -|r_V|t - f(t) , \tag{C.6}$$

where $f(t=0) = 0$ and $f(t \to \infty) = 0$. After combining Eqs. (C.5) and (C.6),

$$\frac{df}{dt} = -\frac{\mu|r_V|}{L^2} \cdot t \cdot f + |r_V| . \tag{C.7}$$

The analytical solution of $f(t)$ is obtained,

$$f(t) = -|r_V| \exp(-\frac{\mu|r_V|}{L^2}\frac{t^2}{2}) \int_0^t \exp(\frac{\mu|r_V|}{L^2}\frac{t'^2}{2}) dt' . \tag{C.8}$$

$V_C(t)$ and $I(t)$ follow:

$$V_C(t) = -|r_V| \cdot \left[t - \exp(-\frac{\mu |r_V|}{L^2} \frac{t^2}{2}) \int_0^t \exp(\frac{\mu |r_V|}{L^2} \frac{t'^2}{2}) dt' \right], \tag{C.9}$$

$$I(t) = WLC' \frac{dV_C(t)}{dt} = -\frac{r_V{}^2 \mu WC'}{L} t \exp(-\frac{\mu |r_V|}{L^2} \frac{t^2}{2}) \int_0^t \exp(\frac{\mu |r_V|}{L^2} \frac{t'^2}{2}) dt'. \tag{C.10}$$

In carrier extraction (discharging) process, the channel capacitor is discharged with increasing gate voltage. Assuming $V_C(t = t_p) = V_G(t = t_p) = V_p$, i.e. $I(t = t_p) = 0$, the initial conditions for the reverse sweep are

$$\begin{aligned} &V_G(t = t_p) = V_C(t = t_p) = V_p \\ &V_G(t > t_p) = V_p + |r_V| \tilde{t} \qquad , \\ &t = \tilde{t} + t_p \end{aligned} \tag{C.11}$$

where V_p are negative. Thus, Eq. (C.5) is modified:

$$\frac{dV_C(\tilde{t})}{d\tilde{t}} = \frac{\mu}{L^2} [V_C(\tilde{t})]^2 + \frac{\mu |V_p|}{L^2} V_C(\tilde{t}) - \frac{\mu |r_V|}{L^2} \cdot \tilde{t} \cdot V_C(\tilde{t}). \tag{C.12}$$

Similarly, $g(\tilde{t})$ is defined as

$$V_C(\tilde{t}) = V_G(\tilde{t}) - g(\tilde{t}) = -|V_p| + |r_V| \cdot \tilde{t} - g(\tilde{t}), \tag{C.13}$$

where $g(\tilde{t} = 0) = 0$ and $g(\tilde{t} \to \infty) = 0$. Combining Eqs. (C.12) and (C.13) gives

$$\frac{dg}{d\tilde{t}} = -|r_V| + (-\frac{\mu|V_p|}{L^2} + \frac{\mu|r_V|}{L^2}\tilde{t}) \cdot g \,. \tag{C.14}$$

The analytical solution of $g(\tilde{t})$ is obtained:

$$g(\tilde{t}) = -|r_V| \exp(\frac{\mu|r_V|}{L^2}\frac{\tilde{t}^2}{2} - \frac{\mu|V_p|}{L^2}\tilde{t}) \int_0^{\tilde{t}} \exp(-\frac{\mu|r_V|}{L^2}\frac{t'^2}{2} + \frac{\mu|V_p|}{L^2}t')dt' \,. \tag{C.15}$$

$V_C(\tilde{t})$ and $I(\tilde{t})$ follow:

$$V_C(\tilde{t}) = -|V_p| + |r_V| \cdot \left[\tilde{t} - \exp(\frac{\mu|r_V|}{L^2}\frac{\tilde{t}^2}{2} - \frac{\mu|V_p|}{L^2}\tilde{t}) \int_0^{\tilde{t}} \exp(-\frac{\mu|r_V|}{L^2}\frac{t'^2}{2} + \frac{\mu|V_p|}{L^2}t')dt' \right], \tag{C.16}$$

$$\begin{aligned} I(\tilde{t}) &= WLC' \frac{dV_C(\tilde{t})}{d\tilde{t}} \\ &= WC'|r_V|(-\frac{\mu|r_V|}{L}\tilde{t} + \frac{\mu|V_p|}{L}) \exp(\frac{\mu|r_V|}{L^2}\frac{\tilde{t}^2}{2} - \frac{\mu|V_p|}{L^2}\tilde{t}) \int_0^{\tilde{t}} \exp(-\frac{\mu|r_V|}{L^2}\frac{t'^2}{2} + \frac{\mu|V_p|}{L^2}t')dt' \end{aligned} \,. \tag{C.17}$$

C.2 Step function voltage profile

We discuss next the case for which the gate voltage profile is a step function. In other words, the channel capacitor is fully charged at a constant gate voltage initially, and then the gate voltage is abruptly changed.

$$V_G(t \le 0) = V_{GT.i} \,, \tag{C.18}$$

$$V_G(t > 0) = V_{GT.f} \,, \tag{C.19}$$

where $V_{GT.i} < 0$. Thus, Eq. (C.3) is modified:

$$\frac{dV_C}{dt} = \frac{\mu}{L^2}[(V_C)^2 - V_{GT.f} \cdot V_C]\,. \tag{C.20}$$

Depending on $V_{GT.f}$, the channel may become partially or completely depleted.

First, we assume that the value of $V_{GT.f}$ is less than zero, i.e., the channel is partially depleted in the final state. It is useful to define a function $u(t)$ as follows

$$u(t) = 1/V_C(t)\,, \tag{C.21}$$

$$\frac{du}{dt} = -(V_C)^{-2}\frac{dV_C}{dt}\,. \tag{C.22}$$

Substituting Eqs. (C.21) and (C.22) into Eq. (C.20) gives

$$\frac{du(t)}{dt} = -\frac{\mu}{L^2} + \frac{\mu V_{GT.f}}{L^2}u(t)\,. \tag{C.23}$$

With the initial condition $u(t=0) = 1/V_{GT.i}$, $u(t)$ is given by

$$u(t) = (\frac{1}{V_{GT.f}} - \frac{1}{V_{GT.i}})\exp(\frac{\mu V_{GT.f}}{L^2}t) + \frac{1}{V_{GT.f}}\,. \tag{C.24}$$

Hence, the voltage of the channel capacitor and the discharging current are:

$$V_C(t) = 1/[(1/V_{GT,f} - 1/V_{GT,i})\exp(\mu V_{GT,f}t/L^2) - 1/V_{GT,f}]\,, \tag{C.25}$$

$$I(t) = \frac{\mu C V_{GT,f}}{L^2}\frac{(1/V_{GT,f} - 1/V_{GT,i})\exp(\mu V_{GT,f}t/L^2)}{[(1/V_{GT,f} - 1/V_{GT,i})\exp(\mu V_{GT,f}t/L^2) - 1/V_{GT,f}]^2}\,. \tag{C.26}$$

Second, the channel is completely-depleted when $V_{GT.f} \geq 0$, and Eq. (C.20) becomes

$$\frac{dV_C}{dt} = \frac{\mu}{L^2}(V_C)^2 . \qquad \text{(C.27)}$$

Substituting Eqs. (C.21) and (C.22) into Eq. (C.27) gives

$$\frac{du(t)}{dt} = -\frac{\mu}{L^2} \qquad \text{(C.28)}$$

With the same initial condition $u(t=0) = 1/V_{GT.i}$, $u(t)$ is given by

$$u(t) = -\frac{\mu}{L^2}t + \frac{1}{V_{GT.i}} \qquad \text{(C.29)}$$

The voltage of the channel capacitor and the discharging current follow:

$$V_C(t) = -1/(\mu t / L^2 + 1/V_{GT,i}) \qquad \text{(C.30)}$$

$$I(t) = \frac{CL^2/\mu}{[t + (L^2/\mu V_{GT,i})]^2} \qquad \text{(C.31)}$$

Thus, the discharge currents of two different scenarios are given by

$$I(t) = \begin{cases} \dfrac{\mu C V_{GT,f}}{L^2} \dfrac{(1/V_{GT,f} - 1/V_{GT,i})\exp(\mu V_{GT,f} t / L^2)}{[(1/V_{GT,f} - 1/V_{GT,i})\exp(\mu V_{GT,f} t / L^2) - 1/V_{GT,f}]^2} & V_{GT,f} < 0 \\ (CL^2/\mu)/[t + (L^2/\mu V_{GT,i})]^2 & V_{GT,f} \geq 0 \end{cases} . \qquad \text{(C.32)}$$

D. Numerical method for the bilayer structure with interface parallel to the current direction

We present numerical methods for the bilayer structure with interface parallel to the current direction. In our model, electrons are injected from the left of the top layer, and holes are injected from the right of the bottom layer, as shown in Fig. D.1.

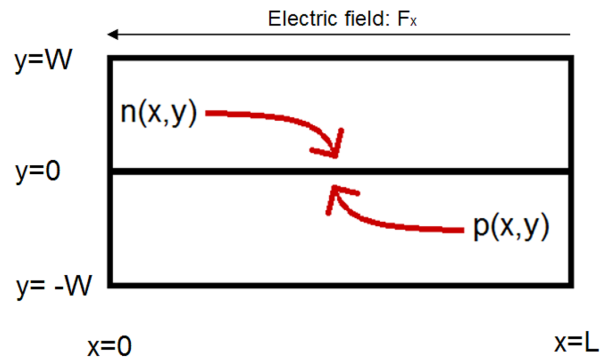

Figure D.1: Schematic diagrams for the bilayer structure with interface parallel to the current direction. Electrons injected from the top layer and holes injected from the bottom layer approach the interface and recombine under the influence of a uniform electric field, F_x.

In steady state, the divergence of currents equals zero:

$$\nabla \cdot J_n = \nabla \cdot J_p = 0\,, \tag{D.1}$$

$$\begin{aligned} J_n &= +eD_n(\partial n/\partial x + \partial n/\partial y) + e\mu_n n F_x \\ J_p &= -eD_p(\partial p/\partial x + \partial p/\partial y) + e\mu_p p F_x \end{aligned}, \tag{D.2}$$

where F_x is taken to be independent of x and y. Thus, the partial differential equations for electron and hole densities are:

$$\frac{\partial^2 p}{\partial x^2} + \frac{\partial^2 p}{\partial y^2} + \frac{\mu_p F_x}{D_p}\frac{\partial p}{\partial x} = 0 \tag{D.3}$$

$$\frac{\partial^2 n}{\partial x^2} + \frac{\partial^2 n}{\partial y^2} - \frac{\mu_n F_x}{D_n}\frac{\partial n}{\partial x} = 0 \tag{D.4}$$

To discretize Eqs. (D.3) and (D.4), we use centered finite-difference formulas given by

$$\frac{\partial f_{i,j}}{\partial x} = \frac{f_{i+1,j} - f_{i-1,j}}{2 \cdot \Delta x}, \tag{D.5}$$

$$\frac{\partial^2 f_{i,j}}{\partial x^2} = \frac{f_{i+1,j} - 2f_{i,j} + f_{i-1,j}}{(\Delta x)^2}, \tag{D.6}$$

$$\frac{\partial^2 f_{i,j}}{\partial y^2} = \frac{f_{i,j+1} - 2f_{i,j} + f_{i,j-1}}{(\Delta y)^2}. \tag{D.7}$$

Combining Eqs. (D.3)–(D.7) yields

$$\begin{aligned}&(1 + 2\alpha / \Delta x)\, p_{i+1,j} + (1 - 2\alpha / \Delta x)\, p_{i-1,j} \\ &+ (p_{i,j+1} + p_{i,j-1})(\Delta x / \Delta y)^2 - 2[1 + (\Delta x / \Delta y)^2]\, p_{i,j} = 0\end{aligned} \tag{D.8}$$

$$\begin{aligned}&(1 - 2\alpha / \Delta x)\, n_{i+1,j} + (1 + 2\alpha / \Delta x)\, n_{i-1,j} \\ &+ (n_{i,j+1} + n_{i,j-1})(\Delta x / \Delta y)^2 - 2[1 + (\Delta x / \Delta y)^2]\, n_{i,j} = 0\end{aligned} \tag{D.9}$$

where $\alpha = \mu_p F_x / D_p = \mu_n F_x / D_n = eF_x / kT$. The appropriate boundary conditions to solve the physical problem are given by

$$\begin{aligned}&n(x = 0) = n_0, \qquad p(x = L) = p_0 \\ &n(x = L) = p(x = 0) = 0\end{aligned}, \tag{D.10}$$

$$\partial n / \partial y\big|_{y=W} = \partial p / \partial y\big|_{y=-W} = 0, \tag{D.11}$$

$$J_s(x) = eD_n(\partial n / \partial y)\Big|_{y=0^+} = eD_p(\partial p / \partial y)\Big|_{y=0^-} = e\gamma \cdot n(x, y=0^+)\, p(x, y=0^-)\,. \qquad \text{(D.12)}$$

In order to calculate the recombination current at the interface, one has to discretize Eq. (D.12) carefully. As shown in Fig. D.2, carrier densities in the electron and hole layers are calculated according to Eqs. (D.8) and (D.9), and the boundary condition associated with the recombination current are expressed through n_1 and p_1.

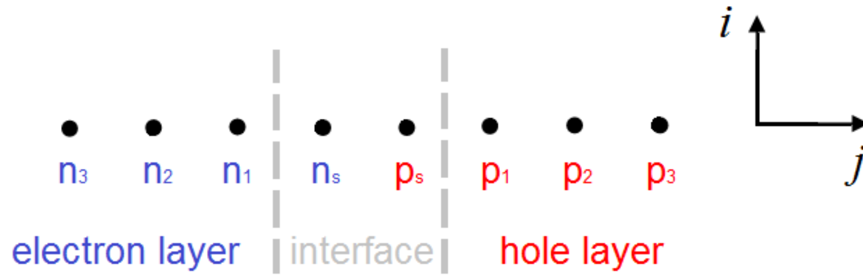

Figure D.2: Carrier densities with indices at the interface.

The diffusion between n_1 and n_s equals the interfacial recombination current involving n_s and p_s:

$$D_n \frac{\partial n}{\partial y}\Big|_{y=0} = D_n \frac{n_1 - n_s}{\Delta y} = \gamma \cdot n_s \cdot p_s\,. \qquad \text{(D.13)}$$

As a result, n_s is given by

$$n_s = \frac{n_1}{1 + \Delta y \cdot \gamma \cdot p_s / D_n}\,. \qquad \text{(D.14)}$$

Similarly, p_s is given by

$$p_s = \frac{p_1}{1 + \Delta y \cdot \gamma \cdot n_s / D_p}\,. \qquad \text{(D.15)}$$

Eqs. (D.8)−(D.15) are used to calculate carrier densities iteratively until the results converge.

In the interest of reducing the calculation time, analytical solutions of n_s and p_s as a function of n_1 and p_1 are added. Since carrier densities (n_1, p_1, n_s, and p_s) are related by the diffusion and recombination current,

$$D_n \frac{n_1 - n_s}{\Delta y} = D_p \frac{p_s - p_1}{\Delta y} = \gamma \cdot n_s \cdot p_s \,, \qquad \text{(D.16)}$$

n_s and p_s with respect to n_1 and p_1 are given by

$$\begin{aligned} n_s &= n_1 - \Delta y \cdot \gamma \cdot n_s \cdot p_s / D_n = n_1 - \lambda_n n_s p_s \\ p_s &= p_1 - \Delta y \cdot \gamma \cdot n_s \cdot p_s / D_p = p_1 - \lambda_p n_s p_s \end{aligned} , \qquad \text{(D.17)}$$

$$n_s \cdot p_s = [(\lambda_p n_1 + \lambda_n p_1 + 1) - \sqrt{(\lambda_p n_1 + \lambda_n p_1 + 1)^2 - 4\lambda_p n_1 \lambda_n p_1}\,]/(2\lambda_p \lambda_n) \,, \qquad \text{(D.18)}$$

where $\lambda_n = \Delta y \cdot \gamma / D_n$ and $\lambda_p = \Delta y \cdot \gamma / D_p$. Equations (D.17) and (D.18) decrease the calculation time dramatically when $\Delta x >> \Delta y$, which is the most useful situation. Subsequently, I_{rec} is calculated as follows

$$I_{rec} = \int_0^L J_s(x) dx = \int_0^L e\gamma \cdot n_s(x) p_s(x) dx \,. \qquad \text{(D.19)}$$

DGBSV, one of the FORTRAN 90 subroutines in LAPACK, is applied to solve the matrix problem.[9] The algorithm of the numerical calculation for Eqs. (D.8)−(D.18) is depicted by the flowchart shown in Fig. D.3.

[9] http://www.netlib.org/lapack/explore-html/index.html

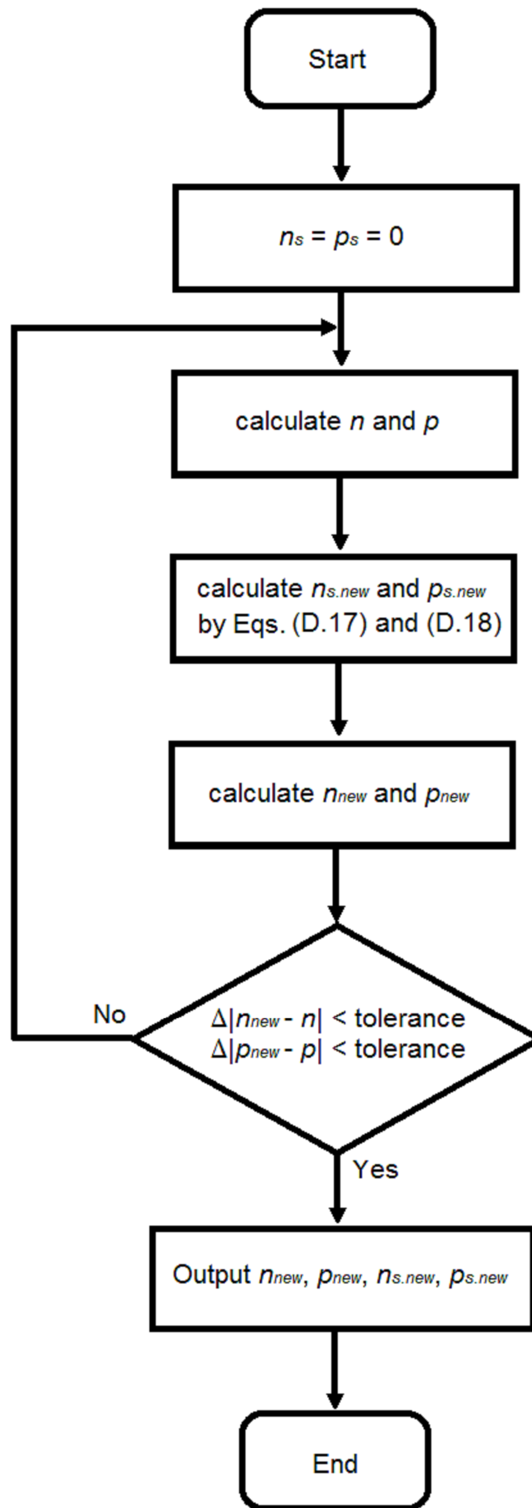

Figure D.3: Flowchart of the algorithm for the numerical calculation.